Tampere University

Arno Tavaila

POWER-TO-METHANOL PLANT CONCEPT

Dynamic Modelling and Control Solutions

Master of Science Thesis
Faculty of Engineering & Natural Sciences
Examiners: University Lecturer Henrik Tolvanen
University Teacher Veli-Pekka Pyrhönen
July 2024

ABSTRACT

Arno Tavaila: Power-to-Methanol Plant Concept: Dynamic Modelling and Control Solutions
Master of Science Thesis
Tampere University
Master's Programme in Environmental and Energy Engineering
July 2024

In Power-to-X concepts, electrical energy is converted into products that are easier to store and transport compared to electricity. The proliferation of such concepts could accelerate the ongoing global energy transition by providing, for example, power grid balancing, energy storage methods, and alternative transport fuels. In order for the different Power-to-X concepts to become more widespread in the future, the associated automation requirements and challenges need to be studied. The purpose of this work was to study typical subprocesses of a Power-to-Methanol plant and to develop a plant concept from them, which to model and simulate, so that the dynamic behavior of the subprocesses could be explored and control solutions for them be developed.

A Power-to-Methanol plant was considered in this work to be separable into five subprocesses, namely water electrolysis, hydrogen storage system, carbon capture system, carbon dioxide storage system, and methanol synthesis. The suitability of different technologies for the subprocesses was assessed based on available scientific literature, so that the plant concept modelled in this work could first be built. Suitable technology solutions were selected for the subprocesses of the developed plant concept, for example, based on criteria such as their common use, simplicity, and operational flexibility.

The modelling of the plant concept was approached by first creating input-output models of the different subprocesses, with the intention of later joining these simulation models together. The most prominent process dynamics were sought to be portrayed with these models, but due to the time constraint of this work and the complexity of the modelling task, many assumptions, and simplifications had to be utilized when designing the simulation models. The implementation of the designed models and the simulation runs, which were analyzed, were performed with MATLAB Simulink.

The behavior of the subprocesses was studied individually in this work with the originally created separate subprocess simulation models. The behavior of the subprocesses was tested by performing step response experiments on these models with the model input variables, whose effects were considered important from a control perspective. The simulation results of the tests were analyzed both to ensure that the models were implemented as planned and to review possible control variables. Despite the simplifications of the modelling, based on the analyzed simulation results and the behavior observed in them, it was possible to propose control solutions for all subprocesses of the Power-to-Methanol plant modelled in this work.

Keywords: PtX, methanol, modelling, simulation, energy transition, renewable energy

The originality of this thesis has been checked using the Turnitin Originality Check service.

TIIVISTELMÄ

Arno Tavaila: Power-to-Methanol -laitoskonsepti: Dynaaminen mallinnus ja säätöratkaisut
Diplomityö
Tampereen yliopisto
Ympäristö- ja energiatekniikan DI-ohjelma
Heinäkuu 2024

Power-to-X -konsepteissa sähköenergiaa muutetaan tuotteiksi, joita on helpompi varastoida ja kuljettaa kuin sähköä. Tällaisten konseptien yleistyminen voisi helpottaa menossa olevaa globaalia energiamurrosta tarjoten esimerkiksi sähköverkon tasapainotusta, energian varastointimetodeja ja vaihtoehtoisia liikennepolttoaineita. Jotta eri Power-to-X -konseptit voisivat yleistyä tulevaisuudessa, täytyy niihin liittyviä automaatiotarpeita ja -haasteita tutkia. Tämän työn tarkoituksena oli tutkia Power-to-Methanol -laitokselle tyypillisiä osaprosesseja ja rakentaa niistä laitoskonsepti, jota mallintaa ja simuloida, jotta osaprosessien dynaamista käytöstä voitiin tutkia ja kehittää niille säätöratkaisuja.

Power-to-Methanol -laitoksen katsottiin tässä työssä olevan erotettavissa viiteen osaprosessiin, jotka olivat veden elektrolyysi, vedyn varastointijärjestelmä, hiilidioksidin talteenottojärjestelmä, hiilidioksidin varastointijärjestelmä ja metanolisynteesi. Eri teknologioiden soveltuvuutta osaprosesseille arvioitiin saatavilla olevan tieteellisen kirjallisuuden perusteella, jotta työssä mallinnettu laitoskonsepti voitiin ensin rakentaa. Osaprosesseille valittiin työssä kehitettyyn laitoskonseptiin sopivia teknologiaratkaisuja käyttäen perusteena muun muassa niiden yleisyyttä, yksinkertaisuutta ja operoinnin joustavuutta.

Laitoskonseptin mallintamista lähestyttiin rakentamalla aluksi yksittäisistä osaprosesseista input-output -malleja, jotka oli tarkoitus myöhemmin yhdistää toisiinsa. Näillä malleilla pyrittiin kuvaamaan merkittävimmät prosessidynamiikat, mutta työn rajallisen aikataulun ja mallinnustehtävän monimutkaisuuden vuoksi monia oletuksia ja yksinkertaistuksia tuli hyödynnettyä simulointimalleja suunniteltaessa. Suunniteltujen mallien toteuttaminen ja analysoidut simulointiajot tehtiin MATLAB Simulinkillä.

Tässä työssä osaprosessien käyttäytymistä tutkittiin yksittäin, aluksi tehdyillä toisistaan irrallisilla osaprosessien simulointimalleilla. Osaprosessien käyttäytymistä testattiin tekemällä näille malleille askelvastekokeita sellaisilla sisääntulomuuttujilla, joiden vaikutusten ajateltiin olevan merkittäviä säädön näkökulmasta. Testien simulointituloksia analysoitiin sekä sen varmistamiseksi että mallien toteutus oli tehty kuten oli suunniteltu että mahdollisten ohjausmuuttujien arvioimiseksi. Mallinnuksessa tehdyistä yksinkertaistuksista huolimatta analysoitujen simulointitulosten ja niissä havaitun käyttäytymisen perusteella pystyttiin ehdottamaan säätöratkaisuja kaikille tässä työssä mallinnetun Power-to-Methanol -laitoksen osaprosesseille.

Avainsanat: PtX, metanoli, mallinnus, simulointi, energiamurros, uusiutuva energia

PREFACE

This thesis was written for Valmet Automation Oy. I offer my gratitude towards all the people at Valmet who helped me during the writing process of this thesis and who made the working experience so enjoyable. Special thanks are given to my thesis supervisor at Valmet, Jyri Kaivosoja, and the people in my coffee break crew at module 30, who I had some unforgettable discussions and moments with. I would also like to thank my supervisors from the university, Henrik Tolvanen and Veli-Pekka Pyrhönen, who gave me important guidance and help throughout this project.

Finally, as I am about to graduate after this thesis, I would like to acknowledge and thank my friends and my family who supported me during my studies at Tampere University.

Tampere, 6 July 2024

Arno Tavaila

CONTENTS

LIST OF SYMBOLS

Latin symbols:

A	area	m^2
b	molality	mol/kg
C_v	valve coefficient	m^2mol/kg
c	specific heat capacity	J/(kgK)
c_m	molar heat capacity	J/(molK)
F	Faraday constant	C/mol
ΔG	change in Gibbs energy	J/mol
ΔH	reaction heat	J/mol
I	electric current	A
j	electric current density	A/m^2, or A/cm^2
j_0	exchange current density	A/cm^2
j_L	limiting current density	A/cm^2
M	molar mass	kg/mol
m	mass	kg
$\dot{m}$	mass flow rate	kg/s
N	number of electrolyzer cells	-
n	polytropic exponent	-
n	molar amount of substance	mol
$\dot{n}$	molar flow rate	mol/s
P	power	W
$P-\%$	pump power setting	%
p	pressure	Pa, or bar
$p_{H_2O_{vap}}$	saturation vapor pressure of water	Pa
ΔQ	change in heat energy	J/mol
$\dot{Q}$	heat transfer rate	W
R	ideal gas constant	J/(molK)
R_x	specific gas constant	J/(kgK)
r	area specific electrical resistance	Ωcm^2
S	stoichiometric number	-
T	temperature	K, or °C
t	time	s
t_{res}	reactor residence time	s
U	overall heat transfer coefficient	$W/(m^2K)$
U	voltage	V
U_{act}	activation overpotential	V
U_{con}	concentration overpotential	V
U_{ocv}	open circuit voltage	V
U_{ohm}	ohmic overpotential	V
U_{rev}	reversible voltage	V
U_{tn}	thermoneutral voltage	V
V	volume	m^3
w	mass fraction	-
$wt-\%$	mass percentage	%
X	CO_2 loading	$mol_{CO2}/kg_{solvent}$
y	valve opening	-
y_{MeOH}	methanol synthesis yield	%
Z	compressibility factor	-
z	electrons transferred per electrochemical reaction	-

Greek symbols:

α	electron transfer coefficient	-
η	efficiency	-
η_F	Faraday efficiency	-
ρ	density	kg/m^3

LIST OF SUBSCRIPTS

abs	absorber
$absd$	absorbed
an	anode
avg	average
c	cold fluid side of a heat exchanger
ca	cathode
$cell$	electrolyzer cell
$comp$	compressor
$cooling$	removing heat energy
$desd$	desorbed
fg	flue gas
$fline$	feedline piping
gas	gas inside the synthesis reactor
HHV	higher heating value
h	hot fluid side of a heat exchanger
$heating$	providing heat energy
hx	heat exchanger
in	inlet stream
LHV	lower heating value
max	maximum
min	minimum
op	operation value
out	outlet stream
PEM	PEM electrolyzer system
$prod$	synthesis product stream
reb	reboiler
ref	reference value
sol	loaded solvent solution
str	stripper
$sump$	liquid volume at the bottom of a column
$tank$	storage tank
unl	unloaded solvent solution
$valve$	valve
x	unspecified chemical substance

1. INTRODUCTION

We are currently living in the midst of global energy transition where our dependency on fossil fuels must be reduced to slow down climate change. This transition towards more environmentally friendly energy technology is happening both in traditional power production and in transportation. But to effectively reach climate targets, major development and innovation are still needed in many areas. This development is being pushed forwards by tightening emission regulations, governing policies, and supporting policies in renewable energy technology and power production fields. (International Energy Agency (IEA), 2018)

One of the major problems in increasing renewable energy sources like solar and wind is their weather dependency, which means that they are not continuously available. This varying availability means that they are not suitable for use as a base load or for answering the fluctuations in energy demand. These kinds of intermittent electricity sources, which cannot be controlled, cause balancing issues for power grids. To combat these issues energy storage solutions are expected to play a major part in grid stability and security in the future. (Mlilo, et al., 2021)

Power-to-X (PtX or P2X) technologies are processes where renewable electricity is converted to different products, which are easier to store, and transport compared to electricity. These products include renewable fuels and key chemicals such as hydrogen, formaldehyde, methanol, and methane. PtX concepts can provide a multitude of benefits including power grid balancing by consuming surplus electricity production, providing energy storage solutions, replacing transportation fuels with renewable alternatives, and providing use cases for CO_2 as a raw material, all of which can accelerate the current energy transition towards a more sustainable future. (de Vasconcelos & Lavoie, 2019)

This thesis focuses on Power-to-Methanol processes, with an aim to gain understanding and expertise about the process automation needs and challenges of possible future PtX customers. Methanol is an interesting PtX product, because it has many applications in the chemical industry as a feedstock material, and it is also considered as a renewable alternative to replace fossil fuels. Methanol is also easy to store and handle as liquid, which makes the methanol economy an attractive alternative for hydrogen economy.

(Basile & Dalena, 2017) However, recent studies show that Power-to-Methanol conversion is still not economically competitive with established methanol production methods (Adnan & Kibria, 2020; Sollai, et al., 2023).

The objectives of this thesis are to develop and model a Power-to-Methanol plant concept, and design control solutions for it. To reach these objectives, the following research questions need to be answered, and the given modelling task completed:

1. What subprocesses does Power-to-Methanol conversion entail, and what technology solutions are suitable to be used for these subprocesses?

Research task: modelling the developed Power-to-Methanol plant.

2. What kind of dynamic behavior of the subprocesses can be observed from performed test simulation runs?
3. How could the subprocesses of the developed plant concept be controlled?

The main results of the work will be a simulation model or models of the developed Power-to-Methanol plant, and control solutions for the plant subprocesses, which will be proposed based on the analyzed simulation results of tested simulation runs. The proposed control solutions will include basic stabilizing and quality controllers for the subprocesses, and suggestions on what measurements should be utilized by these controllers. The model implementation and simulation are done with MATLAB Simulink, and the created model or models are later supposed to be used in testing the developed controls, but this was not included in the scope of the actual thesis work.

The work is divided into two parts, which are a literature review and an applied part, which in this work consists of the previously mentioned modelling task. The literature review is presented in Chapter 2, and it tries to answer research question 1. In the literature review, different subprocess technology possibilities are compared to each other to understand their working principles and suitability for a Power-to-Methanol plant. Few points of interest include what kind of operating limits are caused by process components, by process behavior, by safety concerns, and what kind of operational flexibility is possible. Chapter 3 works as a bridge between the literature review and the applied part, as it discusses mathematical modelling in general and explains how the modelling task was approached in this work. Chapter 4 explains the methodology of this thesis work more thoroughly and presents how the modelling was done. The results of this work are presented in Chapter 5, which answers research questions 2 and 3 as first simulation runs are analyzed to study the dynamic behavior of the subprocesses, and possible control solutions for these subprocesses are proposed based on their observed behavior.

2. POWER-TO-METHANOL

A Power-to-Methanol concept is studied in this thesis, because of the growing need for grid balancing solutions that would permit more renewable energy. Studies in the past have found that renewable methanol production is not yet economically competitive with existing production technologies. (Adnan & Kibria, 2020; Sollai, et al., 2023) However, in these studies major costs were attributed to electricity consumption, which would not be the case in future energy systems where added renewable capacity would decrease wholesale energy prices. (International Energy Agency (IEA), 2023) A methanol production plant could also make additional revenue if it can participate in grid balancing.

George Olah Renewable Methanol plant, located in Svartsengi, Iceland, is used as a reference, which works as the basis for the Power-to-Methanol plant concept that will be built in this work. This plant was the world's first industrial scale methanol production facility that utilized captured CO_2 as a synthesis feedstock. This CO_2 is captured from an adjacent geothermal power plant's flue gas and purified before being catalytically synthesized with hydrogen to produce methanol in the synthesis process. The hydrogen for the synthesis is produced via electrolysis of water. The annual production capacity of the George Olah renewable methanol plant is 4000 tons. (Carbon Recycling International, n.d.) A simplified flowsheet of a Power-to-Methanol process, which includes the previously mentioned subprocesses, is presented below in Figure 1. Additionally, hydrogen and CO_2 storages are included in the subprocesses considered in this work, so that operation flexibility of methanol production can be studied more thoroughly.

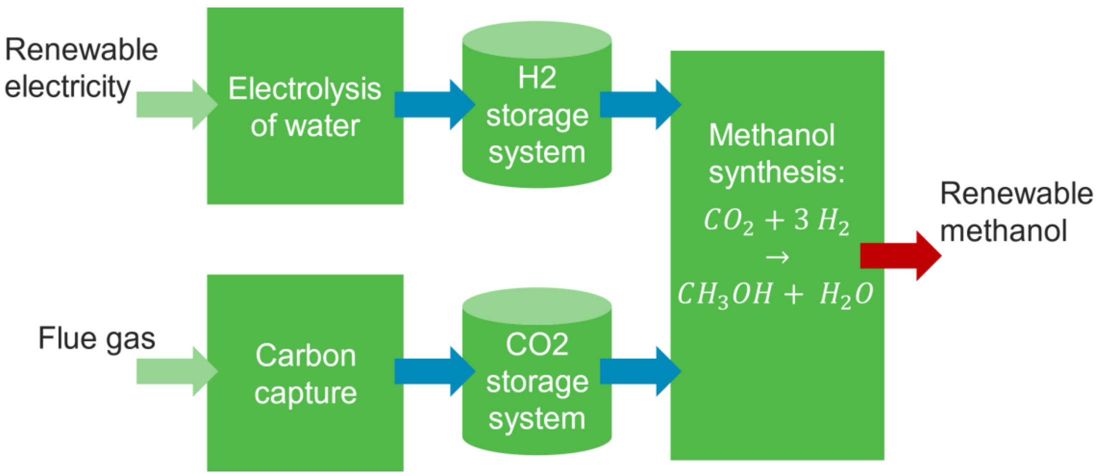

Figure 1. *Simplified flowsheet of a Power-to-Methanol process, and the subprocesses studied in this work.*

Most of the subchapters in the following literature review focus on the subprocesses that are pictured in Figure 1, electrolysis of water, carbon capture, methanol synthesis, and the storage concepts of hydrogen and CO_2. Competing technologies of each of these subprocesses are discussed and reviewed to develop a Power-to-Methanol plant concept that can be modelled in the experimental part of this thesis work. But first, in the next subchapter, a little background is given about the current applications of methanol and the status of its production technologies.

2.1 Global Demand and Production of Methanol

Methanol (CH_3OH), which can also be called methyl alcohol, is the simplest possible saturated alcohol, where a methyl group is attached to a hydroxyl group. It is a volatile, colorless, and polar liquid in moderate conditions. In petrochemical industry, methanol has major significance as a feedstock for other valuable chemical products. These products can be for example fuels, pharmaceuticals, solvents, or antifreeze agents. Methanol is also considered as an alternative fuel for internal combustion engines. (Basile & Dalena, 2017)

Methanol has long been suggested as a viable energy storage medium and as a fuel. The concept of *"Methanol Economy"* has been in development for over two decades. Methanol's use as a transportation fuel or fuel additive has especially gained more interest towards methanol economy. Methanol is in large-scale use as an automotive fuel in China, and in Europe it is used as a maritime fuel. Back in 2013 the annual use of methanol in fuel blends had already reached 4 million tons (Mt) in China, with different methanol fuel blends being available in 15 Chinese provinces, with more than 1500 equipped filling stations. (Olah, et al., 2018)

Methanol has multiple attributes that make it an excellent fuel, but its most important attributes are usually considered to be that it is extremely clean burning, and that it is in liquid phase at standard temperature and pressure (STP), which makes methanol relatively easy to distribute and store. As a transportation fuel, it has also gained interest due to production scalability. Methanol is easy to synthesize, and it has a wide range of feedstocks from which it can be produced from. (Verhelst, et al., 2019)

Some major products for which methanol can be used include acetic acid, olefins, formaldehyde, methyl tert-butyl ether (MTBE), biodiesel, and dimethyl ether (DME). DME like methanol is considered as an alternative clean fuel in the transportation sector. DME can also be used as a refrigerant or as a solvent for extracting various compounds. (Basile & Dalena, 2017) MTBE has also already since the 1980s been used as a fuel additive to gasoline. However, due to groundwater contamination, it has been banned in some countries, for example in the United States, but the use of MTBE is still rising in other regions. (International Renewable Energy Agency (IRENA), 2021)

During the 2010s, the annual methanol production nearly doubled, reaching approximately 98 Mt in 2019, with China having a major influence in the increased production. China is both the world's largest methanol producer and consumer. In 2018, they consumed 55 Mt, which was over half of global production back then. (International Renewable Energy Agency (IRENA), 2021) Historically feedstock costs have accounted up to 90 % of methanol's total production costs, meaning that cheap feedstock options have so far been a key driver of methanol economics (Basile & Dalena, 2017). Until recently, fossil-based feedstocks have been used almost exclusively in methanol production (Coal 35 %, Natural Gas 65 %), with biomass and other renewable sources accounting for under 1% of production, with less than 0.2 Mt of annual production. (International Renewable Energy Agency (IRENA), 2021) Global production capacity and demand for different methanol applications are presented below in Figure 2 for the last six years at the time of writing this thesis.

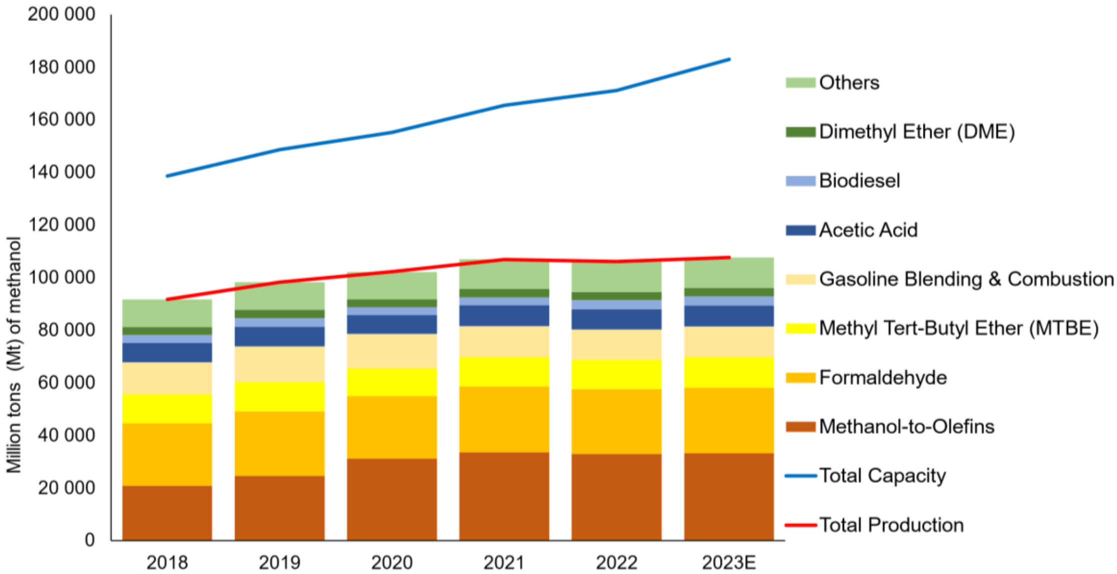

Figure 2. *Global methanol demand and production capacity from 2018 to 2023. Based on source* ***(Methanol Institute, 2023)****.*

Figure 2 is based on data that was provided by Methanol Market Services Asia (MMSA) to Methanol Institute. For better clarity, methanol applications that did not exceed over 3 Mt demand in any year were all combined to the *"others"* -segment in this graph. Data shown for the year 2023 was based on estimations. From Figure 2 it is clearly visible that the methanol market growth has somewhat stagnated during the last few years.

In a 2023 techno-economic assessment of a modelled Power-to-Methanol system, where it was produced from green hydrogen and captured CO_2, it was calculated that the production cost (960 €/t) would be about double the amount of methanol's international market price (450 €/t). The estimation was done with an expected production plant lifetime of 20 years. High production cost was mainly caused by estimated electricity consumption and the capital costs of electrolyzers. (Sollai, et al., 2023) In 2020, another study, which modelled and compared three different Power-to-Methanol concepts, calculated their levelized production costs to vary between 860-1585 $/t, when using then present electricity prices and market conditions. (Adnan & Kibria, 2020)

2.2 Water Electrolysis

Unlike many chemical compounds, hydrogen is not found in its free form on Earth at all. This means that it cannot be collected as such from nature and must be instead separated from other elements like water or hydrocarbons. The generation of hydrogen and oxygen by electrolysis of water was discovered back in the early 1800s by William Nicholson and Anthony Carlisle. (Olah, et al., 2018)

The overall electrolysis reaction equation of water into hydrogen and oxygen can be given as:

$$H_2O \rightarrow H_2 + \frac{1}{2}\, O_2. \tag{1}$$

The reaction heat ΔH or in this case the overall energy demand of the reaction, consists of the change in Gibbs energy ΔG, which must always be supplied electrically, and the heat that must supplied for the reaction ΔQ:

$$\Delta H = \Delta G + \Delta Q. \tag{2}$$

In a temperature range from 0 to 1000 °C, this overall energy demand changes very little (from 283.5 to 291.6 kJ/mol), but the share of its parts on the other hand changes significantly. With rising temperature levels, the heat or thermal demand rises, and the minimum electrical demand decreases. (Buttler & Spliethoff, 2018) The energy demand of water electrolysis is presented below in Figure 3 as a function of the temperature. In this figure, water's heat of vaporization is not included in the plotted values when water is supplied as steam instead of liquid in temperatures over 100 °C.

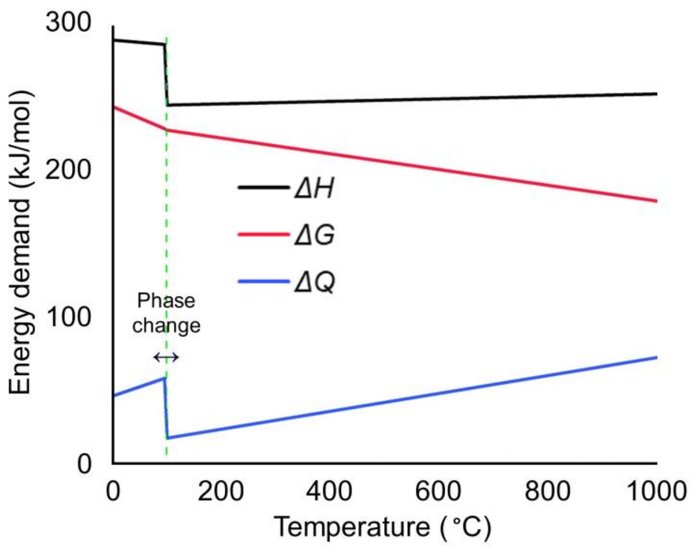

Figure 3. *Energy demand of water electrolysis as a function of temperature. Adapted from source* ***(Bi, et al., 2014)***

The theoretical minimum voltage U_{rev} of electrolysis can be calculated from the necessary change in Gibbs energy, when it is considered that all the necessary heat is at the same time delivered externally:

$$U_{rev} = \frac{\Delta G}{zF}, \tag{3}$$

where z is the number of electrons transferred per produced H_2 molecule ($z = 2$), and F is the Faraday constant (a. 96 485 C/mol). On the other hand, if the total energy demand of the reaction is supplied electrically then the theoretical voltage can be calculated similarly from the total energy demand ΔH:

$$U_{tn} = \frac{\Delta H}{zF}. \tag{4}$$

This U_{tn} value is called the thermoneutral voltage. (Buttler & Spliethoff, 2018) At normal temperature and pressure (NTP) U_{rev} is 1.229 V, and U_{tn} is 1.482 V, but these values change based on process temperature and pressure along with the changing energy demand (Ulleberg, 2003).

The power consumed by an actual electrolyzer cell P_{cell} can easily be calculated from its voltage U_{cell}, and operation current I:

$$P_{cell} = U_{cell} I, \tag{5}$$

and the cell's energy efficiency η_{cell} can be calculated by dividing its theoretical minimum consumption P_{min} with the actual power consumption. This also means that the energy efficiency can be analogically calculated directly from the cell voltage and the theoretical thermoneutral voltage:

$$\eta_{cell} = \frac{P_{min}}{P_{cell}} = \frac{U_{tn}}{U_{cell}}. \tag{6}$$

The actual cell voltages are higher than the theoretical voltage because of the voltage drop caused by ohmic resistance, and the overpotential that is needed. Practical cell voltages in the industry are usually between 1.8-2.6 V. (Wang, et al., 2014)

The previous energy efficiency definition must still be extended with a new term, which is the Faraday efficiency η_F (also called the current efficiency). It accounts for the current losses that happen in an electrochemical system. In cases where electrolyzes are run outside their nominal conditions, parasitic current losses and losses caused by recombination of the product gases can significantly reduce the Faraday efficiency. The corrected definitions are presented below:

$$\eta_{HHV} = \frac{U_{tn_{HHV}}}{U_{cell}} \eta_F, \tag{7}$$

$$\eta_{LHV} = \frac{U_{tn_{LHV}}}{U_{cell}} \eta_F. \tag{8}$$

There are two different definitions for the energy efficiency of an electrolyzer cell as, it can be calculated from either the higher heating value (HHV) or lower heating value (LHV) of hydrogen, which are denoted in the definition subscripts. (Buttler & Spliethoff, 2018)

The HHV value of hydrogen is defined as the amount of heat released during its combustion, when it is originally at 25 °C, and the water produced in the combustion is condensed and cooled back to 25 °C after the process. However, there is no generally agreed upon definition of hydrogen’s LHV value, but the main principle is that the water produced by combustion is assumed to be steam at the end of the process. Usually, hydrogen’s LHV value is defined as the amount of heat released by combustion of hydrogen that is initially at 25 °C, when the end temperature of the combustion products is 150 °C. This temperature limit of 150 °C is based on the acid gas dew point. Under these conditions and definitions, the LHV value of hydrogen is 241.8 kJ/mol, which corresponds to a thermoneutral voltage of 1.25 V. The HHV value of hydrogen corresponds to a thermoneutral voltage of 1.48 V at standard conditions. (Li, et al., 2022) A more accurate value of 1.482 V (Ulleberg, 2003) for the HHV value based thermoneutral voltage was also reported earlier in the thesis when discussing equation 4.

The amount of produced hydrogen can be calculated from the known amount of transferring electric charge per mole of produced hydrogen (zF -term), where $z\ is$ 2, and F is the Faraday constant (a. 96 485 C/mol). The production rate of an electrolyzer, which consists of several cells in series, can be expressed as:

$$\dot{n}_{H_2} = \frac{NI}{zF}\eta_F. \quad (9)$$

The production is directly proportional to the electric current in the circuit I, which is multiplied with the number of cells N and the Faraday efficiency η_F. The amount of water consumption and the production rate of oxygen can be simply calculated from the overall stoichiometric reaction equation, which was presented earlier in equation 1. (Ulleberg, 2003)

There are currently three competing main technologies for electrolysis of water, alkaline electrolysis (AE), proton exchange membrane electrolysis (PEM), and solid oxide electrolysis (SOE). Alkaline electrolyzers are the most commercially ready technology, and they are already available at a MW scale. (Carmo, et al., 2013; Bos, et al., 2020) Solid oxide electrolyzers are expected to become the most efficient electrolyzer type in the future, but they are not yet commercially available (Bos, et al., 2020). Simplified electrolyzer configurations of the main technologies are presented below in Figure 4.

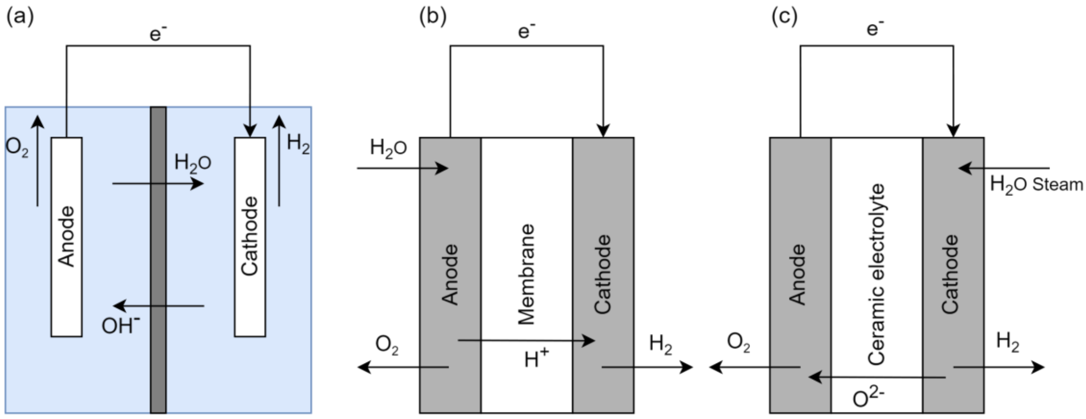

Figure 4. *Simplified electrolyzer cell configurations of: (a) alkaline electrolysis, (b) proton exchange member electrolysis, (c) solid oxide electrolysis. Based on source* ***(Li, et al., 2021)****.*

2.2.1 Alkaline Electrolysis

The main advantage of alkaline water electrolysis is that the electrolyzers can be made of inexpensive materials. Electrodes that are used for hydrogen production can be made from either iron or nickel steel, and the electrodes for oxygen can be made from nickel. These electrodes are immersed in a highly concentrated electrolyte solution, usually potassium hydroxide (KOH) solution, and they are separated by a porous solid material (diaphragm), which allows the OH^- ions in the solution to pass through. At the anode, the reaction is:

$$4\,OH^- \rightarrow O_2 + 2\,H_2O + 4\,e^-, \quad (10)$$

and at the cathode the reaction is:

$$4\,H_2O + 4\,e^- \rightarrow 2\,H_2 + 4\,OH^-. \tag{11}$$

Unlike with the OH^- ions, the diaphragm material does not allow the reaction products to pass through, as it has a very low permeability to hydrogen and oxygen gases. This stops the gases from mixing, which prevents safety issues and low Faraday efficiencies. (Godula-Jopek, 2015)

Alkaline electrolysis is a mature and well-established technology, with multiple AEs commercially available and in operation globally. The biggest advantages of alkaline electrolyzers, other than their cheap electrode materials, are their robustness and long lifetime. Alkaline electrolyzers are already suitable for producing hydrogen in large quantities. (Bodner, et al., 2015)

The formation of gases in AE cells causes several problems for the electrolysis system. The forming gas bubbles will damage the electrode surfaces while also blocking them, which limits the electron transfer from the electrolyte. Gas bubbles also increase the resistance of the electrolyte. These problems mean that only low maximum power densities can be achieved with liquid electrolytes. (Bodner, et al., 2015) Typical commercial current densities are between 0.2-0.5 A/cm^2 (Lange, et al., 2023). Because the diaphragm in AE cells does not totally prevent the product gases from cross-diffusing through it, they can recombine back to water, which decreases the efficiency. This can also cause safety hazards as the mixing gases can reach explosive concentrations. Because decreasing the electrolyzer load only decreases the production rates of gases, but not their permeability through the diaphragm, both problems become more severe on lower loads. This means that AE cells are not suitable for operation at low partial loads. (Carmo, et al., 2013; Godula-Jopek, 2015)

2.2.2 Proton Exchange Membrane Electrolysis

The first PEM electrolyzer concept was developed in the 1960s. This electrolysis concept can be referred to as either proton exchange membrane or polymer electrolyte membrane -water electrolysis, but they share the same acronym. (Carmo, et al., 2013) A thin (50-250 μm) proton-conducting polymer membrane is used as solid electrolyte in PEM technology, which makes compact cell designs possible. The anode reaction in PEM cell is:

$$H_2O \rightarrow \frac{1}{2}\,O_2 + 2\,H^+ + 2\,e^-, \tag{12}$$

and the cathode reaction is:

$$2\,H^+ + 2\,e^- \rightarrow H_2. \tag{13}$$

Because the used polymer materials have a highly acidic environment, platinum group metal catalysts that will not dissolve need to be used. (Godula-Jopek, 2015) At both the anode and the cathode, the catalyst layer is where the half reaction takes place. These layers consist of catalyst particles (platinum or platinum alloy), which are placed near the membrane. (Litster & McLean, 2004)

PEM electrolyzers can operate at high current densities (>2 A/cm^2), which reduces operational costs and potentially the overall costs of water electrolysis. They also react quickly to power input changes because proton transfer through the membrane is not delayed by inertia, like it is with liquid electrolytes. As a solid electrolyte, the polymer membrane allows strong structures and high operational pressures for PEM cells. Very low gas crossover through the membrane also allows a wider operation range, as the efficiency does not drop on lower loads as significantly as it does with alkaline electrolyzers. (Carmo, et al., 2013)

High operational pressures of PEM cells cause an increase in cross-permeation phenomenon of the gases. In over 100 bar pressures, this means that thicker membranes and internal gas combiners are needed to keep the product gas concentrations under the safety limits. PEM cell materials must also be able to handle the polymer membrane's corrosive acidic environment, and high overvoltage, especially at high current densities. This makes cells expensive as they require scarce, expensive materials and components such as platinum group metal catalysts and titanium-based current collectors and separator plates. (Carmo, et al., 2013)

2.2.3 Solid Oxide Electrolysis

SOE technologies operate at temperatures ranging from 700 to 900 °C. This high temperature operation results in higher efficiencies than achieved with AE or PEM, but it causes a significant challenge concerning material stability. Water is provided to SOE cells as steam, which must be preheated to the operation temperature. At the anode, air can be used to remove the produced oxygen gas. The anode reaction in SOE technology is:

$$O^{2-} \rightarrow \frac{1}{2}\, O_2 + 2\, e^-. \tag{14}$$

and the cathode reaction is:

$$H_2O + 2\, e^- \rightarrow H_2 + O^{2-}. \tag{15}$$

Some of the produced hydrogen gas must also be recycled back to the cathode in SOE cells to maintain proper reducing conditions. (Buttler & Spliethoff, 2018)

SOE cells consist of three ceramic layers, two are porous electrode layers and then there is a dense electrolyte placed between them. The electrolyte material must have adequate gas-tightness, good ion conductivity, thermal expansion coefficient similar to the electrodes, chemically inert nature with respect to the electrodes, stability in both oxidizing and reducing environments, and mechanical stability in the demanding operating conditions. The most common electrolyte material is yttria-stabilized zirconia (YSZ). The electrodes must be highly porous, to allow steam diffusion and removal of product gases, and have high electric conductivity along with some degree of ionic conductivity. The anode material is usually a nickel/yttria stabilized zirconia (Ni/YSZ), which is a ceramic-metal composite (cermet). The cathode material is usually a mix of some perovskite material and electrolyte material, for example LSM (Lanthanum Strontium Manganite) mixed with YSZ. (Godula-Jopek, 2015)

SOE technology emerged as a way of reducing operating costs by moving to steam electrolysis instead of the conventional liquid water electrolysis technologies. As explained earlier, the amount of the required electric demand decreases when temperature rises. This means that a bigger portion of the total energy demand can be supplied as heat instead of electricity. To demonstrate this, the thermoneutral voltage U_{tn} only increases from 1.48 to 1.52 V in temperature range of 25-1000 °C, but within the same temperature range, the minimum voltage U_{rev} drops from 1.23 to 0.91 V. Theoretically this means that up to 40 % of the total energy required in steam electrolysis (at 1000 °C) could be supplied as heat. (Ursua, et al., 2012)

Even though the total energy demand increases, the decrease in electrical energy demand is more meaningful economically. Over two thirds of the cost of hydrogen produced by electrolysis is caused by electricity consumption, meaning that high temperature electrolysis can majorly cut down production costs. (Laguna-Bercero, 2012) Furthermore, high temperature operation results in better efficiencies than with AE or PEM technologies. This happens because the kinetics of the electrolysis reactions increase, which results in a decrease in electrical losses in the cell due to lower ohmic resistance in the electrolyte and lower polarization losses from the electrode reactions. (Hauch, et al., 2008)

Despite the advantages that are gained from the high operation temperature, it is also the cause of most of the challenges that SOE technology faces. It means significant challenges concerning the thermal stability of cell materials and sealing issues. In addition, the cathode product stream that is a mixture of hydrogen and water steam causes a need for additional processing, which results in much higher capital costs of SOEs compared to established liquid water electrolysis technologies. (Ursua, et al., 2012) Degradation of the materials is also an issue that limits operation duration of SOE cells currently, and it needs to be studied further to develop a more mature technology (Godula-Jopek, 2015).

2.2.4 Operation Flexibility of Water Electrolysis

Operation flexibility of water electrolysis is important when combined use with intermittent renewable electricity sources is considered. In cold start-up, the electrolysis system needs to be heated to its operating temperature. This means that the system's operation temperature, heat-capacity, and mass define cold start-up speeds of different electrolyzer technologies. Warm start-up refers to when electrolysis is started from a stand-by where the system is already at operating temperature. (Lange, et al., 2023)

Electrolysis systems like AE that have a liquid electrolyte seem to be at some disadvantage in renewable energy integration compared to solid electrolyte systems. This is because the circulation of a liquid electrolyte inherently increases inertia in the ion transport, which makes load change response slower. (Rajeshwar, et al., 2008) Electrolysis systems can still generally operate very dynamically. They are mainly limited by heat management, the maximum voltage of the rectifier, and the time coefficients of external components. AE and PEM electrolyzers that are run at nominal temperatures can change their full load range in seconds. This makes both suitable for grid balancing activities. (Buttler & Spliethoff, 2018)

A summary of the main electrolyzer technologies' key operation parameters is presented below in Table 1. SOE technologies were left out of this table because they are still in development phase, which excludes them from the subprocess consideration for the Power-to-Methanol plant concept that will be built in this work.

Table 1. *Summarized key operation parameters of AE and PEM electrolyzers. Based on sources* ***(Carmo, et al., 2013; Buttler & Spliethoff, 2018; International Renewable Energy Agency (IRENA), 2020; Hermesmann, et al., 2021; Lange, et al., 2023)***

Electrolyzer type	AE	PEM
Temperature (°C)	40 - 100	20 - 150
Pressure (bar)	<60	<80
Cell Area (m^2)	<4	<0.3
Current density (A/cm^2)	0.13 - 0.8	0.6 - 4
Voltage (V)	1.8 - 3.0	1.8 - 3.0
Voltage efficiency (%, HHV)	49 - 82	49 - 82
Load range (%)	10 - 100	0 - 160
Ramp up speed (%/s)	10 - 50	10 - 90
Ramp down speed (%/s)	10	40.6
Warm start-up time (s)	60 - 300	<10
Cold start-up time (min)	<50	<20

From the values presented in the table, cell pressures, and cold start-up-times had the most variation between the referenced sources. In the table typical upper pressure values were decided to be included, but one source suggested that pressures up to 200 bar could be reached with both cell types (Hermesmann, et al., 2021), and another source suggested cold start-up times below 15 minutes for alkaline electrolyzers (Lange, et al., 2023), which compared to other sources seemed unrealistic. Numerical values for ramp speeds were only available in one of the sources (Lange, et al., 2023), so they could not be compared to other reported values.

2.3 Hydrogen Storage

Current hydrogen storage solutions can be divided into two main categories, physical-based, and material-based. In physical-based solutions hydrogen is stored by itself either as a gas or as a liquid, and in material-based solutions it is absorbed into another material either chemically or physically. Because compressed gas storage is one of the more mature storage technologies and as it does not consume as much energy as other physical-based technologies (liquid and compressed -cryogenic hydrogen storage), it was chosen as the most suitable for the studied Power-to-Methanol concept. (Moradi & Groth, 2019)

In STP conditions, hydrogen is in gas phase as it has both the second-lowest boiling point and melting points of all substances, second only to helium. At atmospheric pressure, hydrogen must be cooled below its boiling point of -253 °C for it to liquefy. As a gas, hydrogen has a low ratio of energy per volume in all practically reachable pressures, which makes it hard to store significant amounts of energy in compressed hydrogen storage solutions. As an example, hydrogen gas is approximately 8 times less dense than methane in normal conditions. (Carriveau & Ting, 2016)

The density of most gases can usually be approximated with high accuracy by the ideal gas law, which relates the pressure, volume, and the temperature of a given gas amount. However, the behavior of hydrogen deviates significantly from the predictions of the ideal gas law, as hydrogen gas always occupies more space than predicted. A simple way of correcting the calculation is adding a compressibility factor Z to the law. Compressibility factors are estimated from experimental measurement data, and they depend on the temperature, pressure, and the nature of the gas. The gas law corrected with the compressibility factor can be written as:

$$pV = ZnRT, \tag{16}$$

where p is the pressure, V is the volume, T is the temperature, and n is the molar amount of the gas, while R is the ideal gas constant. (Carriveau & Ting, 2016) The compressibility factor of hydrogen gas is shown in Figure 5 below as a function of pressure for specified constant temperatures.

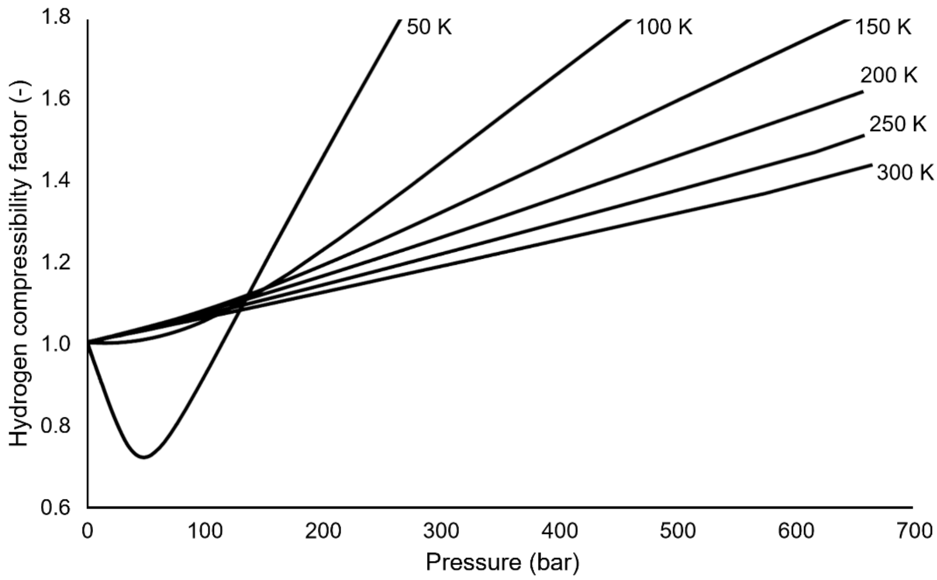

Figure 5. *Compressibility factor of hydrogen as a function of pressure for specified temperatures. Adapted from source* ***(Hirscher, 2010)***

The pressure vessels commonly used for storing compressed hydrogen gas can be divided into types I-IV, defined based on the vessel materials. The most used storage vessel shape is cylindrical. Type I vessels are fully metallic, type II have a thick metallic liner hoop that is partially wrapped in resin composite on the cylindrical part, types III and

IV are both made of composite materials, but differ in their liner materials. Type III has a mostly metal based liner and type IV has mostly polymer liner or an extremely thin metal liner. (Barthelemy, et al., 2017)

The use of composite pressure vessels remains quite small compared to metallic pressure vessels due to their high costs, as some compromise between technical performance and cost competitiveness must be usually made. Hydrogen in industrial applications is typically stored in type I metallic vessels, that are the cheapest, at pressures between 200 and 300 bar. These storages have very poor mass storage efficiency, with only about 1 % of the weight coming from the stored hydrogen. Higher working pressures and mass storage efficiencies can be reached with vessel types III and IV, that can reach pressures of 700 bars. (Barthelemy, et al., 2017) The technical performance and mass storage efficiency matter most when considering storage applications for transportation of hydrogen, so type I vessels are perfectly suitable for a stationary application like the considered Power-to-Methanol plant in this thesis (Hassan, et al., 2021).

Compressed hydrogen is usually stored at room temperature, even though this causes safety concerns and challenges for the durability of storage materials. At room temperature high-pressure and high-purity hydrogen has significant degrading effects on the mechanical properties of metals, which increases the risk of failure of hydrogen components. This phenomenon is commonly called hydrogen embrittlement. Resistance towards hydrogen embrittlement is therefore an important material property that needs to be considered in hydrogen processes. (Zheng, et al., 2012)

The only compressor types that can handle high enough flow capacities required in large-scale hydrogen production are reciprocating compressors and centrifugal compressors. Because these compressors can only achieve limited pressure ratios that are not enough to achieve the high pressures of hydrogen storage systems in just one stage, hydrogen must be compressed in multiple stages. Hydrogen is also cooled down between each compression stage to make the compression process less adiabatic and more isothermal, which decreases the amount of needed work. In practice, the compression process is therefore a polytropic process, which is somewhere between adiabatic and isothermal processes. The power consumed by polytropic compression can be calculated with the following equation:

$$P = \dot{n} Z_{avg} R T_{in} \frac{n}{n-1}\left(\left(\frac{p_{out}}{p_{in}}\right)^{\frac{n-1}{n}} - 1\right), \tag{17}$$

where $\dot{n}$ is the molar flow of the compressed gas, Z_{avg} its average compressibility factor, T_{in} the temperature before compression in Kelvin, p_{in} the pressure before compression,

p_{out} the pressure after compression, and finally n the polytropic exponent. (Tahan, 2022) In a case where hydrogen storage is used, the compressor's delivery pressure to the storage and its compression ratio will change over time according to the pressure inside the hydrogen storage tank (Mucci, et al., 2023). A simplified process configuration of a compressed hydrogen storage system is presented below in Figure 6.

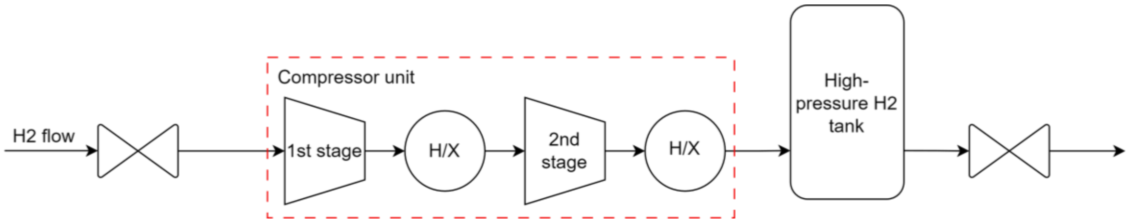

Figure 6. *Simplified compressed hydrogen storage system configuration. Based on source* ***(Li, et al., 2020)***

Fast filling of compressed hydrogen storage results in a temperature rise in the vessel, due to both the temperature rise caused by the compression of hydrogen and the Joule-Thomson effect, which heats hydrogen when it is throttled. Experimental and numerical investigations have shown that the temperature rise during a storage filling process depends mainly on the filling rate, initial pressure, and ambient temperature. (Zheng, et al., 2012)

However, multiple studies show that Joule-Thomson effect contributes very little to the overall temperature rise during a compressed hydrogen storage filling process in operation temperature range of 0-100 °C, and operation pressure range of 1-350 bar. (Dicken & Mérida, 2007; Galassi, et al., 2014; Striednig, et al., 2014) The phenomenon that is mainly responsible for the temperature rise in the filling process is the compression of the hydrogen gas inside the storage vessel. This compression happens when higher-pressure gas is added to the storage from the fueling station. The increase in temperature caused by compression is known as heat of compression. (Dicken & Mérida, 2007) The different phenomena that affect temperature rise in a gas tank filling process are visualized below in Figure 7.

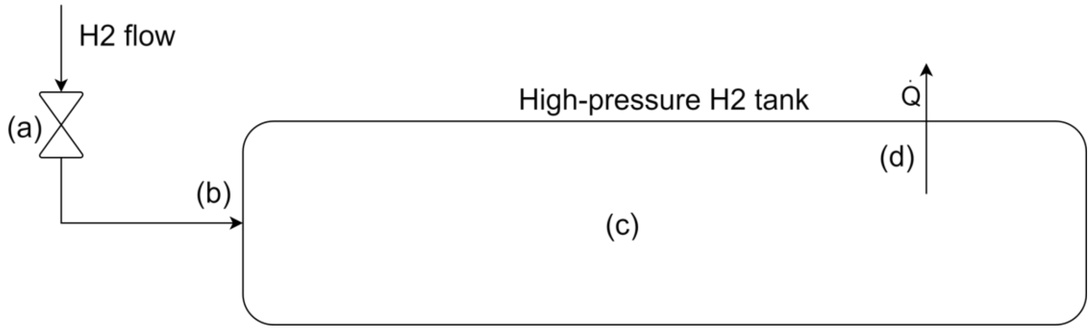

Figure 7. *Temperature related phenomena in theoretical gas tank filling process: (a) Joule-Thomson effect, (b) conversion of kinetic energy into internal energy of the gas, (c) compression of the gas inside the vessel, (d) heat transfer through the tank walls. Based on sources* ***(Dicken & Mérida, 2007; Li, et al., 2020)***

Counter to the filling process, during the discharging process of a compressed hydrogen tank, its temperature drops due to the expansion of the gas inside the storage vessel. In the discharging process of compressed hydrogen tank, the temperature must not go below the design limit of -40 °C. (Melideo, et al., 2017)

2.4 Carbon Capture

CO_2 emissions are considered the main cause of the ongoing climate change, and its emission reduction methods are therefore becoming increasingly important. One method of mitigating CO_2 emissions is carbon capture technologies, which aim to reduce emissions from industrial sources. Carbon capture methods that are used in power generation can be divided into three categories based on where the capture stage is in the process chain. These methods are pre-combustion, during combustion (oxy-fuel combustion), and post-combustion. Along with reducing emissions, carbon capture technologies provide an opportunity for the use of CO_2 as a raw material, like in the Power-to-Methanol concept that is studied in this thesis. (Vaz, et al., 2022)

Because the CO_2 in the considered Power-to-Methanol concept is sourced from flue gas, only post-combustion technologies are discussed in this thesis work. Post-combustion capture technologies are already well-established, and they can be integrated to existing power plants with minimal risk, and without major impact on plant operation, but their cost of implementation is still relatively high. (Mumford, et al., 2015)

2.4.1 Post-combustion Carbon Capture

Post-combustion capture consists of two process steps, which are CO_2 absorption and CO_2 stripping. In the first step CO_2 is captured from the flue gas stream with a solvent, and then in the second step it is separated from the now CO_2 rich solvent in a stripping process, which also regenerates the solvent for continuous use. (Wilberforce, et al.,

2021) Chemical solvents are the most used solvent type in post-combustion carbon capture technologies, with amine-based solvents being most the common out of them (Mumford, et al., 2015). Chemical solvents are commonly used because they are the most suitable solvent type for absorption when the treated flue gas has low CO_2 partial pressures and concentrations (Yu, et al., 2012). A simplified process configuration of a conventional chemical solvent based post-combustion carbon capture unit is presented below in Figure 8**.**

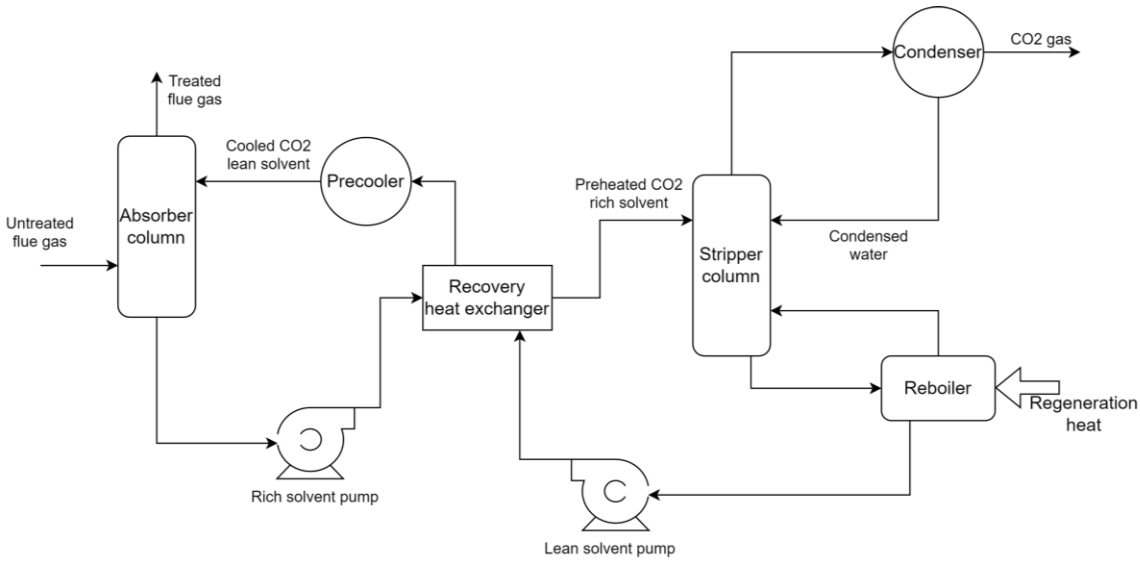

Figure 8. *Simplified configuration of a post-combustion carbon capture system with a chemical solvent. Based on sources* ***(Bui, et al., 2014; Oko, et al., 2017; Wilberforce, et al., 2021)***

The process configuration in Figure 8 is simplified by not including a flue gas pretreatment process before the absorber column or a water wash section at the top of the absorber. Pretreatment methods for neutralizing SOX and NOX emissions from the flue gas are usually needed, because the commonly used amine-based solvents are sensitive to chemical degradation by these acidic gases. (Bui, et al., 2014) The flue gas is typically also cooled to around 50 °C, before it is pretreated and supplied to the absorber column (Gülen & Hall, 2017). Water wash sections can be used to maintain a suitable solvent concentration in the solution, and to remove emissions generated from the degradation of the amine-based solvents, as some of these emissions are categorized as hazardous air pollutants (Drewry & Rochelle, 2024).

In addition to the traditional amine-based solvents, other chemical solvents have also been commissioned for pilot use, which for example include amine-based blended solvents, ammonia-based solvents, amino acid salt -based solvents, and carbonate salt -based solvents. (Mumford, et al., 2015) Monoethanolamine (MEA) solvents are generally considered as the benchmark for post-combustion chemical CO_2 absorption process, with under 30 wt-% MEA solutions generally being used. The biggest problem in using

MEA solvents is their high energy consumption during stripping and regeneration, with the energy consumption being in the range of 3.2-4.2 GJ per captured CO_2 ton. This means that a retrofitted post-combustion carbon capture unit using MEA as the solvent could consume more than one-third of a power plant's original electricity generation capacity. (Oko, et al., 2017)

The energy consumed during CO_2 stripping and solvent regeneration is used by a reboiler unit to generate stripping steam, which is used to separate CO_2 from the liquid solvent in the stripper. When the rich solvent is fed down the stripper column, the stripping steam flow is fed counter to it. The steam flow then removes CO_2 from the solvent and carries it out of the stripper column to the condenser. (Wang, et al., 2017) Heat to the reboiler unit is usually supplied by process steam, and the drop in power generation that was mentioned in the previous paragraph occurs if the steam must be extracted from a power plant's steam turbine. The temperature level of the solvent regeneration is normally around 120 °C, so a low-pressure steam extraction can be utilized. (Gülen & Hall, 2017) This suggests that in combined heat and power (CHP) plants where there is no low-pressure turbine section, district heating production would be decreased instead of electricity production.

Even though MEA is widely used as a solvent in CO_2 absorption systems, there is limited information on its reaction enthalpy in absorbing and stripping processes. Its reaction heat is however a parameter of prime importance in designing post-combustion carbon capture systems in which the steam consumption in the solvent regeneration process is directly related to it. The reaction heat of CO_2 absorption into the liquid solvent can be either measured with direct calorimetry or estimated from available data, but even small inaccuracies in the used data can lead to high levels of uncertainty in the resulting reaction heat values. (Kim & Svendsen, 2007)

In a calorimeter measurement study, the heat of absorption of CO_2 into a 30 wt-% MEA solution, over a temperature range of 40-120 °C, was observed to be dependent both on the process temperature and the CO_2 loading in the solvent. It was observed that the reaction heat increases with increased temperature. In constant temperatures, the differential reaction heats measured in the work stayed constant until CO_2 loadings over the saturation loading (0.5 mol_{CO2}/mol_{MEA}) were reached, after which carbamate reversion and physical absorption can occur. Approximating from the figures presented in the study, this measured constant reaction heat before the CO_2 saturation loading seems to be around 85 kJ/mol at 40 °C, around 95 kJ/mol at 80 °C, and around 110 kJ/mol at 120 °C. After the saturation loading had been reached, the reaction heat values started to decrease. (Kim & Svendsen, 2007)

The CO_2 loading that was referred to in the previous paragraph is usually defined as:

$$X = \frac{n_{CO_2}}{m_{MEA}+m_{H_2O}} = \frac{n_{CO_2}}{m_{unloaded}}, \tag{18}$$

which is the ratio of the molar amount of absorbed CO_2 and the mass of the unloaded solvent solution that also includes the mass of water. But other definitions can also be used, like the loading value that was given in the previous paragraph, which was a ratio of the molar amount of the absorbed CO_2 and the molar amount of MEA in the used solvent. (Notz, et al., 2012) Regardless of the used definition, CO_2 loading refers to the amount of CO_2 that is absorbed into the solvent or its solution.

To improve the process energy efficiency more complex post-combustion capture configurations have also been developed compared to the conventional process presented in this work, but as they require extra equipment, this leads to higher investment costs for the capture systems as well. These configurations can for example be based on added absorber intercooling or CO_2 stripping done in multiple pressure stages. (Oko, et al., 2017) In this his thesis work, the focus is kept strictly on the conventional process configuration, which was presented earlier in Figure 8. More about alternative post-combustion capture configurations can for example be read from the following simulation study that studied the energy consumption of different available process configurations (Ahn, et al., 2013).

Besides the high energy consumption of the solvent regeneration, another problem with the use of MEA and other amine-based solvents is their degradation in the carbon capture process, which causes all sorts of problems including economic, operational, and environmental problems. As an example of the degradation rate of the commonly used MEA, a replacement of 2.2 kg per ton of captured CO_2 is required due to its degradation, which leads to increased operation costs of the capture process. (Yu, et al., 2012)

2.4.2 Operation Flexibility of Post-combustion Carbon Capture

High energy consumption during operation and high cost of the technology implementation are problems that must be resolved before post-combustion carbon capture systems based on chemical absorption can be deployed in large-scale. One proposed approach to make the technology more economical is the flexible operation of the capture process to reduce energy consumption during periods of high electricity prices. Many studies on post-combustion carbon capture focus on steady state operation, while flexible operation and its optimization are often overlooked. But flexible operation must be studied, as continuous operation with a steady CO_2 capture rate may not be economically feasible. Additionally, the rising amount of intermittent energy sources creates a need for more flexible operation of post-combustion CO_2 capture units as the traditional power plants are also operated more flexibly, which leads to fluctuation in their flue gas amount and conditions. (Bui, et al., 2014)

A carbon capture unit can slow down a power plant start-up due to its steam consumption. This negative impact of CO_2 capture during power generation start-ups could be avoided by bypassing the CO_2 capture process completely or partially by venting excess flue gas. (Bui, et al., 2014) However, continuous processes such as CO_2 absorption, and CO_2 stripping cannot be shut down or started at will. If the CO_2 capture process is bypassed by the flue gas, the hydraulic conditions in the absorber and the stripper will change significantly. Flooding or poor wetting of the columns will occur if the gas flow rate through the capture system is too high or too low. So, the throughput of the capture system can only be decreased to a certain point before normal operation cannot be maintained anymore due to poor wetting. (Lin, et al., 2012)

A stripper bypass configuration within the carbon capture process system where solvent flow rate to the stripper column could be reduced with a bypass line is also suggested for partial load operation. Another flexible operation configuration could also be achieved with solvent storages, where one tank would be used to collect rich solvent, and another tank to collect lean solvent. Rich solvent would be stored during high electricity prices, which would allow a higher power output of the plant as the solvent regeneration and energy consumption in the stripping would be reduced. At the same time, lean solvent would be fed from the other storage to the absorber to still maintain a high CO_2 removal rate. Conversely, during low electricity price periods, the rich solvent left in the storage could be regenerated in the stripping process and stored into the lean solvent tank. Unlike a straight stripper bypass, this configuration could be used even with strict emission regulations, as no CO_2 is vented in its flexible operation. (Bui, et al., 2014) However, in both these suggested configurations the throughput of the stripper would be changed dynamically, which could lead to unstable operation caused by the hydraulic conditions of the stripper, which once again limits the achievable load range of these configurations. (Lin, et al., 2012)

To avoid fluctuating hydraulic conditions in the columns during flexible operation, an approach where lean solvent CO_2 loading is altered is suggested. In this configuration, the solvent flow rate would stay constant, and different CO_2 capture rates would be achieved by controlling the reboiler heat load and the amount of CO_2 gas being separated in the stripper. Lean solvent CO_2 loading would decrease with increased reboiler heat load allowing more CO_2 to be captured in the absorber, and conversely decreased reboiler load would increase the CO_2 loading of the solvent recycled back to the absorber, which would then decrease the CO_2 capture rate. To maintain a constant gas flow rate in the stripper, part of the separated CO_2 should also be recycled back to the stripper in this configuration. (Lin, et al., 2012)

Based on another modelling study, changing the reboiler heat duty might however be a too slow control mechanism for the CO_2 capture process. The change in the capture performance would be slow because before the change in the solvent CO_2 loading would affect the absorber column, the solvent would first need to pass through the crossflow heat exchanger and possible solvent buffer tanks in the system. To achieve quicker control by directly affecting the CO_2 absorption rate, changing the mass transfer area by controlling the solvent flow rate might instead be a better control solution. (Nittaya, et al., 2014)

In solvent flow control method, the CO_2 capture rate would follow the variation of the lean solvent flow. The reboiler temperature would be at the same time controlled to keep it constant because the reboiler temperature can be used as an indicator of the CO_2 loading in the solvent. By varying the reboiler heat load accordingly, the CO_2 loading in the recirculated lean solvent could be approximately kept as a constant. In the solvent flow control method, the hydraulic conditions in the columns would not be kept as constant due to the varying solvent throughput, which again limits the available load range of this control method. Based on an earlier modelling study, the limiting factor would again be the fluctuation of hydraulic conditions in the stripper, while the fluctuation in the absorber would be relatively minor compared to it. (Lin, et al., 2012)

In a modelling study based on a process configuration with decoupled rich solvent and lean solvent storage, a flue gas load range of 50-130 % of the design capacity was achieved with the lean solvent flow control method. The control method was used to keep CO_2 removal at above 90 % and the lean solvent loading at 0.21 mol_{CO2}/mol_{MEA}. (Gaspar, et al., 2015) In another modelling study, which was done with Aspen Plus the authors identified a capacity range of 78-125 %, when they modelled variating flue gas amounts. This flue gas -based capacity range was again identified to be limited by the hydraulic conditions in the columns, with the upper operation limit being caused by flooding of the absorber, and the lower limit by poor wetting of the absorber. The liquid-to-gas (L/G) ratio in the columns was said to be kept constant, suggesting that the solvent flow in the study was controlled by (or that it followed) the amount of flue gas flow (Herrmann, et al., 2020) Suggesting that the capacity range limits were caused by the (Lin, et al., 2012), which was referenced in the previous paragraph. It suggested that with the solvent flow control method, the fluctuation of hydraulic conditions in the stripper would be more severe than in the absorber.

One experimental study with pilot-scale chemical absorption post-combustion carbon capture system found no significant barriers for flexible operation in none of the five different studied operation scenarios. This included gas turbine start-up and shutdown scenarios where 30 % flue gas -based operation capacities were achieved without problems. The tests were completed using a 30.16 wt-% MEA solution as the solvent, and the solvent and gas flow rates were ramped down simultaneously to maintain a constant liquid-to-gas ratio. The maximum ramp down speed for liquid and gas flows used in the shutdown test was 7.5 %-baseload/min, and the maximum ramp up speed during the start-up test was 5.7 %-baseload/min. It should be noted that due to dimensional differences of the absorber column in the test system compared to actual carbon capture systems, a lower lean solvent CO_2 loading had to be used to achieve 90 % CO_2 capture rate in the absorber, which means that an unusually high solvent flow rate and L/G ratio were present in all the test scenarios. This difference compared to actual industrial capture plants might also cause differing behavior during dynamic operation compared to real systems. A more thorough explanation of the test conditions and of the other flexibility test scenarios can be read from the referenced original source. (Tait, et al., 2016)

To estimate process dynamics, it is important to understand what effects the lag times between different process components in a system. In chemical absorption based post-combustion carbon capture systems, the solvent circulation times have a direct impact on the dynamic response of the process, as they define when a process operation change can be observed in another part of the system. For example, in the test system that was discussed in the previous paragraph, it took approximately 30 minutes at 100 % load to see the effect of reboiler heat load change in the CO_2 loading at a measurement point located after the absorber column. The solvent circulation times in the system are dependent on the total solvent inventory, and flow rates at different load capacities. The solvent flow rates in the test were controlled with a solvent pump, which could reach new setpoint values in approximately 10 seconds. This means that compared to the dynamic change in the total system, the dynamic response time of the pump can be thought of as insignificant. (Tait, et al., 2016)

It seems that when choosing the control solution, either a quicker load response (solvent flow control method) or wider load range (solvent CO_2 loading control method) must be chosen. Finding reliable information about actual load ranges or ramp rates proved to be a challenge because the flexible operation of a post-combustion carbon capture system can mean two different things, it can mean either that different amounts of flue gases can be treated, or that the capture rate can be operated dynamically. Additionally, most studies that discuss flexible operation of post-combustion carbon capture seem to be either modelling studies, or pilot-scale experimental studies, instead of experimental studies conducted in actual industrial scale capture systems, which increases the uncertainty of the load ranges reported in available literature. The dynamic operation parameters of a solvent flow control method based chemical absorption post-combustion carbon capture systems estimated from the studies that have been referenced earlier in this work are summarized in Table 2 below. It must be noted again that these values are not measured from actual industrial capture systems and should as such be treated with healthy skepticism.

Table 2. *Estimated dynamic operation parameters of chemical absorption post-combustion carbon capture systems. Based on sources* ***(Gaspar, et al., 2015; Tait, et al., 2016; Herrmann, et al., 2020)***

Control method	Solvent flow control
Minimum load (%)	30 - 78
Maximum load (%)	125 - 130
Maximum solvent flow ramp up speed (%/min)	5.7
Maximum solvent flow ramp down speed (%/min)	7.5
Solvent circulation time through the system (min)	>30

2.5 CO_2 Storage

To offer operation flexibility, a CO_2 storage system was included in the subprocesses considered for the Power-to-Methanol concept being developed in this thesis work. In contrast to the previously discussed compressed gaseous hydrogen storage, which involved complex behavior and operational limits, a CO_2 storage system included in a Power-to-Methanol plant can have a simple liquid storage tank. This is because CO_2 can be stored as a liquid in pressure vessels under moderate conditions with straightforward connections with the rest of the system. (Chen & Yang, 2021; Sollai, et al., 2023)

The process used to adjust the state of CO_2 after capture systems, for transportation or storage applications, can be referred to as CO_2 conditioning. Extensive research has been done to optimize capture systems because of the major energy penalty caused by traditional capture methods, but this has also diverted attention away from CO_2 conditioning, which is another essential step of the full carbon capture and storage systems. (Muhammad, et al., 2019)

Integrally-geared compressors have been used in high-pressure CO_2 applications for decades, and they can be considered as the conventional method to compress CO_2. The pressure ratio of the used compressors is usually around two, and the compression to high pressures is usually done in multiple stages, with intercoolers between each compression stage to cool the gas back to ambient temperature. If the critical pressure of CO_2 (7.38 MPa) is exceeded, then compressors in the following pressure stages can be replaced with pumps, as CO_2 behaves similarly to a liquid above its critical pressure at 25 °C. (Jackson & Brodal, 2018) No gas compression related equations are presented in this subchapter, as gas compression was already discussed in Chapter 2.3.

For liquefaction process of captured CO_2, two processes are presented here. These processes are categorized based on if they use external or internal cooling for the liquefaction. In a liquefaction process which uses external refrigeration, CO_2 can be compressed directly to the wanted transport or storage pressure, after which it is liquefied by condensing it using an external refrigeration cycle. The cooling is called external because the refrigerant is not in direct contact with the CO_2 gas. Separators are also used between compression stages to remove condensed impurities like water from the CO_2 flow. In an internal cooling gas liquefaction process, CO_2 is compressed to a higher pressure than needed, after which it is throttled. During the expansion in the throttling process, CO_2 cools down and some of the gas is condensed. The non-condensed CO_2 is then separated and recirculated back to a suitable compression stage. (Øi, et al., 2016) This internal cooling gas liquefaction method can be used only when the Joule-Thomson coefficient of the processed gas is positive in the throttling conditions (Aliyon, et al., 2020).

In a Power-to-Methanol plant configuration that was considered by Chen and Yang, CO_2 was stored as a liquid in the pressure required by the downstream synthesis process, and its saturation temperature at that pressure. Based on the flowsheet presented in their work, the liquefaction of CO_2 was done with a condenser after the final compression stage, meaning that it could be identified as an external refrigeration liquefaction process. (Chen & Yang, 2021) A simplified process configuration of a CO_2 storage system with external refrigeration liquefaction is presented below in Figure 9. Separators were not included in the liquefaction configuration as per the referenced source, which might be reasonable if the purity of captured CO_2 is already very high.

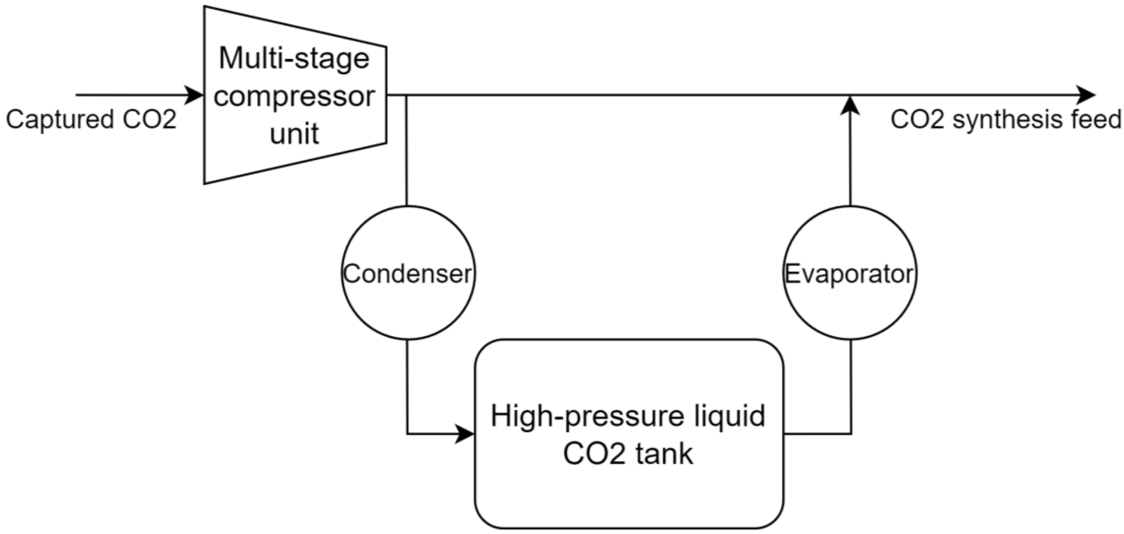

Figure 9. *Simplified CO_2 storage system configuration with external refrigerant liquefaction process. Based on source* ***(Chen & Yang, 2021)***

2.6 Methanol Synthesis

In the dominating coal and natural gas feedstock production methods of methanol, these feedstocks are first converted to syngas, from which methanol is then produced. Syngas mainly consists of carbon monoxide (CO) and hydrogen. It can be produced from coal via gasification, where the coal reacts with oxygen and water steam at high temperatures to form the coveted syngas. (Zhen & Wang, 2015) Syngas is also similarly produced from natural gas by having it react with water steam. This syngas production method is called natural gas reforming, in which methane is the main component, that converts to syngas. To achieve high conversion efficiencies (>99 %) in methanol production with natural gas as a feedstock, sulfur must be removed before the reforming process, because it could poison used catalyst materials. (Çelebi & Aydın, 2019)

The syngas produced via coal gasification must be enhanced with water-gas-shift reaction to obtain more hydrogen, because of the low hydrogen to carbon ratio of the coal, before it can be synthesized to methanol (International Renewable Energy Agency (IRENA), 2021). Syngas composition can be characterized with the stoichiometric number S, which is defined as:

$$S = \frac{n_{H_2} - n_{CO_2}}{n_{CO} + n_{CO_2}}. \tag{19}$$

It compares the molar amounts of the different gas components included in the syngas. Ideal S value for methanol synthesis is 2 or slightly above. Values over 2 indicate an excess amount of hydrogen for ideal formation, and correspondingly values below 2 indicate a hydrogen deficiency. (Olah, et al., 2018)

The conversion of syngas to methanol can be described with the following reaction equations: (Ott, et al., 2012)

$$CO + 2\,H_2 \leftrightarrow CH_3OH\ ;\ \Delta H_{300K} = -90.77\ kJ/mol, \tag{20}$$

$$CO_2 + 3\,H_2 \leftrightarrow CH_3OH +\ H_2O\ ;\ \Delta H_{300K} = -49.16\ kJ/mol, \tag{21}$$

$$CO_2 + H_2 \leftrightarrow CO +\ H_2O\ ;\ \Delta H_{300K} = +41.21\ kJ/mol. \tag{22}$$

Both reactions that produce methanol (equations 20 and 21) are exothermic, and they also decrease volume when proceeding. According to Le Chatelier's principle, methanol conversion is therefore favored by increasing pressure and decreasing temperature. As all the presented reactions are reversible, they are limited by their reaction equilibriums, which change based on the prevailing process conditions. (Olah, et al., 2018)

In recent years, there has been a big push towards direct methanol production via hydrogenation of CO_2, without using fossil fuels. Utilized CO_2 could either be sourced from the environment or captured before it is released to the environment, and the used hydrogen could be produced with renewable energy. (Bowker, 2019) Compared with the conventional syngas process, direct conversion from CO_2 would generate less heat as can be seen from its main reaction (equation 21), and its endothermic side-reaction (equation 22) could also additionally decrease the heat released during green methanol conversion. (Cui & Kær, 2020)

2.6.1 Green Methanol Synthesis

Traditional syngas to methanol reactor types, with proper modifications, should also be suitable for CO_2 to methanol synthesis processes. These gas-phase catalytic fixed-bed reactors can be separated into two main types, depending on their method of heat removal from the catalyst beds. These types are adiabatic reactors, which have no internal cooling, and isothermal reactors, which have integrated internal cooling. Adiabatic reactors can have multiple catalyst beds, usually with gas quenching between the beds being used to control the temperatures. Because isothermal reactors need cooling tubes or cooling plates inside the reactor for heat removal, it makes this reactor type more complex and costly compared to adiabatic reactors. Isothermal reactors can be either water-cooled or gas-cooled. (Cui & Kær, 2020)

The usual catalyst material in the industry is CZA (Cu, ZnO, Al_2O_3). This material has been in use since the 1960s. It has evolved slightly, mainly its longevity has been increased by adding components such as magnesium, but essentially it has stayed the same. Green methanol synthesis produces significant amounts of water (according to equation 21), which accumulates to the outlet of the reactor bed, which in turn decreases catalyst activity and longevity. (Bowker, 2019) This problem could be addressed through a two-step methanol synthesis process, where CO_2 would first be hydrogenated to CO and the forming water removed, before converting the formed CO to methanol. This and other water removal technologies are in development, but in this thesis the focus is kept on direct CO_2 to methanol hydrogenation. (Cui & Kær, 2020)

Usually allowed methanol synthesis reactor temperature range is 180-280 °C, as temperatures outside this range may increase wax condensation in the catalyst bed and catalyst deactivation by sintering. In a 2020 modelling study, which compared different methanol synthesis reactor types, outlet temperatures that were in the accepted operation range were also achieved with a single-pass adiabatic reactor, when the CO content in the synthesis feedstock was kept low. This suggests that due to the low reaction heat compared to traditional syngas conversion, simple and cost-efficient single-pass adiabatic reactors could potentially be used when producing green methanol directly from only CO_2. Based on the same simulation study the water-cooled reactor would have a slightly better performance in CO_2 hydrogenation between the two isothermal reactor types, with it having a better yield and lower hot-spot temperatures than the gas-cooled reactor, but all three traditional methanol synthesis reactor types show potential for direct CO_2 to methanol conversion. (Cui & Kær, 2020)

Traditional operation pressures of methanol synthesis reactors are usually between 50 and 100 bar. Operation pressures that are close to the syngas production conditions are usually preferred, because a small pressure difference between the feedstock production processes and the synthesis process is favorable from an economic standpoint, as it reduces the energy needed for gas compression. However, as mentioned earlier in the work, lowering the pressure in the synthesis reactor will result in a lower methanol yield per pass. (Bozzano & Manenti, 2016)

The methanol synthesis process can be divided into three subprocesses, compression of feedstocks, preheating and reactor feeding, and separation of produced methanol. The gas feedstocks must first be compressed to the operation pressure of the reactor before they are mixed. Then the mixed feedstocks are preheated and fed to the reactor. In the third and final subprocess, methanol is separated in a distillation column. Before it is distilled, the unreacted CO_2 and H_2 gases are first separated from the product stream in a flash vessel. (Pérez-Fortes, et al., 2016) A simplified configuration of the considered methanol synthesis process is presented in Figure 10 below.

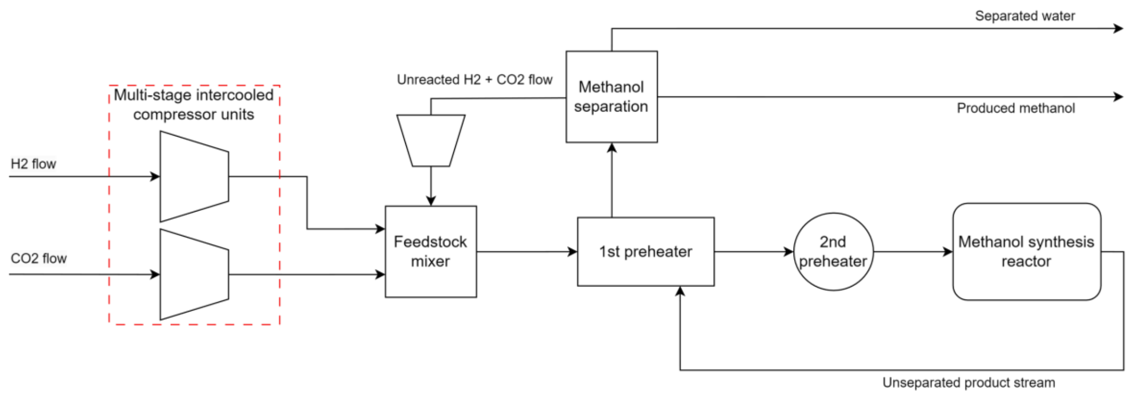

Figure 10. *Simplified methanol synthesis system configuration. Based on sources* ***(Luyben, 2010; Pérez-Fortes, et al., 2016)***

Different compressor stages and their intercoolers are not presented for the compression of original feedstocks in Figure 10 to simplify the flowsheet. Additionally, the methanol separation process is not visualized at all. Because the separation process itself is also quite complex, it was totally left out of the scope of this thesis and is thus not discussed further. More about the separation process can be read from sources (Pérez-Fortes, et al., 2016; Marlin, et al., 2018)

Like traditional syngas-based production methods, direct CO_2 to methanol synthesis also requires recycling of the unconverted gases in the product stream back to the reactor, as can be seen in the previously presented process flowsheet. This is due to the low single-pass yield of the process (15 to 35 % of CO_2 converted), the single-pass yield can be defined in percentages as follows:

$$y_{MeOH} = \frac{n_{MeOH_{out}}}{n_{CO_{2_{in}}} + n_{CO_{in}}} \cdot 100, \tag{23}$$

where the molar amount of produced methanol $n_{MeOH_{out}}$ per pass is compared to the molar amount of carbon-based (CO_2 and CO) feedstocks supplied to the reactor. (Cui & Kær, 2020) A small amount of the recycle stream (about 1 %) must also be purged to avoid the accumulation of impurities and inert gases in the system. (Bozzano & Manenti, 2016; Pérez-Fortes, et al., 2016)

Liquid-phase synthesis processes might replace gas-phase methanol synthesis in the future as they would allow more efficient heat removal from the reaction, leading to improved temperature control, and they would also require lower recycling ratios of product gases compared to gas-phase reactors. Unfortunately, liquid-phase reactors have not yet been applied for methanol production due to modelling and scale-up issues. (Bozzano & Manenti, 2016) Quite confusingly liquid-phase synthesis seems to refer to a conversion process where catalyst particles are mixed in an inert liquid, which the feed gas passes through, meaning that the reaction happens inside this liquid, instead of referring to the phase of the reactants themselves. (Ghosh & Seethamraju, 2021; Bozzano & Manenti, 2016; Kung, 1992)

Another possible reactor type for future methanol production could be a catalytic membrane reactor. Because the methanol yield is limited by reaction equilibrium, it would be advantageous to selectively remove produced methanol and water during the reaction to increase total yield. This could be achieved with membrane reactors, which would separate the condensable products, of methanol and water, from the gases. (Gallucci, et al., 2004)

2.6.2 Operation Flexibility of Methanol Synthesis

Only the technologically ready gas-phase fixed bed reactors are discussed in this subchapter, as they represent the currently commercially available synthesis reactor technologies. Because PtX concepts are commonly seen as a power grid balancing option, at least the electrolysis must be operable dynamically. To avoid very large hydrogen storages in Power-to-Methanol systems, the methanol synthesis process should also be flexible. (Dieterich, et al., 2020)

Lurgi AG have claimed that their water-cooled reactors are very flexible in traditional syngas-based methanol conversion with a minimum load from 10 to 15 %, and a load change from 0 to 100 % in just few minutes. Fast load changes are supposed to be possible with water-cooled reactors due to the large thermal capacity of the surrounding cooling water, which would ensure stable reactor behavior. (Dieterich, et al., 2020)

One problem in flexible load operation of CO_2 hydrogenation is the conversion behavior during start-ups. In one experimental test with a water-cooled fixed bed reactor, it took significantly long to reach steady state process conditions and conversion (about 80 to 100 hours) after process restarts. This slow increase in CO_2 conversion after restarts should be investigated further to see how it would affect flexible operation of CO_2 to methanol reactors that would be subjected to regular start-ups and shutdowns due to fluctuating hydrogen availability. (Pontzen, et al., 2011)

Currently, there is still very limited data available about the partial load operation of methanol synthesis reactors in CO_2 hydrogenation regarding actual load limits and ramp rates. Even though there does not seem to be publicly available experimental or theoretical data concerning the subject, some modelling studies do still assume a level of load flexibility for the synthesis process. In a 2021 modelling study the authors assumed a minimum reactor load of 10 % with an isothermal reactor (Chen & Yang, 2021), and in a 2022 modelling study with an adiabatic reactor the authors used a minimum load of 50 %, with a ramp time of 1 hour (ramp rate of 50 %/h) to study the flexible operation and energy efficiencies of different partial loads (Cui, et al., 2022).

In 2023 a German company MAN Energy Solutions however claimed that their Flex-Methanol concept, which is a modular green methanol conversion unit, could handle fast load ramping and a production load range of 10 to 100 %. Low operation pressure of 40 bar was suggested to be the key innovation, which would allow the modular methanol plant to operate with fluctuating energy availability, and varying hydrogen and CO_2 feed-stocks. It was also claimed that because of the synthesis flexibility, no costly hydrogen buffer tanks are required in their concept. (MAN Energy Solutions, 2023)

Conventional chemical processes are typically operated at steady state conditions, and in renewable chemical production operation flexibility is currently mainly achieved with energy storage solutions, particularly with the use of compressed hydrogen storage. It should also be noted that even if the flexible operation of chemical reactors shows some promise, it is not enough by itself. There can exist a big disparity between the flexibility of different process units in a chemical plant, which is often ignored in scientific literature. For example, load flexibility disparity between conversion and separation processes would require additional storage applications for intermediate products, and it could also complicate the heat integration system of a chemical plant. (Chen & Yang, 2021)

3. MATHEMATICAL MODELLING

Mathematical modelling and simulation are important tools that can be used to support designing, evaluating, and analyzing different systems. The definition of what constitutes as a system is very broad and application dependent. Generally, a system is used to mean a combination of components or parts that collectively work to perform a desired function. Good models allow simulations to be used for testing, which is less costly than carrying out tests on actual systems or prototypes. (Spong, 2023)

A model is a mathematical representation, which approximates physical reality. One method of classifying mathematical models is separating them based on how they are derived. *"Models from first principles"* are models that are based on physics, and they are typically differential or difference equations. *"Black box models"* are models that are based on measured data, which is used to identify input/output structures of systems. *"Gray box models"* are a combination of the two previous classifications, where measured data is used to complete a model. For example, by identifying modelling parameters that can be used with an already assumed mathematical model structure. (Spong, 2023)

One other key classification between mathematical models can be determined based on the role of time in these models. This separates mathematical models into dynamic and static models. A model which has no dependency on time is a static model, and one where the results instead vary based on the modelled time is a dynamic model. This difference between the models can be compared to the difference between looking at a photograph and looking at a video. (Birta & Arbez, 2007)

Dynamic models can further be divided into two classes according to how changes occur in the modelled system as time goes by. In discrete-time systems changes can occur only at certain times, but in continuous-time systems their behavior can change smoothly and continuously over time as the term suggests. (Gray, 2010) The modelling task in this work can be considered as continuous-time dynamic modelling because of the modelled process and how its behavior is wanted to be analyzed over time.

3.1 Dynamic Modelling Practices and Challenges

It is challenging to explicitly define best practices in the field of dynamic modelling, but practices that can be identified as *"best"* should be rule-like, making them easy to interpret and implement. A few highly agreed upon practices include involving the customers of the modelling work in the modelling process, clearly identifying the purpose and focus of the modelling task, trying to approach the model conceptualization from different perspectives, developing models first through simpler versions, and adding complexity after it becomes necessary to model a system in more detail, comparing the modelling results to behavior of real systems, and making sure that the modelling process revolves around the considered problems. (Martinez-Moyano & Richardson, 2013)

Dynamic system modelling is usually an iterative process consisting of work steps that include model development, implementation, testing, result analyzing, and model validation. However, commonly encountered dynamic system modelling tasks often consist of individual subsystems that belong to different engineering and research fields, and when modelling such systems, it is often advisable to model the subsystems first separately and to join them together later. To model and analyze such complex systems, in addition to understanding the behavior of individual subsystems, it is important to understand their interactions between one another. (Yang & Abramova, 2022)

Some dynamic modelling challenges can be identified from the earlier paragraphs of this chapter. The complexity of a modelled system can make choosing what behavior is relevant to include in detail, and when to simplify the model, very challenging. If using or creating models that are based on measurement data, there is a risk of that the model is or will be overfitted to model specific sample data. Validating the model behavior can also be challenging or almost impossible if there is no measurement data of a real system, that could be used for comparison.

3.2 Modelling Approach in This Work

In this work, a Power-to-Methanol plant concept is developed and attempted to be modelled to study the behavior of its subprocesses, and to develop control solutions for this plant. This modelling task consists of five separate subprocesses, which were discussed earlier in Chapter 2. The modelling was decided to be approached by doing and testing the subprocesses models separately at first, like suggested earlier in this chapter, to make the model implementation and result analyzing phases easier. Since modelling based just theoretical physics and chemistry was assumed to be quite complex the approach was not limited to only *“models from first principles”*, and other model types could also be used if the modelling task was made less complex by them.

The modelling software chosen for use was Simulink, which is a MATLAB based simulation environment. It was selected because of its common use in the industry and easily available support and documentation. Regarding future continuation of this work, implementing and testing control solutions is also very easy to do in MATLAB Simulink.

4. MATERIALS AND METHODS

The main objectives of this thesis work were to develop and model a Power-to-Methanol plant concept, so that control solutions for it could be developed and later tested. The work as whole has a target to gain more knowledge about common automation challenges related to PtX concepts. The reason the modelled plant had to first be designed in this work was that there was no available plant reference that could be utilized. The modelled plant concept was built based on a literature review part of the work, which had to be done first. In the experimental part of the work, simulation models describing this plant's subprocesses were developed and based on the results given by these models, possible control solutions could be proposed for the individual subprocesses. However, the proposed control solutions were not yet tested in this thesis work.

The literature review was done based on available scientific literature, and it is covered in Chapter 2. The literature review focused on comparing subprocess alternatives to each other and understanding their principles and operation flexibility. Chapter 3 gives a little background for mathematical modelling and explains how the modelling task was approached. The aim of this chapter was to work as a bridge between the literature and applied part of this work. The modelled plant concept is presented in the first subchapter of Chapter 4, and the model construction and modelling methods of its individual subprocesses are covered in the subchapters that follow it. The results of this thesis work are analyzed in Chapter 5. These results include open loop step responses of the created simulation models and control solutions that could be proposed based on the dynamic behavior observed in these tested simulations runs.

To develop and test stabilizing plant controls, modelling just the normal operation range of the plant was assumed to be enough. Because of this, the models were not developed or expanded to always give reasonable simulation results outside the designed operation ranges, or in all plausible erroneous operating situations. Fitted equations based on available process data or data curves were developed and used when it was possible to simplify the modelling this way. Also, because the modelling task's scope was so extensive, not all model parameter values could be found from reference literature like was originally planned, and some values had to be set for the models instead only according to the author's own discretion. All the parameter values used in the modelling are provided in the appendices of this work.

The open loop behavior, which is here used to refer to system behavior when no controls are implemented or included, of the developed models was tested in this work by doing step response simulation tests with chosen input variables. These tests were analyzed both to identify possible control variables of the plant and to see if the models behaved as expected. The initial input values from which individual simulation runs were started were chosen by the author, and these initial conditions are presented together with the test simulation results in Chapter 5.1.

Some modelling equations are presented for the first time in the following subchapters, while those that have been already presented in the literature review part are just referenced if utilized. In the literature review part not all units of the presented equations were covered as the equations were mostly presented as just theory background, but in the following subchapters the units used in the modelling are provided. However, the units are only defined in cases where they differ from SI-units, so that the work is not unnecessarily lengthened without reason. The calculation units that were used can also be more easily checked from the symbol list provided at the start of this work.

In this work different flow rate definitions such as molar flow rate ($\dot{n}$), and mass flow rate ($\dot{m}$) are very commonly used in the utilized modelling equations, and they should not be mistaken for derivatives. To distinguish them from each other, dot notation is only used for flow rate definitions and derivatives are instead always written open as complete division calculations. Variables that were modelled as time dependent are denoted in the presented equations by including time t in brackets after them, like $a(t)$ for an example.

4.1 Power-to-Methanol Plant Configuration

In this subchapter, the green methanol plant concept modelled in this work is presented. This plant concept was built by combining subprocess technologies that were deemed suitable based on the literature review part of this work. The process choices that were made when developing the plant concept and the reasoning behind these choices are summarized in a list below. To keep the scope of the study reasonable, some simplifications and omissions to the plant concept had to be made, which are also covered in a separate list below.

The following process choices were made when developing the plant configuration:

1. PEM electrolyzer was chosen for hydrogen production, because based on the literature review, it is the most suitable electrolyzer type for flexible operation (Rajeshwar, et al., 2008; Carmo, et al., 2013; Buttler & Spliethoff, 2018).

2. Electrolysis was considered to happen in a pressure level (50 bar), which would also be high enough for the methanol synthesis, meaning that no compressors were included in the main hydrogen feed pipeline.
3. A metallic type I high-pressure gas tank was chosen for hydrogen storing, because of its simplicity and suitability for stationary applications (Hassan, et al., 2021). The gas storage was assumed to operate in pressure levels above the methanol synthesis pressure (>50 bar), so no compressors were included in the discharge pipeline of the hydrogen storage (Barthelemy, et al., 2017).
4. The simplest post-combustion capture unit based on chemical absorption was chosen for CO_2 capture in the plant. This carbon capture method was chosen because of its technological maturity. The most common chemical solvent, which is monoethanolamine (MEA) was chosen as the solvent with 30 wt-% solution. (Bui, et al., 2014; Mumford, et al., 2015; Oko, et al., 2017; Wilberforce, et al., 2021)
5. A liquid high-pressure tank was chosen for CO_2 storage, with external refrigerant cooling being used for the CO_2 liquefaction process. These CO_2 storage system choices were made because of similar configurations that were presented in referenced literature. (Chen & Yang, 2021; Sollai, et al., 2023)
6. The pressure of the liquid CO_2 storage was assumed to be the same as in the main CO_2 feedline, so no compressors were included in the discharge pipeline of the CO_2 storage (Chen & Yang, 2021).
7. A single-pass adiabatic fixed bed reactor was chosen for the methanol synthesis as it was suggested that the lower heat generation of CO_2 hydrogenation process, compared to traditional methanol synthesis, would allow this simple reactor type to be used (Ott, et al., 2012; Cui & Kær, 2020).

The following process simplifications and omissions were made when developing the plant configuration:

1. Purification and product separation technologies of neither the water electrolysis nor the methanol synthesis were studied in this thesis and were therefore not included in detail in the developed plant configuration.
2. Flue gas pretreatment or posttreatment (water washing) were not considered parts of the carbon capture subprocess and were therefore not included in the considered plant configuration.

A flowsheet of the modelled Power-to-Methanol plant based on the listed technology choices and simplifications is presented below in Figure 11. To make the plant flowsheet more compact, multi-stage compression trains are presented in it with singular compression units, instead of showing multiple compression stages and intercoolers. Different subprocesses are also separated with dashed lines and named in the flowsheet to increase its readability.

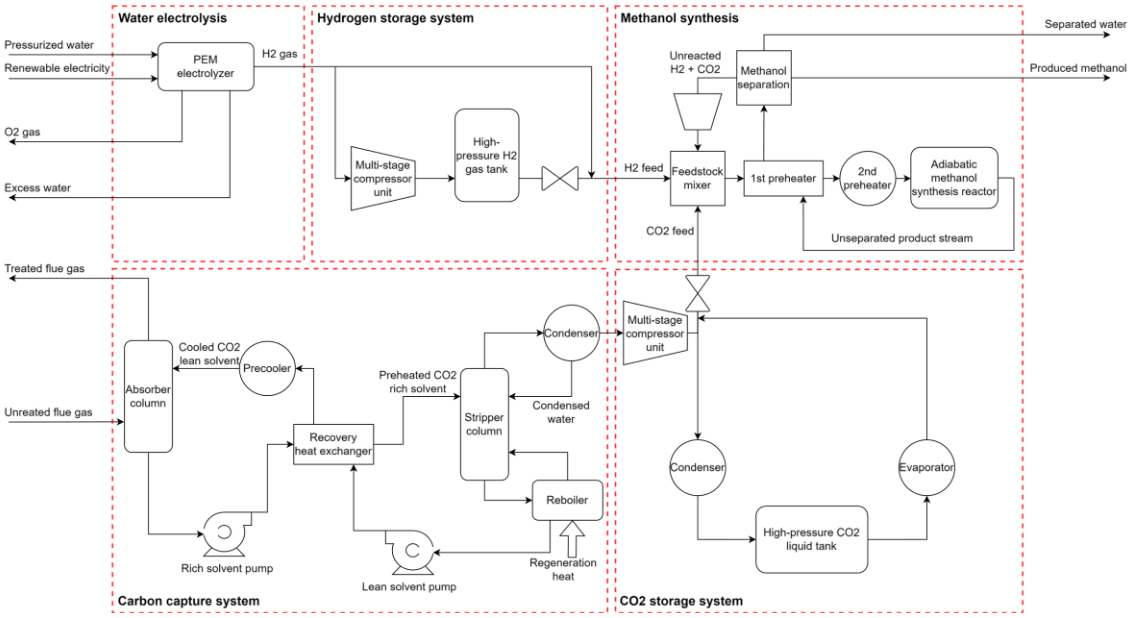

Figure 11. *Flowsheet of the Power-to-Methanol plant concept considered in this work.*

The following subchapter focuses on the model construction process and the eventually done simulation runs. It was included to provide a little more background on how the modelling task was completed, and how and why the test simulations were both run and analyzed.

4.2 Model Construction and Simulation

The model implementation and simulation in this work were done with MATLAB Simulink, as mentioned earlier. The modelling was approached by first constructing subprocess models separately from each other. During the model development, however, it was always kept in mind that these separate models would need to be later joined to each other to produce a one single simulation model of the entire plant. But in the end, simulation results of the entire plant model were not analyzed in the work at all.

There were two reasons for the decision not to analyze tests done with the entire plant model. The first reason was simply that presenting simulation results individually for the original subprocess models was assumed to be more reader friendly and to take less time, as then all the presented tests would not include all possible result values of the entire plant. The second reason was that by testing the subprocesses separately, it was assumed that running tests where the simulation results would stay in working range of the models would be easier.

This latter mentioned problem of having to not exceed the working ranges of the models in the tests was caused by modelling choices which were done in the model development phase, when it was decided that it would be enough to only model the normal operation ranges of the subprocesses. This problem especially concerns modelled subprocesses, which included fitted equations, but using fitted equations in the modelling was considered necessary in some cases so that the modelling task's complexity could be reduced enough.

Other common ways in which the modeling task was simplified in this work include treating some of the actual process variables as input values or constants instead, like for example some pressure, temperature, and some fluid property values, omitting some parts of the considered plant from the modelling scope, ignoring heat transfer with the environment, and assuming or estimating some process variable changes to be instantaneous instead of them happening smoothly.

Simulation test runs were needed to be analyzed in this work to check that the models behaved as expected and were implemented correctly, and to identify possible control variables. The analyzed test runs were step response tests with input variables that were deemed important from a control perspective. The initial input values of the analyzed tests were chosen so that the subprocess models were stable at the start and the tested input changes so that the results stayed in working ranges of the models like discussed previously. The initial input values of the tests are presented together with the analyzed simulation results in Chapter 5.1.

The following subchapters focus on the modelling methods of the subprocess technologies, which were chosen for the developed Power-to-Methanol plant concept. The aim of the following chapters is to describe the used modelling equations and final model structures in detail, and to provide explanations for why some of the simplifications and assumptions were utilized during the development phase of the subprocess models.

4.3 Proton Exchange Membrane Electrolysis Modelling

For the chosen PEM Electrolyzer, a conventional heat management method is an excess flow of the process water. However, process water flow independent temperature control methods with separate coolant circulation are also studied and developed. (Wirkert, et al., 2020) The conventional heat management method was chosen for the process model, which means that because excess water flow will always be provided the production of hydrogen can only be limited by the operation current. The amount of produced hydrogen can therefore be directly calculated with equation 9 in mol/s, when using SI-units. The other outlet flows can be calculated from the stoichiometric reaction equation (presented in equation 1), like suggested earlier in the theory part. The power consumption of an electrolyzer can on the other hand be calculated from equation 5.

To use these mentioned equations 9 and 5, models for the U_{cell}, and η_F values must be defined. Next, the modelling of PEM electrolyzer cell voltage U_{cell} is presented. The modelling method of U_{cell} used in this work is based on some of the alternative equations used in a study that focused on developing an electrolyzer modelling tool. To better understand the equations, which are presented next, the original source should be read, which gives insight to the origins and simplifications of these equations. (Järvinen, et al., 2022) In this thesis work, only the final equations that were used are presented.

The voltage of an electrolyzer consists of four different potential terms:

$$U_{cell}(t) = U_{ocv} + U_{ohm}(t) + U_{act}(t) + U_{con}(t), \tag{24}$$

which are open circuit voltage U_{ocv}, ohmic overpotential U_{ohm}, activation overpotential U_{act}, and concentration overpotential U_{con}. The equation used in this work for the open circuit voltage of a PEM electrolyzer has the following form:

$$U_{ocv} = U_{rev} + \frac{RT}{zF}\ln\left(\frac{\left(p_{ca}-p_{H_2O_{vap}}\right)\left(p_{an}-p_{H_2O_{vap}}\right)^{\frac{1}{2}}}{p_{ref}^{\frac{3}{2}}}\right), \tag{25}$$

where T is the operation temperature of the modelled PEM electrolyzer, p_{ca} pressure at the cathode, p_{an} pressure at the anode, $p_{H_2O_{vap}}$ saturated vapor pressure of water, and p_{ref} a standard reference pressure of 100 000 Pa. The other variables of the equation 25 have been presented and discussed earlier in this work's theory part and were not listed again here. To use the previous equation, the reversible potential U_{rev} must be determined in the electrolyzer's operation temperature, and for this a simple linear approximation was used:

$$U_{rev} = 1.229 - 0.000846 \cdot (T - 298.15). \tag{26}$$

The saturated vapor pressure of water was determined from an experimental equation that had the following form:

$$\log_{10}\left(p_{H_2O_{vap}}\right) = 35.4462 - \frac{3343.93}{T} - 10.9 \cdot \log_{10}(T) + 4.1645 \cdot 10^{-3} \cdot T, \tag{27}$$

where the only variable is again the operation temperature. (Järvinen, et al., 2022)

The ohmic overpotential in the model was determined from Ohm's law:

$$U_{ohm}(t) = rj(t), \tag{28}$$

where r is the total area specific electrical resistance of the electrolyzer cell, and j is the operating current density, for which units of Ωcm^2 and A/cm^2 were used in the model. For activation overpotential a combined equation that takes both electrodes into account was used instead of using individual equations for the anode and the cathode. The used equation is an approximated solution of Butler-Volmer equation, that was derived in the original source material. The activation overpotential was calculated in the model as follows:

$$U_{act}(t) = \frac{RT}{zF\alpha} \sinh^{-1}\left(\frac{j(t)}{2j_0}\right), \tag{29}$$

where α is a unitless electron transfer coefficient, j is operating current density, and j_0 exchange current density. The concentration overpotential was calculated in the model with the following equation:

$$U_{con}(t) = -\frac{RT}{zF} \ln\left(1 - \frac{j(t)}{j_L}\right), \tag{30}$$

where j_L is the limiting current density. (Järvinen, et al., 2022)

It can be seen from the previously presented equations 25-30, that the electrolyzer cell voltage is dependent on the operation temperature T, pressure at the cathode p_{ca}, pressure at the anode p_{an}, total area specific resistance of the cell r, electron transfer coefficient α, exchange current density j_0, limiting current density j_L, and finally the operation current density j. However, the theory behind some of these variables that are needed could not be covered in detail to keep the work's scope reasonable. Some of these variables, like r and j_0, are also temperature dependent themselves. (Sood, et al., 2020) This means that to model proper temperature dependency of the cell voltage, these dependencies would also need to be considered. In this work it was however decided that when modelling the cell voltage all parameters other than the operating current density j would be considered as constants, and the design operating temperature value would therefore be used. Because the operating temperature change is still modelled in the developed model structure, this means that the cell voltage modelling and the cell temperature modelling are done independently of each other. The electrolyzer cell voltage values given by the modelled design operating conditions (T_{cell}, p_{ca}, p_{an}), and parameter values (r, j_0, j_L, α) are plotted below in Figure 12 as a function of operation current density. The pressure at anode and cathode were estimated in this work to both be equal to the decided design operation pressure of 50 bar ($p_{ca} = p_{an} = p_{cell}$). The parameter values used in the electrolyzer cell voltage modelling can be checked from Appendix A of this work.

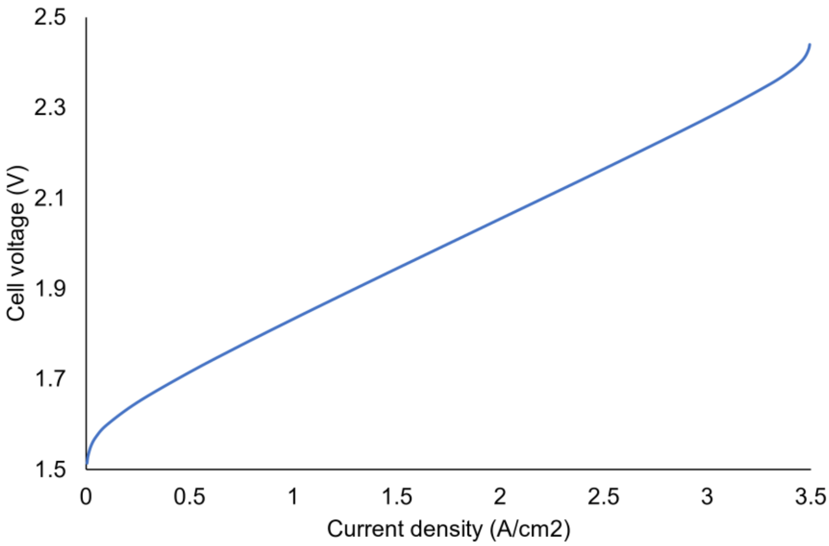

Figure 12. *Cell voltage values of the modelled PEM electrolyzer.*

Multiple Faraday efficiency models have been developed for alkaline electrolyzers, which are usually dependent on operation temperature and operation current density. However, for PEM electrolyzers gas pressure has a stronger influence on the Faraday efficiency than temperature, and its effect should therefore be included if a PEM electrolyzer is modelled. In 2020 modelling study, an empirical Faraday efficiency model that is only based on operation pressure was developed for PEM electrolyzers. (Yodwong, et al., 2020) In this thesis work, a newer model that also accounts for the operation temperature was used. This model equation is presented below:

$$\eta_F(t) = \exp\left(\frac{-b_1 T_{cell}(1-(p_{cell}-1)b_2)}{j(t)}\right) \tag{31}$$

where T_{cell} and p_{cell}, are the operation conditions of the modelled PEM electrolyzer, j is the operation current density, and b_1 and b_2 are model parameters that should be determined from experimental data. In the original source it was suggested that for PEM these values would be $b_1 = 0.1$ and $b_2 = 0.3$, and that with different values this same equation should also be suitable for modelling alkaline electrolyzers. When using equation 31 the pressure should be given in bar and temperature in Celsius units, while the current density should still be in SI-units (A/m^2). The efficiency values given by the equation are unitless values between 0 and 1. (Antoniou, et al., 2022)

When testing the previously presented Faraday efficiency equation, it was however noticed that to get similar results as in the source study, the b_2 value should instead be

-0.3. The modelled Faraday efficiency is plotted as a function of the operation current density below in Figure 13 in constant temperature of 30 °C, and constant pressure of 50 bar. Because the operation voltage was already modelled only depending on the current density at this point, the same decision was made for the Faraday efficiency modelling. This means that the Faraday efficiency was also modelled based on the design operation temperature value being considered as constant, and therefore the operation efficiency (according to equation 7) was in its entirety modelled to be dependent only on the operation current density in this work.

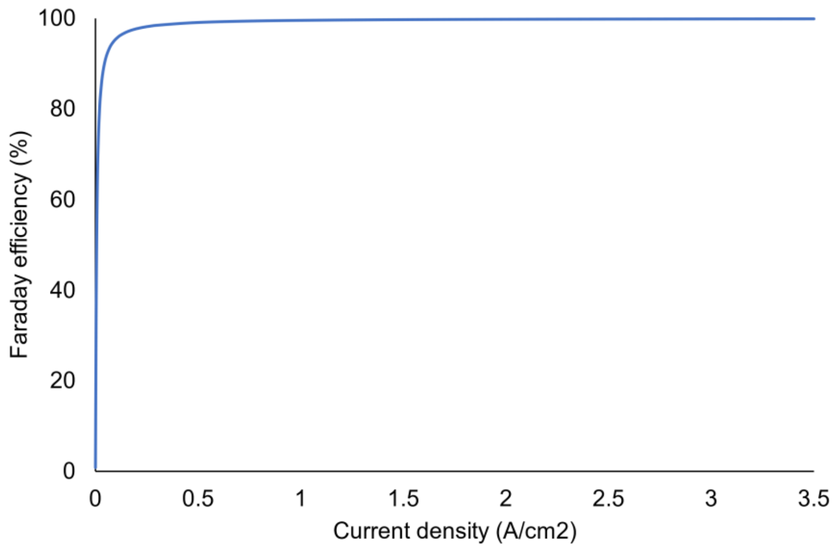

Figure 13. *Faraday efficiency values of the modelled PEM electrolyzer, with T_{cell}=30 °C, p_{cell}=50 bar, b_1=0.1, and b_2=-0.3.*

Next the modelling of the operation temperature change is explained, but again it is important to keep in mind that this temperature value is modelled only to test the electrolyzer cooling, and it is not used to model changes in the electrolyzer efficiency. With the chosen cooling solution, the operation temperature of the electrolyzer changes based on the amount of excess water flow and the excess heat generated during operation. This change can be calculated from the energy balance of the electrolyzer, as follows:

$$\frac{dT_{op}(t)}{dt} = \frac{\dot{m}_{H_2O_{in}}(t)c_{H_2O}\big(T_{in}(t)-T_{op}(t)\big)+\dot{Q}_{heating}(t)}{m_{PEM}c_{PEM}}, \quad (32)$$

where $\dot{m}_{H_2O_{in}}$ is the water flow in, c_{H_2O} the specific heat capacity of water, T_{in} the water flow's inlet temperature, T_{op} the operation temperature of the PEM electrolyzer, $\dot{Q}_{heating}$ the heat rate that is generated during operation, and m_{PEM}, and c_{PEM} are the mass and specific heat capacity of the electrolyzer system respectively. In this work, heat loss to environment was neglected when solving the operation temperature change from the heat balance.

To be able to calculate the previously derived temperature differential equation, the amount of excess heat must be defined. The power consumption of an electrolyzer system was defined earlier in equation 5. Now if it is assumed that all the excess power generates heat in the system, then this amount can be calculated by simply subtracting the amount of energy that was consumed by the hydrogen production from the actual total power consumption of all cells, leading to the following equation:

$$\dot{Q}_{heating}(t) = NI(t)\left(U_{cell}(t) - U_{tn_{HHV}}\eta_F(t)\right), \tag{33}$$

which was derived from equations 5 and 7 presented earlier in the work. The HHV definition of the electrolyzer efficiency was chosen to be used in the modelling and a constant value of 1.482 V (Ulleberg, 2003) was used for the HHV thermoneutral voltage $U_{tn_{HHV}}$ in the electrolyzer model.

The developed model structure of the PEM electrolyzer is visualized below in Figure 14. The model has three input variables, which are the operation current, and the water temperature and mass flow rate into the electrolyzer. Additionally, the operation temperature value must be initialized before any simulation runs.

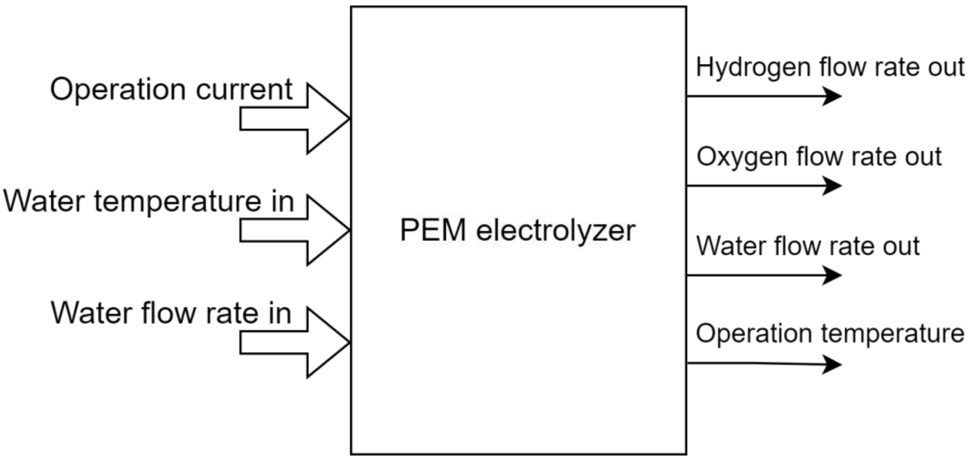

Figure 14. *Visualization of the PEM electrolyzer model structure.*

The simplifications and assumptions used in the creation of the PEM electrolyzer simulation model are summarized below:

1. Mass was assumed to not accumulate to the electrolyzer system, meaning that the inlet and outlet mass flows were modelled as equal.
2. The electrolyzer system was modelled at constant pressure of 50 bar, which was assumed to be the pressure of both electrode sides in the model.
3. Electrolyzer cell voltage was modelled only as a function of the operation current.
4. Faraday efficiency was modelled only as a function of the operation current.

5. Constant heat capacity and thermoneutral voltage values were used in the modelling instead of them depending on temperature.
6. Heat transfer to the environment was not modelled.
7. No purification or handling of product streams were modelled, all the substances in the model are instead considered to have totally pure and unmixed flows after the electrolyzer.

4.4 Post-combustion Carbon Capture System Modelling

As specified earlier, the simplest post-combustion CO_2 capture process was chosen for the considered plant configuration, with 30 wt-% MEA solution being used as the solvent. The most important process variables were identified to be the solvent CO_2 loading (defined in equation 18), and the temperature level at different parts of the carbon capture system. Pressure levels, however, were not modelled in the developed simulation model.

To estimate somewhat realistic process dynamics, solvent sumps were modelled at the bottom of the absorber column and the stripper column (or the reboiler unit). In real systems, these sumps along with buffer tanks have a major effect on process lag time. (Tait, et al., 2016) In this work, the stripper column and the reboiler unit were combined into a one singular modelled process component. The solvent sumps were modelled as ideal liquid mixing tanks, where new CO_2 concentrations would be reached infinitely fast when solvent would flow into the sumps. In the model it was assumed that the solvent volume in the sumps would not depend on the CO_2 loading or operation temperature, and because the volume flow rate of the solvent was modelled as equal in all parts of the system, the liquid volume in these sumps would stay constant.

The carbon capture model structure is explained next. To make the explanation easier to follow, it was written by following the solvent flow once through the entire capture system, starting from when the solvent flow enters the absorber column. When the solvent flows through the absorber, CO_2 is absorbed by it either until its maximum loading value is reached (defined as constant in the model), or until 98 % of CO_2 has been captured from the flue gas flow. This 98 % value was given as an upper limit, because it was assumed that actual systems could never reach 100 % capture rate, and to make sure that nonexistent CO_2 would not be generated by the absorber model. This previously explained method was used to define the following model values: CO_2 loading of the solvent before it enters the solvent sump $X_{sump_{in}}$, the amount of captured CO_2 in moles per second, and the carbon capture percentage.

After the absorption process has happened, the solvent flows into the solvent sump mixing with it, which changes the CO_2 loading in the sump. The CO_2 loading change in the sump can be solved from the sump's mass balance. The volume flows in and out were assumed equal in the model, which means that the mass flows of unloaded solvent in and out must also be equal, because the volume of the solvent was assumed to not depend on CO_2 loading nor temperature. These assumptions lead to the following mass balance solution, which was used in calculating the CO_2 loading change in the modelled absorber solvent sump:

$$\frac{dX_{sump}(t)}{dt} = \frac{\dot{n}_{CO_2in}(t) - \dot{n}_{CO_2out}(t)}{m_{unl_{sump}}} = \frac{\dot{m}_{unl_{in}}(t)\left(X_{sump_{in}}(t) - X_{sump}(t)\right)}{m_{unl_{sump}}}, \tag{34}$$

where $\dot{m}_{unl_{in}}$ is the mass flow rate of unloaded solvent in, $X_{sump_{in}}$ the CO_2 loading at the sump inlet in mol/kg, X_{sump} the current CO_2 loading in the sump, and $m_{unl_{sump}}$ the mass of unloaded solvent in the sump, which stays constant in the model based on earlier assumptions.

In the developed simulation model, the temperature profile inside the absorber was modelled as uniform, meaning that the whole system and its outlet flows were modelled with the same temperature value T_{abs}. In the model, the heat released by absorption therefore warms both flows that pass through the absorber, and the solvent volume accumulated to the bottom of the column. The temperature change in the absorber column could therefore be derived from the column's total energy balance. Possible heat losses to the environment were not modelled, which resulted in the following differential equation:

$$\frac{dT_{abs}(t)}{dt} = \frac{\dot{m}_{sol_{in}}(t)c_{sol_{in}}(t)\left(T_{sol_{in}}(t) - T_{abs}(t)\right) + \dot{m}_{fg_{in}}(t)c_{fg_{in}}\left(T_{fg_{in}}(t) - T_{abs}(t)\right) + \dot{n}_{CO_{2_{absd}}}(t)\Delta H}{m_{sol_{sump}}(t)c_{sol_{sump}}(t)}, \tag{35}$$

where flue gas flow is denoted with the subscript fg. It is also very important to notice that in this equation the used solvent mass values ($\dot{m}_{sol_{in}}, m_{sol_{sump}}$) include the mass of loaded CO_2, unlike in the previous differential equation that was used in determining the CO_2 loading change in a solvent sump. The heat that is released during absorption can be simply determined by multiplying the molar CO_2 capture rate and the reaction heat of absorption ΔH, for which a constant value was used in the developed model. The specific heat capacity of the inlet solvent flow $c_{sol_{in}}$ changes based on its CO_2 loading, and same with the specific heat capacity of the solvent inside the sump $c_{sol_{sump}}$, but for all the substances in the solvent flow (MEA, water, CO_2), and in the flue gas flow (water, CO_2, N_2,

O_2) constant specific heat capacity values were used to simplify the modelling task. Because the composition of the flue gas was determined to not change in the model, its specific heat capacity $c_{fg_{in}}$ was therefore also a constant.

After the absorber, solvent flows from the bottom of the solvent sump to the recovery heat exchanger, where it is heated with the flow that is coming back from the stripping process. The heat recovery heat exchanger is assumed to be, and modelled as, a counter flow heat exchanger, based on found pilot plant data values. (Notz, et al., 2012) All inlet variables, which include the inlet temperatures of cold and hot fluid sides, and the solvent mass flow rate in both fluid sides can change in the developed model structure. To model how the performance of the heat exchanger depends on these variables, an equation to calculate the temperature difference between the fluid sides was created. The developed equation has the following form:

$$\Delta T_{hx}(t) = \left(-0.0027 \cdot \left(\dot{m}_{unl}(t)\right)^2 + 0.0657 \cdot \dot{m}_{unl}(t) + 0.0066\right)\left(T_{h_{in}}(t) - T_{c_{in}}(t)\right), \quad (36)$$

where $\dot{m}_{unl}$ is the unloaded mass flow rate of the solvent through both sides of the recovery heat exchanger, $T_{h_{in}}$ the inlet temperature of the hot fluid side, and $T_{c_{in}}$ the inlet temperature of the cold fluid side. The fit is based on a simplification that the overall heat transfer coefficient U would stay constant in different operation points, and an iterative solution, where two different equations that can be used to calculate the heat transfer in the exchanger were kept equal:

$$UA\Delta T_{hx}(t) = \dot{m}_{sol_c}(t)c_{sol_c}(t)\left(T_{c_{out}}(t) - T_{c_{in}}(t)\right), \quad (37)$$

where $\dot{m}_{sol_c}$ is the loaded solvent mass flow rate through the cold side of the exchanger, c_{sol_c} its specific heat capacity, $T_{c_{out}}$ the cold side's outlet temperature, and $T_{c_{in}}$ the cold side's inlet temperature. On the left side of the equation U is the overall heat transfer coefficient of the heat exchanger, A the heat transfer area, and ΔT_{hx} the temperature difference between the fluid sides of the heat exchanger. The solutions given by equation 36 are plotted in Figure 15. It is very important to notice that the developed equation 36 can only be used to estimate the behavior of a one specific counter flow heat exchanger that was dimensioned for just this plant modelling task. The modelled exchanger was dimensioned with the following value of $U \cdot A$ = 53 261.94 W/K.

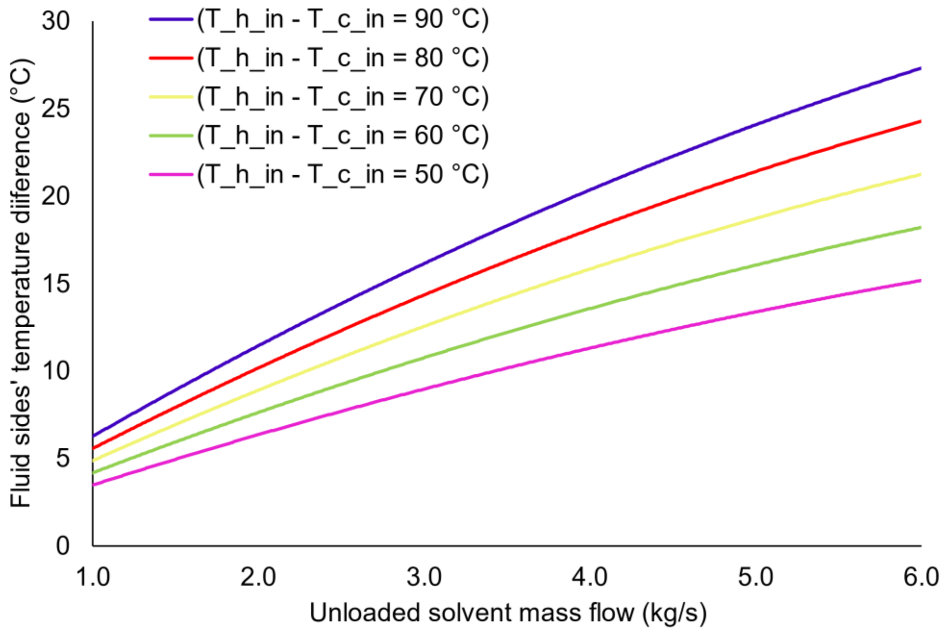

Figure 15. *Fluid sides' temperature difference in the modelled counter current heat exchanger based on inlet temperatures and solvent flow in the CO_2 capture system.*

The outlet temperatures of the heat exchanger were modelled by simply either adding or subtracting the temperature difference that could be solved from the previously discussed equation 36. The outlet temperature of the cold flow side is calculated in the model as follows:

$$T_{c_{out}}(t) = T_{h_{in}}(t) - \Delta T_{hx}(t), \tag{38}$$

and the outlet temperature of the hot flow side as follows:

$$T_{h_{out}}(t) = T_{c_{in}}(t) + \Delta T_{hx}(t). \tag{39}$$

Small error is caused to the outlet temperature values calculated this way, because during the model development the calculations were simplified by assuming an equal mass flow on both sides of the heat exchanger. This was done because it further allowed the assumption that the temperature difference between the fluid sides would be constant throughout the entire length of the recovery heat exchanger. Major error is not caused to the temperature values, because the real difference between mass flows of the fluid sides is just the slight difference that is caused by the CO_2 loading difference between the lean and rich solvent flows.

After the solvent flow has been preheated in the recovery heat exchanger, it is passed to the stripping process, where CO_2 is removed from the solvent by stripping steam. In this work, the stripping process modelling is simplified roughly by not considering the real phenomena in the reboiler or in the stripper column. Additionally, the condenser section is not modelled at all. The separated CO_2 gas flow is considered pure at the top of the stripper column, instead of it being mixed with water vapor like in a real process. The temperature of the solvent flow before it enters the solvent sump at the bottom of the column (reboiler) is roughly estimated from the heat load that is fed to the stripping process, and the corresponding CO_2 loading value and therefore the amount of stripped CO_2 are also determined from this temperature value. This can be done because if the stripping process is considered to happen at a constant pressure, then there can only exist a singular reboiler operation temperature and CO_2 loading value pair for a specific solvent. The lower the wanted lean solvent CO_2 loading value at the end of the stripping process is, the higher the reboiler operation temperature then needs to be. (Oexmann, et al., 2012)

In a real stripping process, the heat load that is fed to the reboiler is consumed by four different phenomena when not counting heat losses. These phenomena include desorption of CO_2, heating of the solvent flow, heating of the water condensate flow, and generation of the stripping steam. In one of the post-combustion CO_2 capture system operation experiments conducted by Notz, et al., they determined that 17.3 % of the total energy consumed by the stripping process (when discounting heat losses) went into heating of the solvent. The total energy requirement of the stripping process in this same test was 3.98 GJ/ton of CO_2. This referenced test was done with a 30.3 wt-% MEA solvent, that had a rich CO_2 loading value of 2.296 $mol_{CO2}/kg_{solvent}$, and a temperature of 108.56 °C, at the stripper inlet. (Notz, et al., 2012)

In this work, the percentage value (17.3 %) presented in the previous paragraph, was used to estimate the amount of heat that would warm the solvent flow during the stripping process, leading to the following equation:

$$\dot{Q}_{heating}(t) = 0.173 \cdot \dot{Q}_{reb}(t), \quad (40)$$

where $\dot{Q}_{reb}$ is the total heat load that is being fed to the stripping process in the reboiler. In reality, the shares of total load consumed by the different phenomena do change in different process conditions (Notz, et al., 2012), but in this thesis equation 40, where these shares can be thought of as constants, was used to simplify the modelling task.

The temperature $T_{sump_{in}}$ of the solvent flow when it reaches the sump inlet (surface) in the reboiler was modelled based on the previously defined $\dot{Q}_{heating}$ term (equation 40), as follows:

$$T_{sump_{in}}(t) = \frac{\dot{Q}_{heating}(t)}{\dot{m}_{sol_{in}}(t) c_{sol_{in}}(t)} + T_{str_{in}}(t), \quad (41)$$

where $T_{str_{in}}$ is the temperature of the solvent at the stripper inlet, $\dot{m}_{sol_{in}}$ the mass flow of the solvent at the start of stripping, and $c_{sol_{in}}$ the solvent's specific heat capacity at the start of stripping. The CO_2 flow in the model was also assumed to exit the top of the stripper in this temperature $T_{sump_{in}}$.

As explained before, specific reboiler operation temperature values correspond to specific CO_2 loading values, so the CO_2 loading value at the sump inlet needed to be defined from the $T_{sump_{in}}$ value. For this, the following fitted equation was used in the model:

$$X(t) = -0.00164153 \cdot \left(T(t)\right)^3 + 0.528119 \cdot \left(T(t)\right)^2 - 56.6802 \cdot T(t) + 2031.23. \quad (42)$$

This equation was created by estimating reboiler operation temperatures from multiple loading curves of 30 wt-% MEA solvent at 1.5 bar stripping pressure presented in the work by (Oexmann, et al., 2012), which were then fitted to a third order polynomial equation. This means that the previous equation can only be used to estimate final CO_2 loading values of a stripping process at a constant pressure of 1.5 bar, and with 30 wt-% MEA solvent solution being used in the capture system. The CO_2 loading values given by the previous equation are in $mol_{CO2}/kg_{solvent}$, and the temperature values should be fed to the equation in Celsius units. The results given by the used CO_2 loading equation are plotted below in Figure 16.

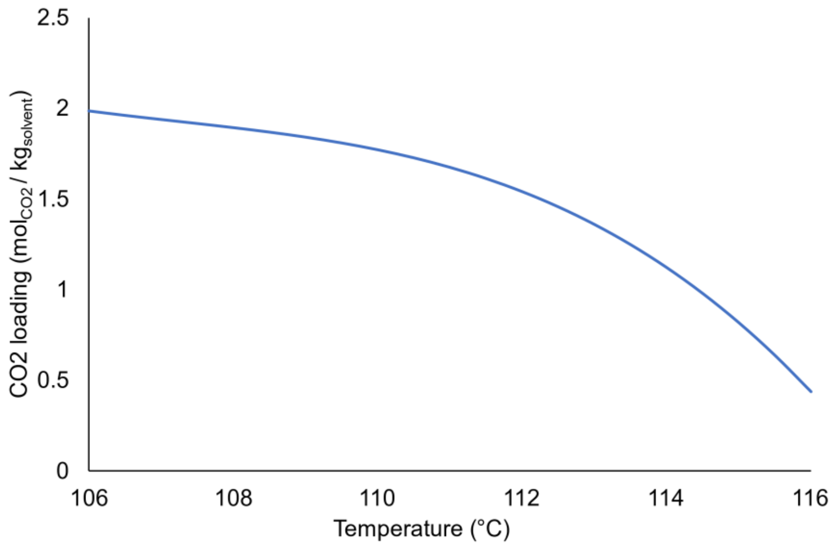

Figure 16. *CO_2 loading values of 30 wt-% MEA solvent based on reboiler temperature, for a stripping process at 1.5 bar.*

Based on the results plotted in Figure 16, the fit gives reasonable looking results in reboiler operation temperature range of 106-116 °C, but probably cannot be used outside this range with acceptable accuracy.

The amount of stripped CO_2 $\dot{n}_{CO_{2desd}}$ was modelled based on the CO_2 loading change during the stripping process with the following equation:

$$\dot{n}_{CO_{2desd}}(t) = \dot{m}_{unl}(t)\left(X_{str_{in}}(t) - X_{sump_{in}}(t)\right), \tag{43}$$

where $X_{str_{in}}$ is the CO_2 loading at the stripper inlet at the start of the stripping process, $X_{sump_{in}}$ the CO_2 loading at the end of the stripping process (defined with equation 42), and $\dot{m}_{unl}$ the mass flow rate of unloaded solvent through the stripper column.

After the stripping process has happened, as the solvent has flown down the column, it reaches the solvent sump inlet (surface) in the reboiler, and instantly mixes into the solvent sump because of the ideal mixing tank assumption. The CO_2 loading change was again modelled with equation 34. Unlike in the developed absorber model, the temperature profile inside the stripping process was not modelled as uniform, because the $T_{sump_{in}}$ value presented before was used in determining the desorption rate of CO_2 in the process. The temperature change in the solvent sump at the bottom of the reboiler was therefore solved from just the sump's individual energy balance, where possible heat losses to the environment were again ignored:

$$\frac{dT_{sump}(t)}{dt} = \frac{\dot{m}_{sol_{in}}(t)c_{sol_{in}}(t)\left(T_{sump_{in}}(t) - T_{sump}(t)\right)}{m_{sol_{sump}}(t)c_{sol_{sump}}(t)}, \tag{44}$$

where $\dot{m}_{sol_{in}}$ is the solvent mass flow into the sump, $c_{sol_{in}}$ the specific heat capacity of this solvent flow, $T_{sump_{in}}$ the temperature of this solvent flow at the sump inlet, T_{sump} the current sump temperature, $m_{sol_{sump}}$ the mass of the solvent currently in the sump, and $c_{sol_{sump}}$ the specific heat capacity of the solvent currently in the sump.

From the solvent sump at the bottom of the reboiler, the solvent flows to the recovery heat exchanger, where it cools down. The modelling of this recovery heat exchanger, and the calculation of the hot side's outlet temperature (equation 39) was already explained earlier in this subchapter. After the recovery heat exchanger, the solvent flows to the precooler located before the absorber column. The temperature after the precooler was modelled by simply determining it from the fed precooling load $\dot{Q}_{cooling}$, and the solvent mass flow through the precooler as follows:

$$T_{out}(t) = \frac{\dot{Q}_{cooling}(t)}{\dot{m}_{sol_{in}}(t)c_{sol_{in}}(t)} + T_{in}(t), \tag{45}$$

where T_{in} is the temperature of the solvent before the precooler, $\dot{m}_{sol_{in}}$ the solvent mass flow in, and $c_{sol_{in}}$ the specific heat capacity of the solvent flow.

A pump model was needed to generate the volumetric flow rate of the solvent through the modelled system. Because of earlier assumptions made during the model development, the volumetric flow rate of the solvent became directly proportional to the mass flow rate of unloaded solvent in this work. The volumetric flow rate could therefore be directly replaced in the developed pump model with the unloaded solvent's mass flow rate value instead. Calculating realistic power consumption of the pump or pumps was not considered necessary, and to avoid going through theory related to pumps, it was assumed that the pump power would linearly affect the generated flow rate. Based on these earlier reasons, the mass flow rate of unloaded solvent generated by the pump was modelled by simply multiplying the maximum generable mass flow rate with the current power setting value $P-\%$ divided by one hundred, because the setting value was defined as a percentage value (%):

$$\dot{m}_{unl}(t) = \dot{m}_{unl_{max}} \frac{P-\%(t)}{100}. \tag{46}$$

Because this flow rate was assumed to be equal everywhere in the modelled capture system only one pump was modelled, instead of separately modelling the two pumps, which were included in the developed plant concept, which was presented earlier in the work in Figure 11.

The full carbon capture simulation model structure is visualized below in Figure 17, which also shows the model input variables. The model has five input variables, which are the pump power setting, regeneration heat load, precooling heat load, flue gas flow rate, and flue gas temperature. Additionally, the temperature and CO_2 loading values of both the solvent sumps must be initialized before simulation runs.

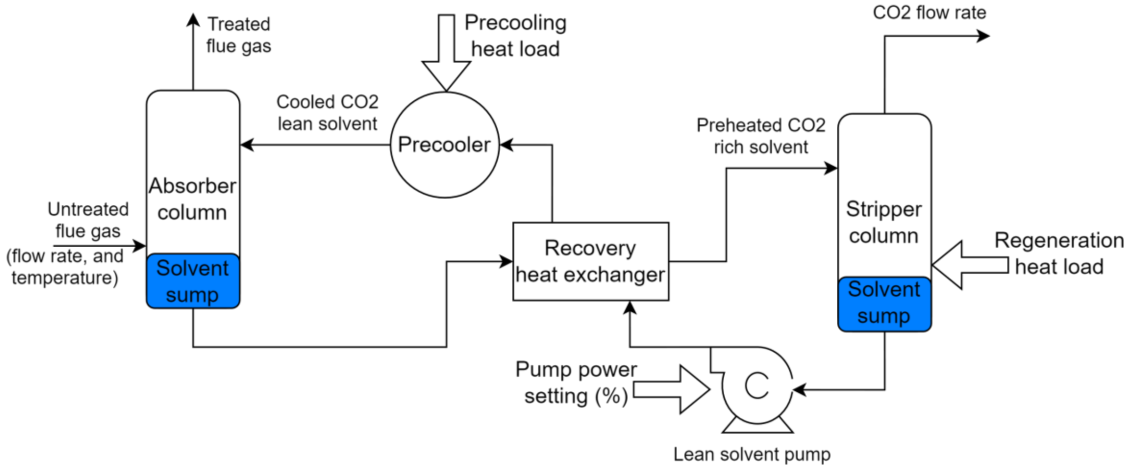

Figure 17. *Visualization of the post-combustion carbon capture model structure.*

The simplifications and assumptions used in the creation of the post-combustion carbon capture simulation model are summarized below:

1. Pressure levels in the capture system were not modelled.
2. CO_2 loading and temperature were assumed to have no effect on the solvent volume.
3. The volume flow rate of the solvent was modelled to be equal in all parts of the carbon capture system.
4. The solvent sumps were modelled as ideal mixing liquid tanks.
5. Heat losses to the environment were not modelled.
6. In all temperature calculations, constant specific heat capacity values were used for all elements in the substances circulating in the capture system.
7. A constant reaction heat value was used for CO_2 absorption in the absorber modelling.
8. The temperature profile of the absorption process was modelled as uniform, but the temperature profile of the stripping process was modelled with two temperature values.
9. The condenser above the stripper column and the condensate reflux returned to the stripper were not modelled. The gas flow from the top of the stripper was modelled as pure CO_2 flow.
10. The stripped CO_2 flow was estimated based on the temperature value at the end of the stripping process.
11. The volume flow rate generated by the solvent pump was estimated to be directly proportional to the pump's power setting.

4.5 Green Methanol Synthesis Modelling

In a work by Luyben where control solutions for a traditional syngas-based methanol synthesis plant were covered, an additional second preheating stage was included so that the inlet temperature of the reactor could be controlled. The first preheating stage in the considered traditional plant was uncontrolled, as its aim was to recover as much heat as possible from the product stream coming from the reactor. (Luyben, 2010) These two preheating stages were also chosen for the methanol plant configuration developed in this thesis work. However, in the developed model structure, these stages were combined into a one single preheating stage. The reasoning for this is explained in the next paragraph.

It was not necessary to model the temperature of the product recycle stream after the heat recovery preheater, and before product separation, because the separation process was not included in the scope of this thesis. For this reason, the preheating stages, and their heating load $\dot{Q}_{heating}$ could be combined in the developed model to simplify the modelling task. The previously given reasoning is attempted to be visualized in Figure 18, where the process parts outside the thesis scope are crossed over, and how their omission affects different process values in the modelled system explained. Effected process value locations are connected to the explanations with arrows in Figure 18, and the preheating stages that were combined in the model structure, are also circled with a dashed line.

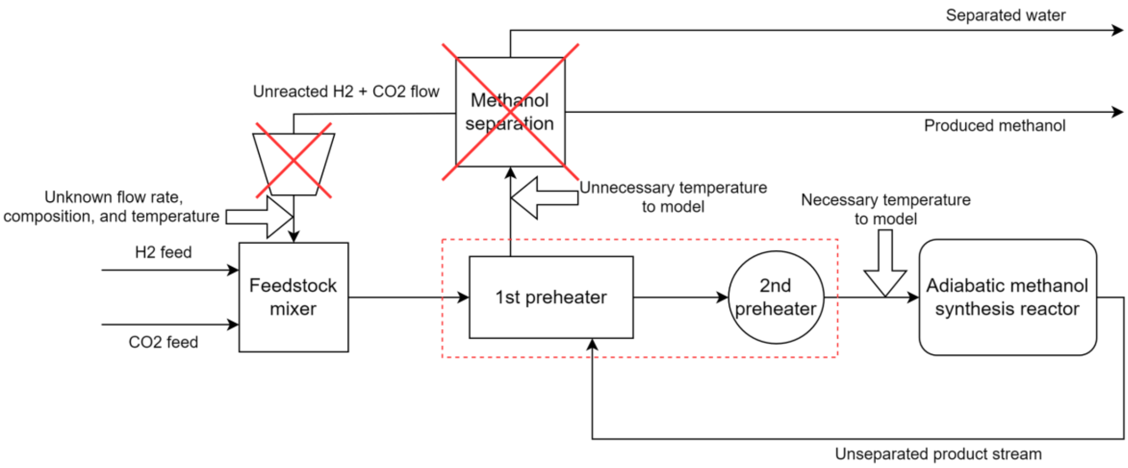

Figure 18. *Visualization of the reasoning behind the combined preheating modelling, with process parts outside this work's scope crossed out.*

Because the product separation process was not modelled, the recycle flows of unreacted hydrogen and CO_2 were also decided to be left out of the developed synthesis model. Therefore, only the flows fed from upstream subprocesses are combined in the modelled feedstock mixer. The temperature after the feedstock mixer is determined in the model from the energy balance of the feedstock gases, as follows:

$$T_{out}(t) = \frac{\dot{n}_{H_2}(t) c_{m_{H_2}} T_{H_{2_{in}}}(t) + \dot{n}_{CO_2}(t) c_{m_{CO_2}} T_{CO_{2_{in}}}(t)}{\dot{n}_{H_2}(t) c_{m_{H_2}} + \dot{n}_{CO_2}(t) c_{m_{CO_2}}}, \tag{47}$$

where $T_{H_{2_{in}}}$ is the temperature of hydrogen feed flow before the mixer, $T_{CO_{2_{in}}}$ is the temperature of CO_2 feed flow before the mixer, $\dot{n}$ values are the molar flows of these feed substances and c_m values are their molar heat capacities.

After the mixer, the mixed feed flow is preheated. The temperature of the feed gas after the preheating was again in the simulation model determined from the process' energy balance, in which the combined $\dot{Q}_{heating}$ value was used to include both preheating states in the same model, as explained before:

$$T_{out}(t) = \frac{\dot{Q}_{heating}(t)}{\dot{n}_{H_2}(t)c_{m_{H_2}} + \dot{n}_{CO_2}(t)c_{m_{CO_2}}} + T_{in}(t), \quad (48)$$

where T_{in} is the temperature of the feed flow after the feedstock mixer, and $\dot{n}$ values are the molar flows of feed substances (CO_2 and H_2), while c_m values are their molar heat capacities.

The modelled single-pass adiabatic methanol reactor was assumed to be a plug flow reactor, which was modelled ideally, meaning that there was assumed to be no mixing of gases or back flow. In the model, the inlet and outlet mass flows of the reactor were assumed as equal, meaning that there could be no mass accumulation into the reactor. The pressure in the reactor inlet was assumed to be constant at 50 bar, and the catalyst material and its possible effects were also ignored. The feed temperature and feed composition, which depends on the flow rates of hydrogen and CO_2, were left as variables that could affect the reactor behavior in the model. A methanol yield (defined earlier in equation 23) equation that depends on these inlet variables was therefore created. In this equation, the feed's composition was included as a single variable by utilizing the stoichiometric number S (defined earlier in equation 19). This yield equation was created based on conversion results that were presented in an earlier modelling work that also modelled single-pass adiabatic methanol reactors. (Cui & Kær, 2020) The developed yield equation is presented below:

$$y_{MeOH}(t) = -0.1 \cdot T_{in}\big(t - t_{res}(t)\big) + 2.4660 \cdot S_{in}\big(t - t_{res}(t)\big) + 31.9626, \quad (49)$$

where the feed's reactor inlet temperature T_{in} must be given in Celsius units, and where the resulting yield value y_{MeOH} is in percentages. Additionally, the fitted equation can only be used for feed compositions that do not include CO. The results given by equation 49 for different feed composition and inlet temperature values are visualized in Figure 19 below. This yield modelling was also only designed to work on operation ranges of T_{in}: 180-280 °C, and S_{in}: 2-10.

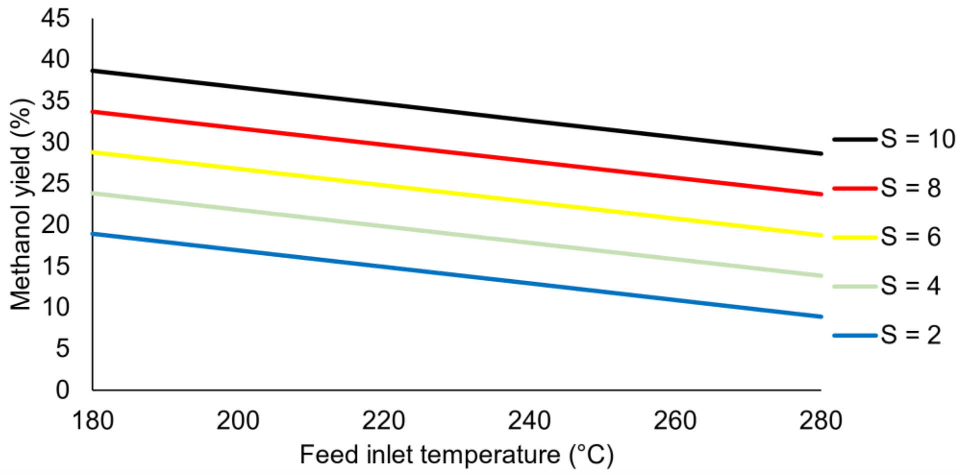

Figure 19. *Methanol yield results based on the reactor inlet feed temperature, for compositions S: 2-10, at constant inlet pressure of 50 bar, and with only CO_2 and H_2 in the reactor feed.*

The equilibrium concentrations of the product stream that correspond to specific inlet conditions are in the model calculated from the previously presented equation 49 and the methanol conversion reaction, which was presented in equation 21. Similarly, the reaction equilibrium temperature T_{prod} that corresponds to specific inlet conditions was assumed to always be reached in the model. It can be solved from the heat generated by the reaction, and in the developed process model this led to the following equation being used:

$$T_{prod}(t) = \frac{\dot{m}_{in}(t-t_{res}(t))c_{prod}(t)T_{in}(t-t_{res}(t))+\dot{n}_{CO_2in}(t-t_{res}(t))\frac{y_{MeOH}(t)}{100}\Delta H}{\dot{m}_{in}(t-t_{res}(t))c_{prod}(t)}, \tag{50}$$

where $\dot{m}_{in}$ is the feed mass flow into the reactor, c_{prod} the specific heat capacity of the product stream, T_{in} the temperature of the feed before the reaction, $\dot{n}_{CO_2in}$ the amount of CO_2 in the feed as a molar flow rate, y_{MeOH} the methanol yield specified by the inlet conditions, and ΔH the reaction heat of CO_2 hydrogenation. The reactor outlet temperature was modelled to see if the chosen adiabatic uncooled reactor type could be kept below the allowed operation temperature limit, which based on an earlier source was 280 °C (Cui & Kær, 2020).

The previously appearing reactor residence time t_{res} was used in the reactor model as a delay for the reaction equilibrium concentration and temperature values, to take the reactor dynamics into account. In the developed model this time variable delay was implemented with MATLAB Simulink's "*Variable Transport Delay*" -block. The residence time input was defined for this block based on the feed mass flow through the reactor $\dot{m}_{in}$, and the gas mass m_{gas} already inside the reactor as follows:

$$t_{res}(t) = \frac{m_{gas}}{\dot{m}_{in}(t)}. \tag{51}$$

The molar flows of individual substances at the reactor outlet were modelled by multiplying the known outlet product stream concentrations with the current mass flow rate through the reactor:

$$\dot{n}_x(t) = b_x(t)\dot{m}_{in}(t), \tag{52}$$

where $\dot{n}_x$ is the molar flow rate of any substance in the product stream, b_x its molality, and $\dot{m}_{in}$ the total mass flow rate through the reactor.

The developed model structure of the methanol synthesis subprocess is visualized below in Figure 20. The model has five input variables in total, which are the molar flow rates of CO_2 and hydrogen into the feedstock mixer, their temperatures before the mixer, and the preheating load. These input variables are again included in the presented model visualization.

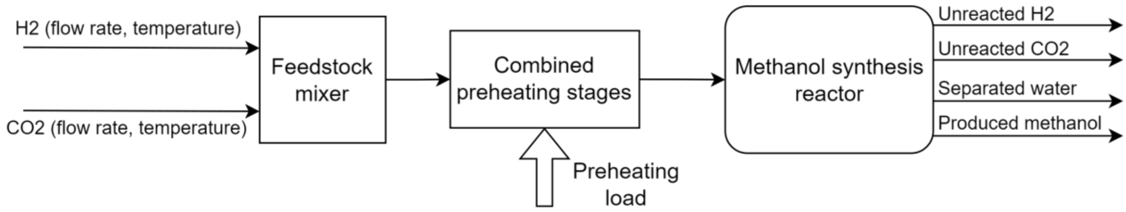

Figure 20. *Visualization of the methanol synthesis model structure.*

The simplifications and assumptions used in the creation of the methanol synthesis process simulation model are summarized below:

1. Mass was assumed to not accumulate into the synthesis reactor, because its inlet and outlet mass flows were modelled as equal.
2. The synthesis reactor's inlet was modelled at a constant pressure of 50 bar.
3. The synthesis reactor was modelled as an ideal plug flow reactor.
4. The synthesis was assumed to have 100 % selectivity towards the wanted methanol conversion reaction (equation 21), so unwanted byproduct (CO) formation was not modelled.
5. Constant specific heat capacity values were used for individual elements in all temperature calculations.
6. The preheating stages of the synthesis feed were combined into a single stage in the model.
7. Heat losses to the environment were not modelled.

8. Neither the product separation process nor the recycle feedstock streams were modelled.

4.6 Storage Systems Modelling

Both storage systems of hydrogen and CO_2 include intercooled compressor trains, which are used for gas compression. In this work, accurately modelling the power consumption of the compression processes was not considered to be of major importance, so the compression trains in both storage models were modelled with just one compression stage. The task of the compressors in the models is just to generate mass flows in the system. For this reason, the compressor calculations were also simplified by treating both hydrogen and CO_2 as ideal gases during compression. The gas flow generated by a one compressor $\dot{n}_{comp}$ was modelled in both storage systems with the following equation:

$$\dot{n}_{comp}(t) = \frac{\eta_{comp} P_{comp}(t)}{RT_{in}(t)\frac{n}{n-1}\left(\left(\frac{p_{out}(t)}{p_{in}(t)}\right)^{\frac{n-1}{n}} - 1\right)}, \tag{53}$$

where η_{comp} is the compressor efficiency as a unitless factor between 0 and 1, P_{comp} the power consumed by the compressor, R the ideal gas constant, T_{in} the temperature at the compressor inlet, p_{in} the pressure at the compressor inlet, p_{out} the pressure after compression, and finally n the polytropic exponent. This equation was derived from the polytropic compressor work equation presented earlier in the literature review part (equation 17), when the compressed gas was assumed as ideal, and the use of compressibility factor therefore ignored.

Intercooling of the compressor trains was considered by using suitable constant polytropic exponent n values, which reduce the power required by the compressors compared to adiabatic compression processes. However, in both storage models, the final temperatures of compression were not modelled accurately based on the used polytropic exponent values, and instead constant temperature values were used. This was done to simplify the pressure calculations in the storage system models. One more complex option would have been to model the polytropic exponent values as input values that would represent the intercooling load of the compressor trains and that could be controlled to achieve the wanted final temperatures.

4.6.1 Compressed Hydrogen Storage System Modelling

The pressure change inside the hydrogen storage tank could be derived from its mass balance and equation 16 presented earlier, which led to the following equation being used in the modelling:

$$\frac{dp_{H_2tank}(t)}{dt} = \frac{Z_{H_2}(t)\left(\dot{n}_{H_2in}(t) - \dot{n}_{H_2out}(t)\right)RT_{tank}}{V_{tank}}, \tag{54}$$

where Z_{H_2} is the compressibility factor of hydrogen, $\dot{n}_{H_2in}$ the molar flow into the storage, $\dot{n}_{H_2out}$ the molar flow out of the storage, R the ideal gas constant, T_{tank} the temperature of the hydrogen storage system, and V_{tank} the volume of the storage tank. The modelling of cooling and heating phenomena of the hydrogen storage were left out, as a constant T_{tank} value was used like explained earlier.

However, hydrogen was treated as a real gas in the storage tank by including the use of compressibility factor Z. This was done to model the stored capacity more accurately in the system. A fit, which was taken from (Striednig, et al., 2014), was used to model the compressibility factor of hydrogen in this work:

$$Z_{H_2}(t) = 1 + K_1Tp(t) + K_2p(t) + K_3\frac{p(t)}{T} - K_4T^2\left(p(t)\right)^2 - K_5T\left(p(t)\right)^2 - K_6\left(p(t)\right)^2 - K_7\frac{\left(p(t)\right)^2}{T} + K_8\frac{\left(p(t)\right)^2}{T^2}, \tag{55}$$

where temperature and pressure are used in SI-units. The definitions of the appearing coefficient values $K_1 - K_8$, are provided in Appendix C of this work. Because the hydrogen storage temperature was set as a constant in this work, the variation of the compressibility factor is only caused by the change in the tank pressure like can be seen from equation 55.

In the model, the flow into the storage $\dot{n}_{H_2in}$ is defined by the compressor power and flow out of the storage is defined by the discharge valve opening y (between 0-1). The equation used in this work for the molar flow rate of gas $\dot{n}_x$ through a valve was modified from a mass flow rate equation used for CO_2 gas in another dynamic modelling study (Olumayegun & Wang, 2019). The equation used in the model is presented below:

$$\dot{n}_x(t) = C_v y(t)\sqrt{p_{in}(t)\rho_{in}(t)\left(1 - \frac{p_{out}}{p_{in}(t)}\right)}, \tag{56}$$

where p_{in} is the pressure upstream of the valve, p_{out} the pressure downstream of the valve, ρ_{in} the density of the gas at the valve inlet, and C_v a valve construction and gas specific coefficient. The required density value of the gas at the valve inlet was determined from the gas law (equation 16) in the model. The temperature of the hydrogen synthesis flow was defined as a molar flow rate weighted average from the temperatures of hydrogen that is taken straight from the electrolysis, and hydrogen that is taken from the hydrogen gas tank.

The developed model structure of the hydrogen storage system is visualized below in Figure 21. The model has six input variables, which include the molar flow rate of hydrogen into the system produced with electrolysis, the electrolysis pressure, the electrolysis temperature, the compressor power, the storage discharge valve opening, and the storage tank temperature. The starting pressure of the hydrogen storage tank must also be initialized before simulation runs.

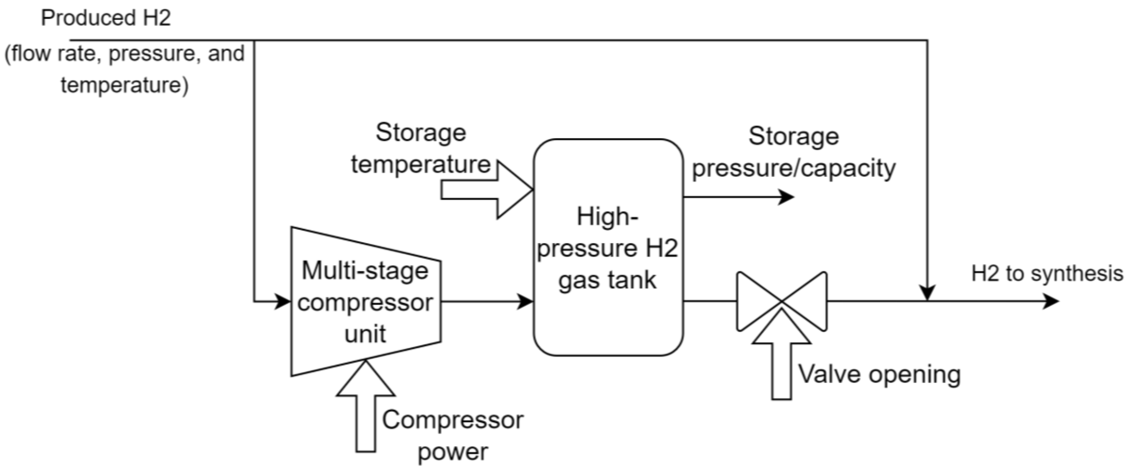

Figure 21. *Visualization of the compressed hydrogen storage system model structure.*

The simplifications and assumptions used in the creation of the hydrogen storage system simulation model are summarized below:

1. In the storage tank model, hydrogen was treated as a real gas to better estimate the stored capacity and pressure level inside the gas tank.
2. In the compressor model, hydrogen was treated as an ideal gas, which causes error between the modelled power consumption and the generated flow rate.
3. Actual intercooling of the compressor train was not modelled, the power consumption of the compressor train is decreased compared to an adiabatic scenario by using a polytropic exponent to estimate the work decrease that would be caused by the intercooling.
4. Gas storage heating or cooling phenomena, which were discussed in the literature review part, were not modelled. The storage system was assumed to stay at constant temperature instead.

5. Since the storage temperature was defined as an input variable, it was modelled independently in relation to the compressor model.
6. Pressure losses in the pipelines were not modelled.

4.6.2 Liquid CO_2 Storage System Modelling

The created CO_2 storage system model and the previously presented hydrogen storage model are largely similar. One difference between the systems is that in the CO_2 storage system, the CO_2 gas passing through the main feedline must also be compressed to achieve the required reactor inlet pressure downstream. In the CO_2 storage system model the compressor inlet pressure changes were also modelled unlike in the hydrogen storage system model, and CO_2 was treated as an ideal gas everywhere in the system. The pressure change at the compressor feedline could therefore be derived from the mass balance of the compressor and the ideal gas law, which led to the following equation:

$$\frac{dp_{comp_{in}}(t)}{dt} = \frac{\left(\dot{n}_{CO_2comp_{in}}(t) - \dot{n}_{CO_2comp_{out}}(t)\right)RT_{comp_{in}}}{V_{fline_{comp}}}, \tag{57}$$

where $\dot{n}_{CO_2comp_{in}}$ is the flow rate of CO_2 gas in the compressor feedline, $\dot{n}_{CO_2comp_{out}}$ the CO_2 flow rate generated by the compressor train, $T_{comp_{in}}$ the temperature at compressor inlet, which was assumed constant in the model, and $V_{fline_{comp}}$ the volume of the feedline before the compressor. The flow rate generated by the compressor $\dot{n}_{CO_2comp_{out}}$ was again modelled with equation 53, which was presented earlier in the text.

The back pressure of the compressor, which is also the storage system pressure, was modelled similarly as the compressor inlet pressure was, with the following equation:

$$\frac{dp_{valve_{in}}(t)}{dt} = \frac{\left(\dot{n}_{CO_2valve_{in}}(t) - \dot{n}_{CO_2valve_{out}}(t)\right)RT_{valve_{in}}}{V_{fline_{valve}}}, \tag{58}$$

where $\dot{n}_{CO_2valve_{in}}$ is the flow rate of CO_2 gas to the synthesis valve, $\dot{n}_{CO_2valve_{out}}$ the CO_2 flow rate through the synthesis valve, $T_{valve_{in}}$ the temperature of the storage system and at the valve inlet, again assumed constant in the model, and $V_{fline_{valve}}$ the volume of the storage system gas piping. The flow through the synthesis valve $\dot{n}_{CO_2valve_{out}}$ was again determined with equation 56 that was previously used in the hydrogen storage system modelling. The flow rate to the valve $\dot{n}_{CO_2valve_{in}}$ was solved from the mass balance of the whole storage system, as follows:

$$\dot{n}_{CO_2valve_{in}}(t) = \dot{n}_{CO_2comp_{out}}(t) - \dot{n}_{CO_2tank_{in}}(t) + \dot{n}_{CO_2tank_{out}}(t), \tag{59}$$

where $\dot{n}_{CO_2comp_{out}}$ is the CO_2 gas flow generated by the compressor train, $\dot{n}_{CO_2tank_{in}}$ the flow rate that is fed to the CO_2 storage, and $\dot{n}_{CO_2tank_{out}}$ the flow rate that is taken from the storage tank. The liquefaction and evaporation processes that would determine the flows to the storage were decided to be left out from the modelling scope, and the storage flows were instead modelled as user determinable inputs. Because CO_2 is stored as liquid in the storage tank, the variation in storage capacity was assumed to not change the pressure inside the tank or in the system, unlike in the case of the modelled hydrogen storage that was a compressed gas tank. The change in the storage capacity was modelled simply based on the storage's mass balance, as follows:

$$\frac{dn_{CO_2tank}(t)}{dt} = \dot{n}_{CO_2tank_{in}}(t) - \dot{n}_{CO_2tank_{out}}(t). \tag{60}$$

The developed model structure of the CO_2 storage system is visualized below in Figure 22. The model has eight input variables, which include the flow rates in and out of the liquid CO_2 storage like mentioned earlier, the storage system temperature, the compressor power, the synthesis valve opening, the synthesis pressure, and the temperature and flow rate of CO_2 coming from the carbon capture system. In addition to the input variables, the pressure values of both the storage system and the compressor inlet, and the amount of CO_2 in the storage must be initialized before simulations.

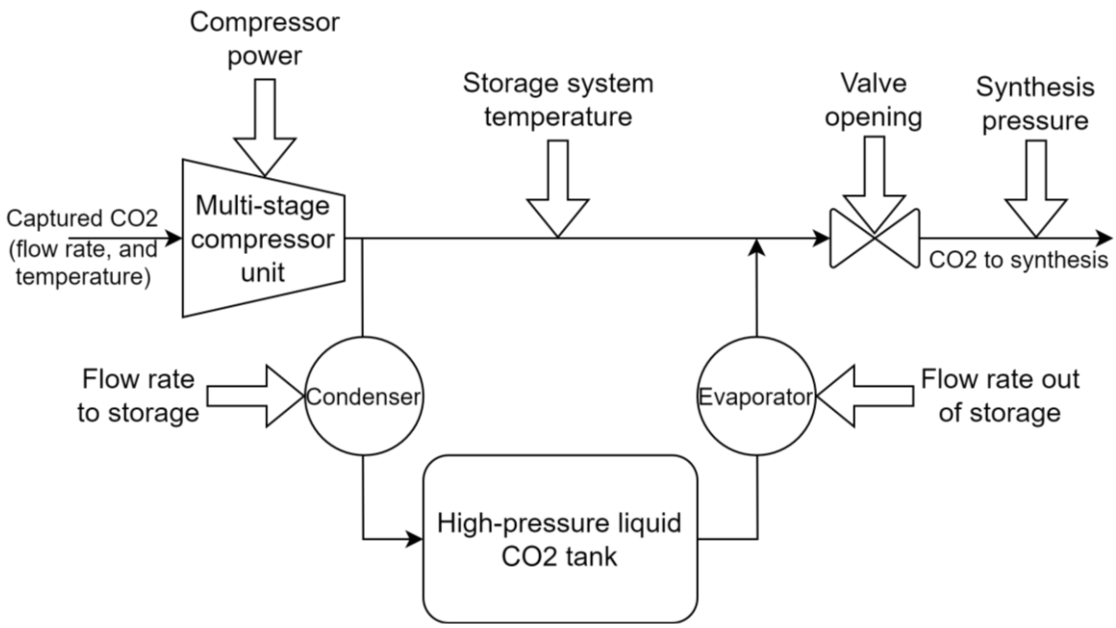

Figure 22. *Visualization of the liquid CO_2 storage system model structure.*

The simplifications and assumptions used in the creation of the CO_2 storage system simulation model are summarized below:

1. CO_2 was treated as an ideal gas both in the compressor model and in the pipeline pressure calculations.

2. Actual intercooling of the compressor train was not modelled, the power consumption of the compressor train is decreased compared to an adiabatic scenario by using a polytropic exponent to estimate the work decrease that would be caused by the intercooling.
3. Since the storage system temperature was defined as an input variable, it was modelled independently in relation to the compressor model.
4. The condenser and evaporator were not modelled mathematically. Flows in and out of the storage tank were instead modelled as user modifiable input variables.
5. Pressure losses in the pipelines were not modelled.

5. RESULTS AND DISCUSSION

In this chapter, the results of the work are presented and analyzed. These results include simulation results of the developed individual subprocess models in selected test runs, as well as proposed control solutions for the subprocesses of the considered Power-to-Methanol plant concept. The test simulation runs are discussed first because they were needed as intermediate results, based on which possible control solutions could then be proposed.

5.1 Dynamic Behavior Analysis

The dynamic behavior of the developed subprocess simulation models was tested by doing open loop step response simulation runs with input variables, whose effects were deemed to be important from a control perspective. The behavior of the models is analyzed both to validate that they work as expected and to analyze control variable candidates of the subprocesses. To make following the plotted simulation results easier, readers are advised to go back and look at the model structure visualizations again if it is not clear what the simulated values were and where were they located in the modelled systems.

When keeping in mind the eventual goal of designing controls based on the simulation results that are analyzed next, it is important to look at the results from two perspectives. Firstly, the results should be looked at to detect any unstable process variables in order to design stabilizing controls needed to keep the processes within allowed operation ranges. Secondly, the results should be analyzed to identify possible quality control variables or those variables that could be manipulated to influence most effectively any of the already known quality control variables, such as production rates or loads.

5.1.1 Proton Exchange Membrane Electrolysis

In this subchapter, the open loop behavior of the developed PEM electrolyzer model is analyzed. The parameter values used for the PEM electrolyzer modelling can be found from Appendix A of this work. Initial input values of the analyzed simulations, which were initialized to produce a steady operation state, are presented below in Figure 23.

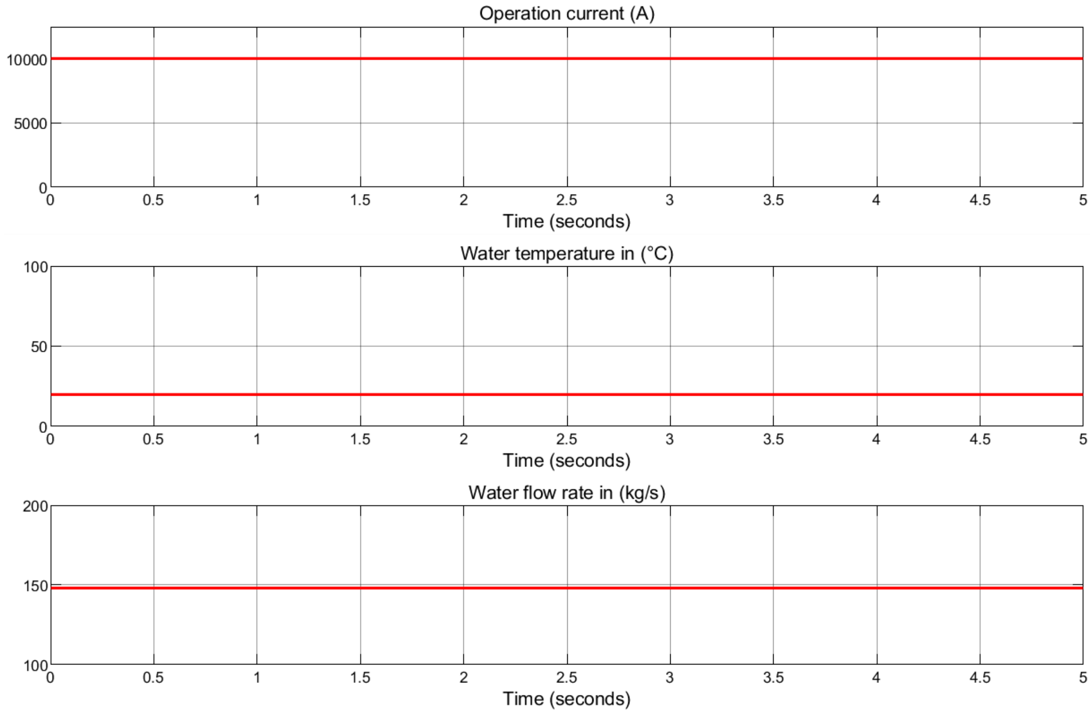

Figure 23. *PEM electrolyzer modelling -initial input values.*

Next, the modelling results of a step change of the electrolyzer operation current are analyzed. Because the initial operation values that were presented are close to the upper operation load limit of the modelled electrolyzer, this test was done by dropping the operation current from 10 000 A to 6 000 A, at t=5 s. Other input values were kept as their initial values. The tested input variable change and outputs of this simulation run are plotted below in Figure 24, as red and blue, respectively.

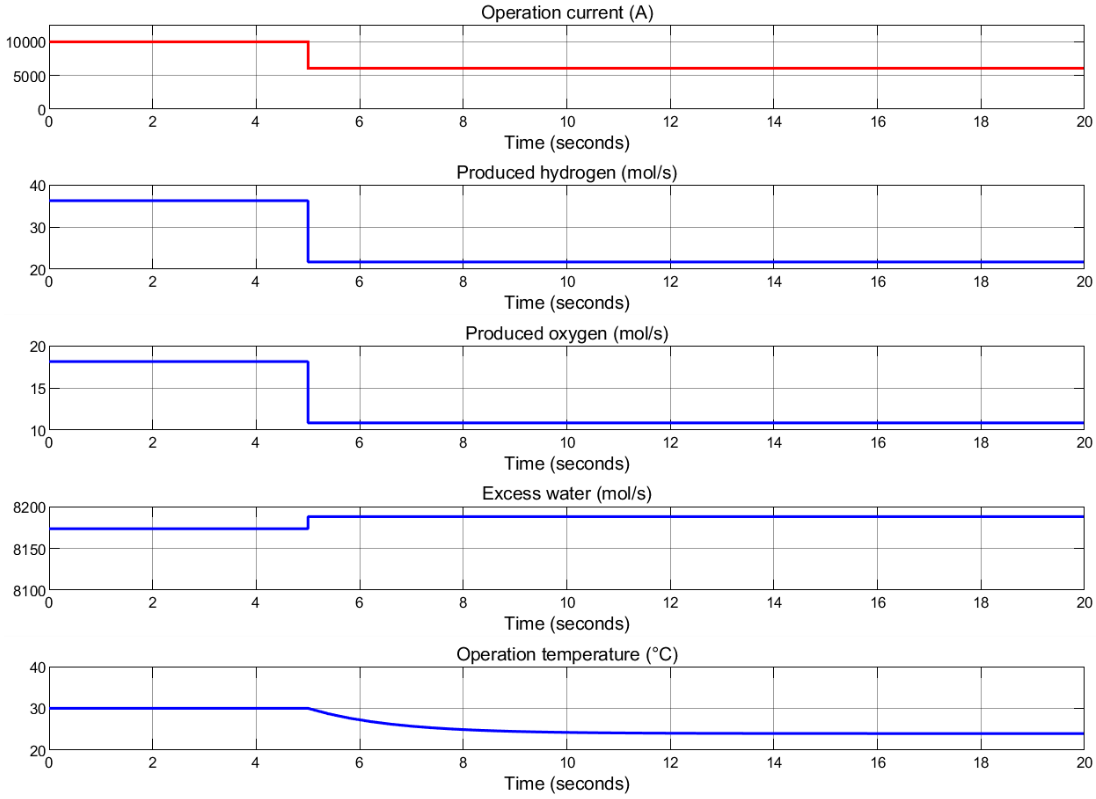

Figure 24. *Operation current -step response simulation results.*

From Figure 24 it can be observed that the amounts of produced gases change instantaneously because realistic dynamics of ion transfer were not modelled. However, in the literature review very quick load changes in a range of couple seconds were suggested to be possible for PEM electrolyzers, so if the plant is considered as a whole, then omitting this dynamic is almost meaningless. Because of the already large amount of excess water flow that is used for cooling purposes, the change in the excess water flow rate is very minor. When the electrolyzer load and production drop, the generated heat also decreases, which leads to a decrease in the operation temperature. In the model, the operation temperature changes until a new steady state is found.

Next, the modelling results of a step change of the water flow rate in are analyzed. In the test run, the flow rate was raised from 147.9 kg/s to 180 kg/s at t=5 s, and other input values were kept as their initial values. The tested input variable change and outputs of this simulation run are plotted below in Figure 25, as red and blue, respectively.

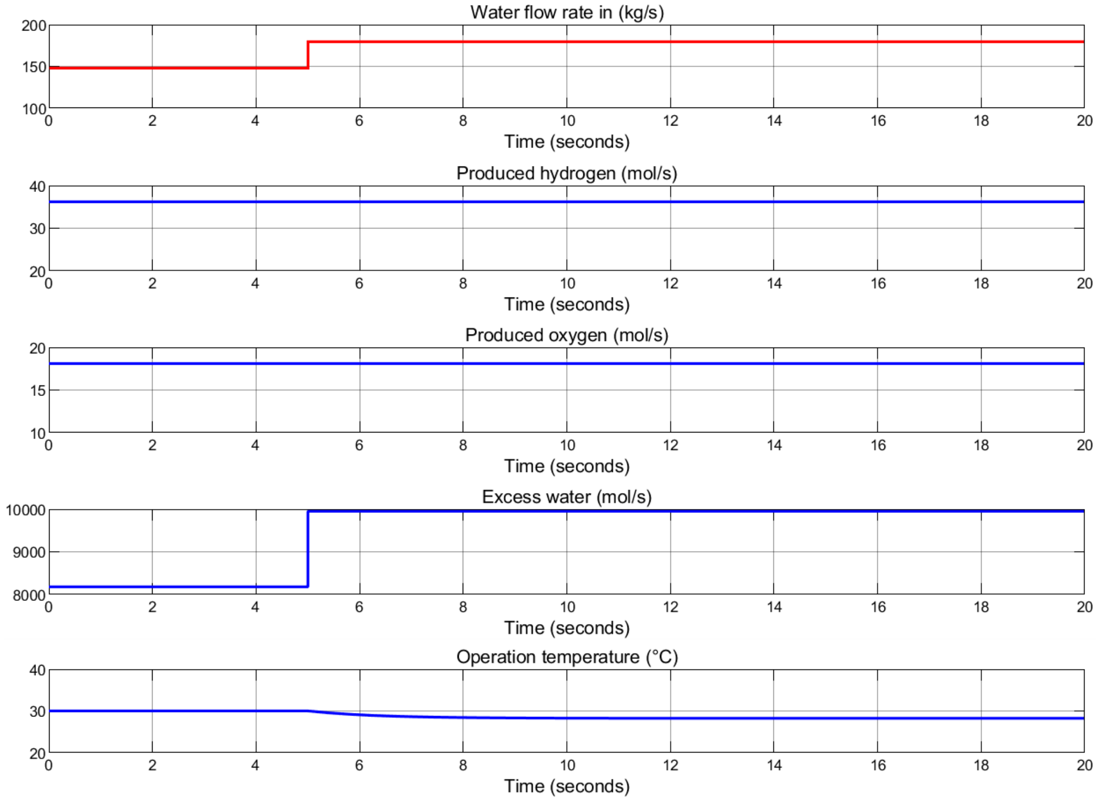

Figure 25. *Water flow rate in -step response simulation results.*

It can be observed that if the water flow rate in is changed in the model, it only affects the operation temperature and the amount of excess water flow rate. The change in water flow does not affect the gas flows because the electrolyzer efficiency was only modelled based on its operation current. If the electrolyzer efficiency had also been modelled in relation to the operation temperature, then the instability of a real system would be seen better from the model. A change in operation temperature would in reality affect the efficiency, and therefore the molar flows of produced gases, and the amount of generated excess heat. This would cause the temperature to keep changing, unlike in the model that was created in this work.

However, it can still be seen from the developed model that the electrolyzer operation current and the amount of water flow determine the steady operation state of the system. The third model input, which was the water flow's inlet temperature was kept constant, and its step response tests were not analyzed, as a lower inlet temperature would obviously just decrease the operation temperature, and a higher inlet temperature would increase it, similarly as the model would react to water flow rate changes.

5.1.2 Compressed Hydrogen Storage System

In this subchapter, the open loop behavior of the developed hydrogen storage system model is analyzed. The modelling parameters of the system can be found from Appendix

B of this work, and the coefficient definitions of the used hydrogen compressibility factor Z_{H_2}-fit can be found separately from Appendix C. The initial values of the analyzed simulation runs are presented below in Figure 26. However, a couple of the input values included in this figure were not considered for possible step response tests and were modelled just as constants. These constant input values were the electrolysis pressure, which is also the pressure at the compressor inlet and at the main hydrogen feedline, and the hydrogen storage tank temperature.

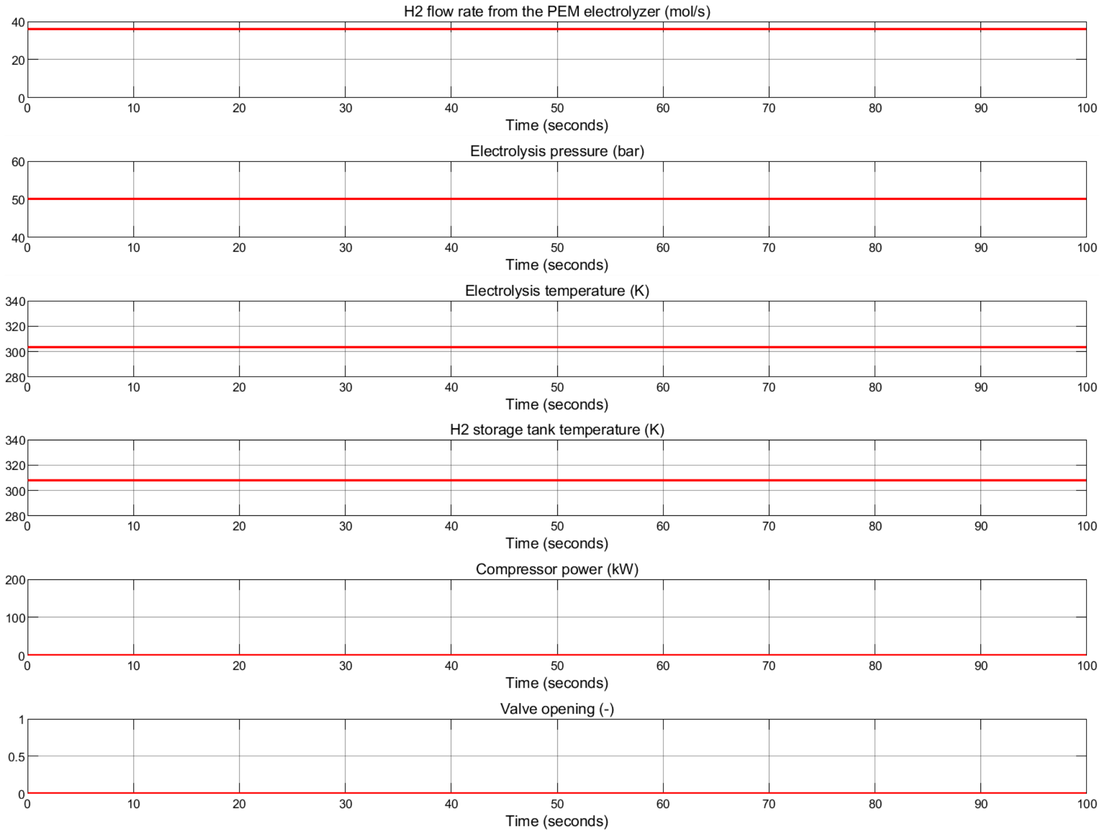

Figure 26. *Compressed hydrogen storage system modelling -initial input values.*

Next, the modelling results of a step change of the compressor power are analyzed. In the test run, the compressor power was raised from 0 kW to 100 kW at t=100 s, and other input values were kept as their initial values. The tested input variable change and outputs of this simulation run are plotted below in Figure 27, as red and blue, respectively.

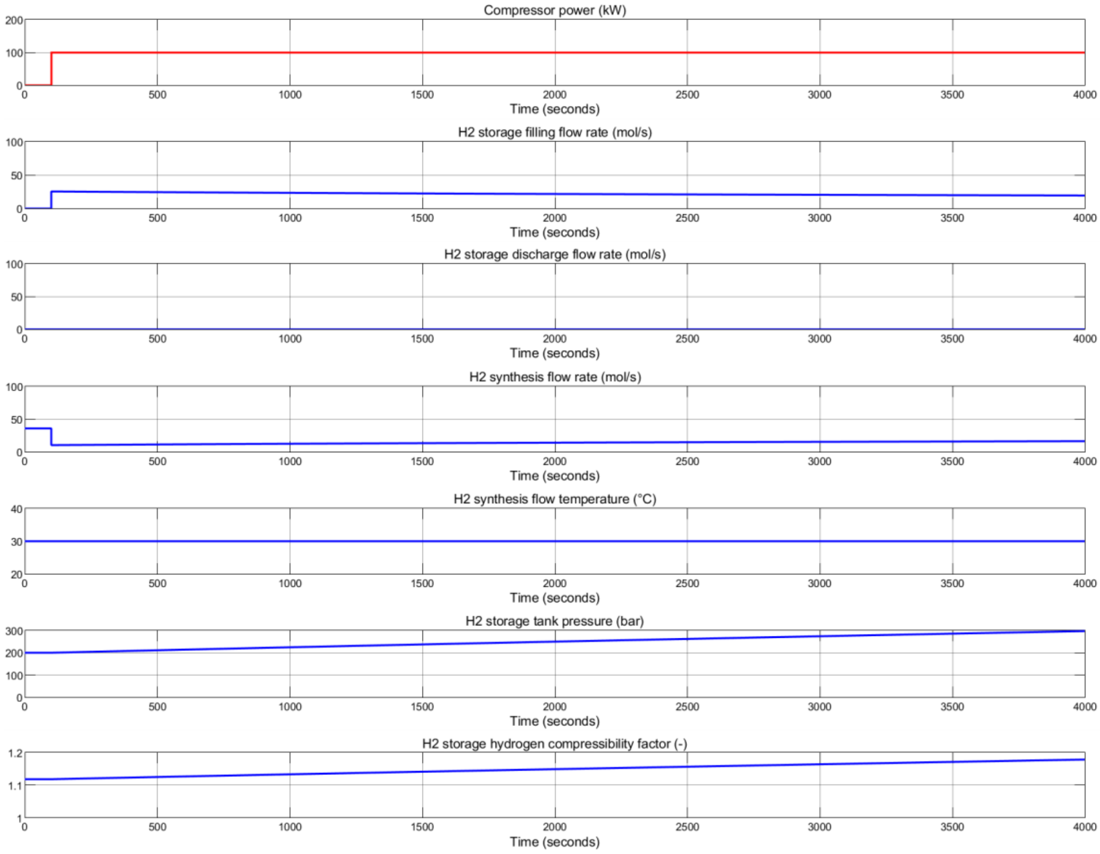

Figure 27. *Compressor power -step response simulation results.*

At t=100 s when the compressor power is increased, it instantaneously starts generating hydrogen flow to the storage tank, which reduces hydrogen's synthesis flow rate. The amount of hydrogen in the tank keeps increasing as there is no discharge flow, which then increases the pressure in the tank, and because the compressor back pressure keeps increasing, the flow rate that it can generate with the fed power continuously decreases during the simulation. The synthesis flow stays at the electrolysis temperature because there is no storage discharge flow, and the synthesis flow is just taken straight from the PEM electrolyzer.

Next, the modelling results of a step change of the storage discharge valve opening are analyzed. In the test run, the valve was opened to a 0.1 position from 0 at t=100 s, and other input values were kept as their initial values. The tested input variable change and outputs of this simulation run are plotted below in Figure 28, as red and blue, respectively.

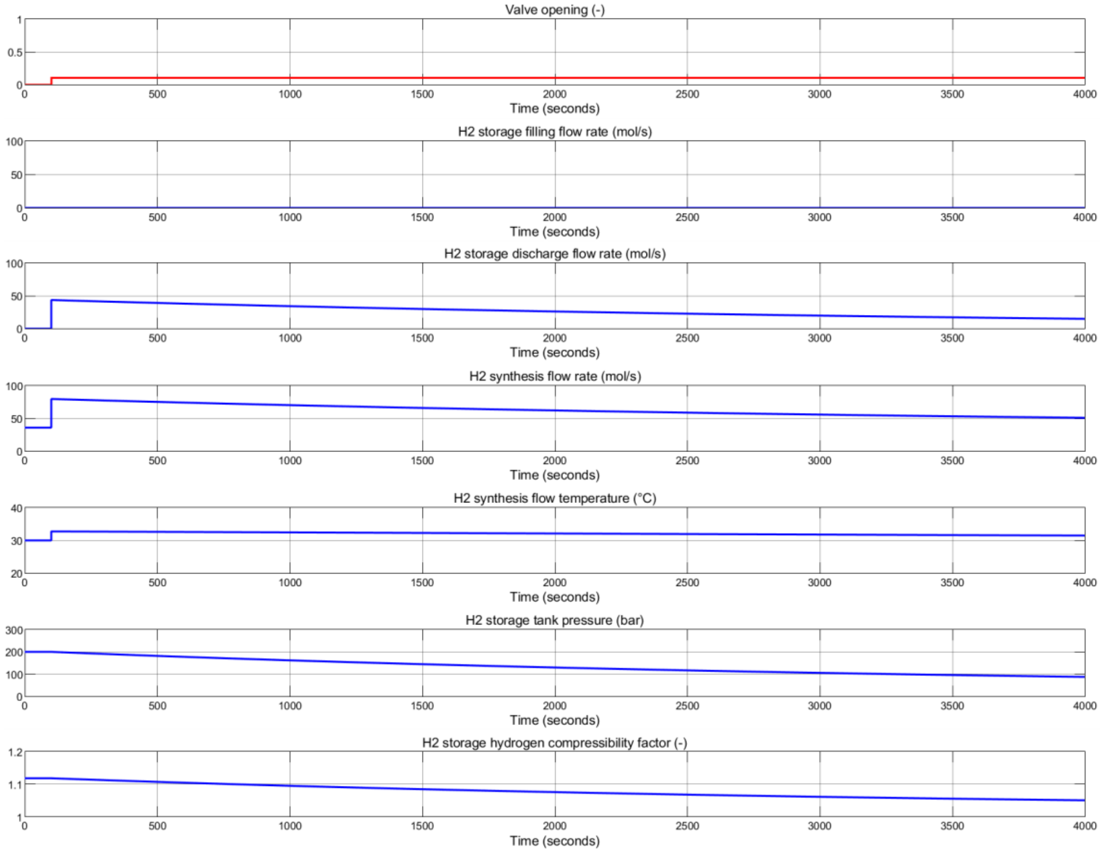

Figure 28. *Valve opening -step response simulation results.*

At t=100 s when the discharge valve is opened, hydrogen starts flowing out of the storage, which increases its synthesis flow rate. The synthesis flow consists of hydrogen flows that are taken straight from the electrolyzer and from the storage, so its temperature depends on the mixing ratio of these two flows. This can also be seen in the plotted synthesis flow temperature results. Because the amount of hydrogen in the storage decreases as long as the storage is discharged, the pressure in the tank keeps decreasing during the whole simulation run. This also affects the flow rate out of the storage, which decreases in relation with the valve inlet pressure.

Step responses to the change of the hydrogen flow rate from the PEM electrolyzer to the system were not tested, as the change should only affect the hydrogen synthesis flow rate from the model outputs. In case there was a discharge flow at the same time, it would also affect the synthesis flow's temperature, but not any other additional outputs. Changing the electrolysis temperature input was also not tested, as at this point it was assumed that the electrolysis temperature could be controlled to be stable in a real system. Electrolysis pressure and storage tank temperature inputs were not even considered to be tested, like mentioned at the start of this chapter.

5.1.3 Post-combustion Carbon Capture System

In this subchapter, the open loop behavior of the developed carbon capture system model is analyzed. Initializing this model to a steady state, from which the simulation runs could be started, was however found to be very challenging. This was assumed to be due to the third order polynomial fit (equation 42) used to determine the CO_2 loading values at the inlet (surface) of the solvent sump at the bottom of the stripper column (reboiler unit). Because of this initialization problem, test simulations of absorption and stripping processes were decided to be done separately, so that the starting operating conditions for these tests could be steadied.

All the other process components except the stripper model, which combined the column and the reboiler, were tested together in the absorption test simulations, and the stripper model's behavior was tested just individually. In the analyzed absorption process tests the stripper's outlet values (solvent temperature at stripper outlet, and lean CO_2 loading) were given as constant input values for the rest of the carbon capture model, which can be seen in the initial absorption process input values that are plotted below in Figure 29. The parameter values used in the CO_2 absorption process modelling are provided in Appendix D of this work.

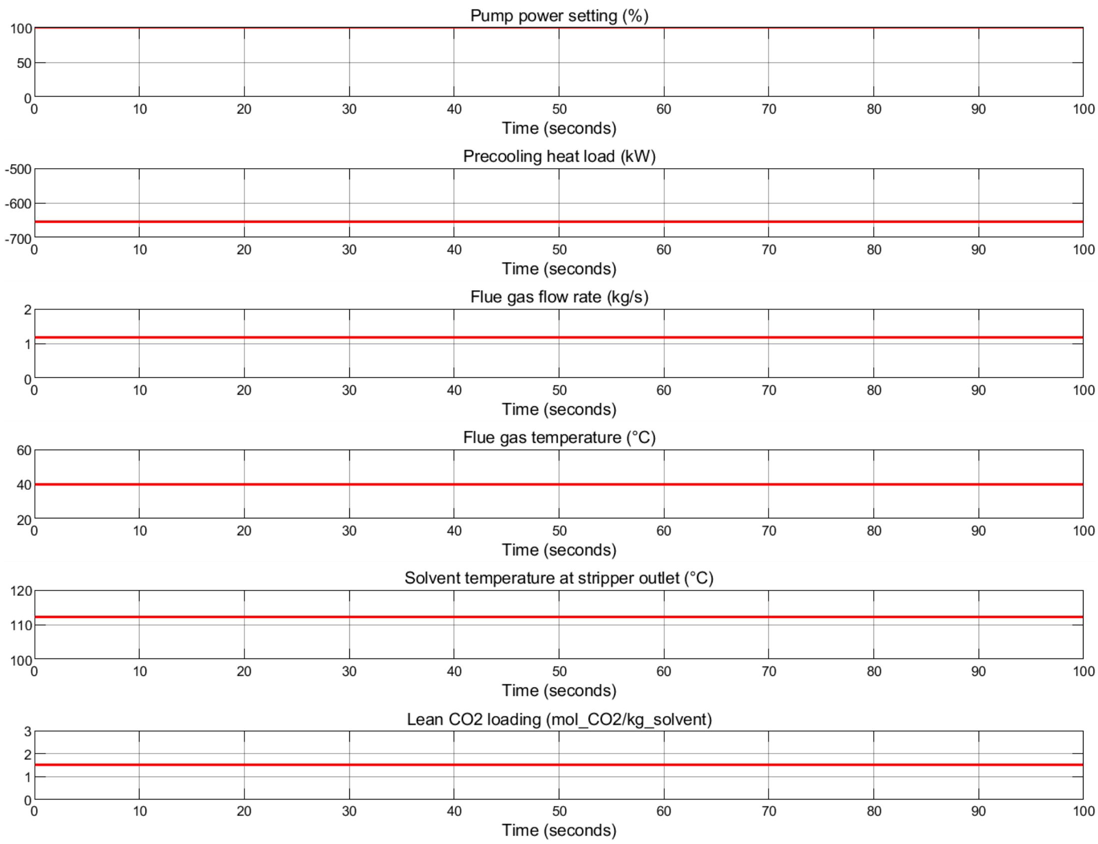

Figure 29. *CO_2 absorption process modelling -initial input values.*

Next, the modelling results of a step change of the pump power setting are analyzed when the power setting was dropped from 100 % to 80 % at t=100 s, and other input values were kept as their initial values. The tested input variable change and outputs of this simulation run are plotted below in Figure 30, as red and blue, respectively.

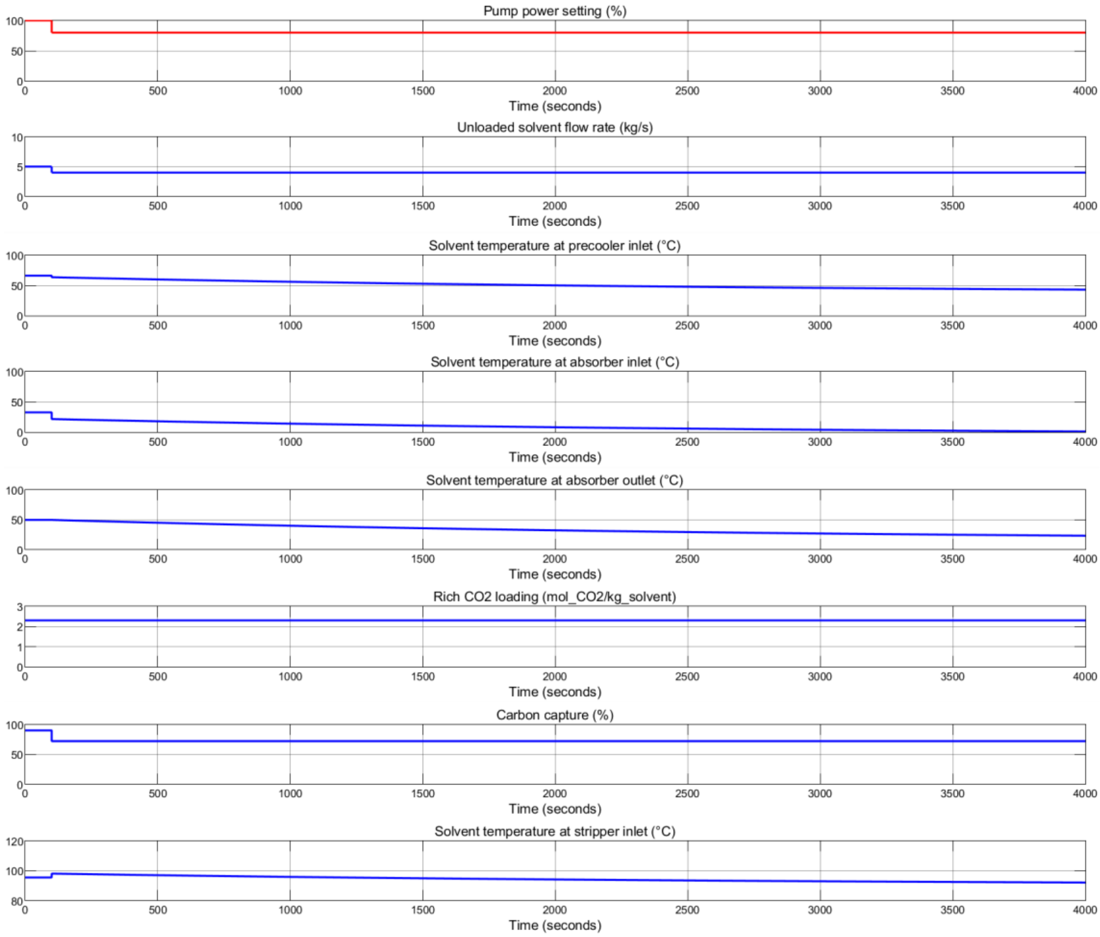

Figure 30. *CO_2 absorption process, pump power setting -step response simulation results.*

The pump power setting change causes an instant change in the unloaded solvent mass flow through the entire system as expected. The lowered mass flow rate improves the performance of the recovery heat exchanger, and a lower temperature difference is first achieved between its fluid sides, which means that the hot side flow cools more and the solvent temperature at precooler inlet is decreased and the temperature at stripper inlet is increased. Because delays based on neither the recovery heat exchanger nor the precooler dimensions were modelled, this effect is seen in the model at the same time as the pump power was decreased. As the precooler load was not changed in the simulation, its cooling load becomes excessive in comparison to the lowered solvent mass flow rate. Because of this, the solvent temperature at the absorber inlet drops more steeply compared to the temperature decrease seen at the precooler inlet at t=100 s.

After the mass flow change has happened, the solvent temperature at the absorber outlet keeps dropping, from which it can be deduced that the heat generated by the absorption process is no longer enough to keep the original absorption operation temperature. This is as expected because the carbon capture percentage and the heat generation drop at the same time as the solvent mass flow, as the original performance can no longer be reached. Additionally, because the mass flow change decreases the absorber inlet temperature, the heat generation in the absorber column would need to increase from the original level instead of decreasing, so that the initial operation temperature could be kept. But as this not the case the operation temperature of the absorber starts to drop, which in the following flow circulations through the system keeps decreasing all the modelled system temperature values as can be seen from the plotted simulation results.

Next, the modelling results of a step change of the precooling heat load are analyzed. In the test run, the cooling load was changed to -550 kW at t=100 s, and other input values were kept as their initial values. The tested input variable change and outputs of this simulation run are plotted below in Figure 31, as red and blue, respectively.

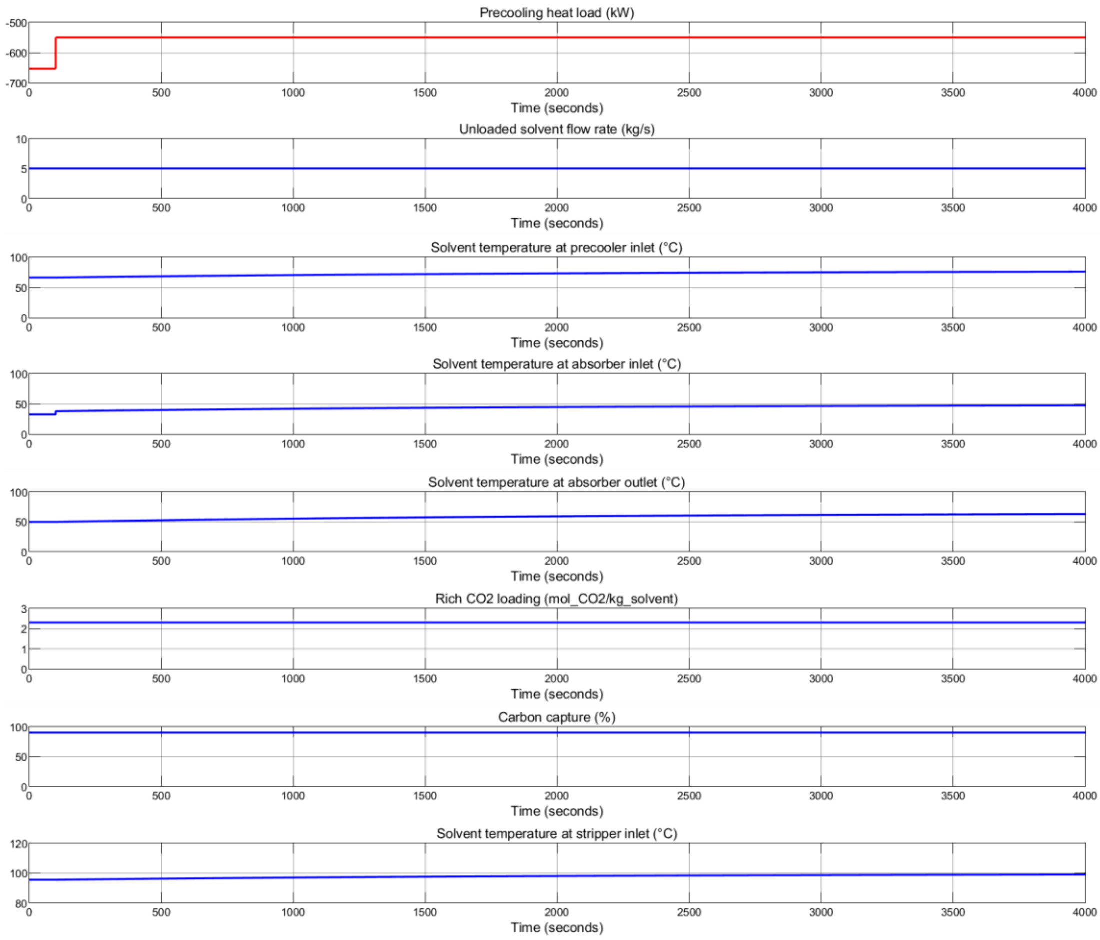

Figure 31. *CO_2 absorption process, precooling heat load -step response simulation results.*

When the precooling load changes, it directly affects only the solvent temperature at the absorber inlet, as can be seen from its instantaneous rise at t=100 s. Because the capture performance and therefore the heat generated by the absorption process stay unaffected, just the change in the absorber inlet temperature starts to slowly affect the absorber operation temperature and all the other temperatures values in the system. Because of these rising temperature values in the absorption side of the carbon capture system, the cold and hot flow side inlet temperatures of the recovery heat exchanger start getting closer to each other, which weakens its performance. During the simulated timeframe, this performance however changes rather little, as can be seen from the plotted solvent temperature at the stripper inlet. The temperature difference between the heat exchanger's fluid sides is always equal to the temperature difference between the solvent at stripper inlet and solvent at stripper outlet, and as the stripper outlet temperature was modelled as a constant in this simulation run, the change of the stripper inlet temperature must be equal to the change of the temperature difference between the recovery heat exchanger's fluid sides. This change based on the plotted results is approximately 4 °C during the simulated timeframe.

Tests of changing the other absorption process input values were not analyzed to keep the work's length reasonable. Changing the flue gas flow rate can be expected to have somewhat similar results compared with the change of precooling heat load. A lower flue gas mass flow would increase the absorber operation temperature and a higher mass flow would decrease it, while the molar amount of captured CO_2 would stay the same unless the flue gas flow rate would drop so low that the maximum CO_2 loading could no longer be reached during absorption. The carbon capture percentage would also obviously change if the flue gas flow rate would. Changing the flue gas stream's inlet temperature should also have similar results compared with the change of precooling load, as it should affect the absorber operation temperature identically as a change in absorber inlet solvent temperature would.

In the previously analyzed tests the stripper model's outlet conditions were modelled with user determined input values, and step changes of these input values were also not tested like mentioned in the previous paragraph. If tested, these stripper model's outlet values (solvent temperature and lean CO_2 loading) would need to be changed at the same time, because the lean CO_2 loading value cannot change individually in the system as it depends on the reboiler operation temperature. This means that changing the stripper's operation state would, in an uncontrolled capture system, affect both the absorber's CO_2 capture performance and the temperatures of the whole system, causing major instability.

The stripper model's dynamic behavior is covered next separately from the rest of the capture system, because all the other modelled components of the developed carbon capture model, except the stripper column and the reboiler unit, were already included in the previously analyzed absorption process tests. The modelling parameters used in the stripping process modelling can be found from Appendix E of this work, and the initial input values of the analyzed stripping process simulations are presented below in Figure 32.

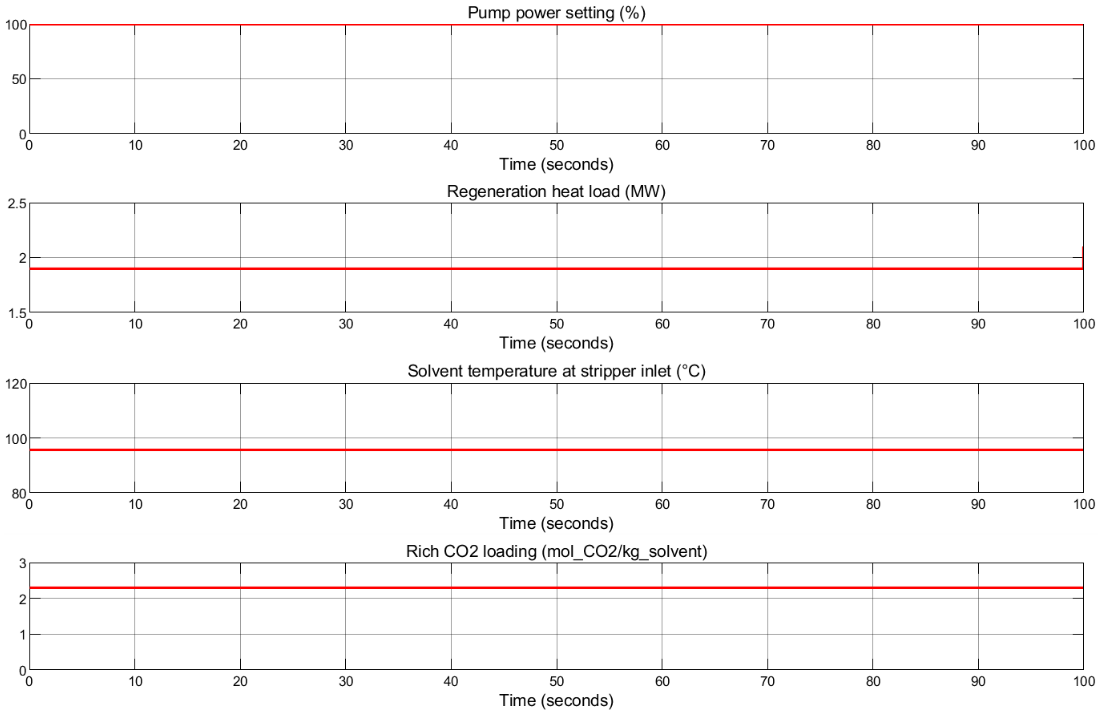

Figure 32. *CO_2 stripping process modelling -initial input values.*

Next, the modelling results of a step change of the reboiler regeneration heat load are analyzed. In the test run, the regeneration heat load was raised from 1.9 MW to 2.1 MW at t=100 s, and other input values were kept as their initial values. The tested input variable change and outputs of this simulation run are plotted below in Figure 33, as red and blue, respectively.

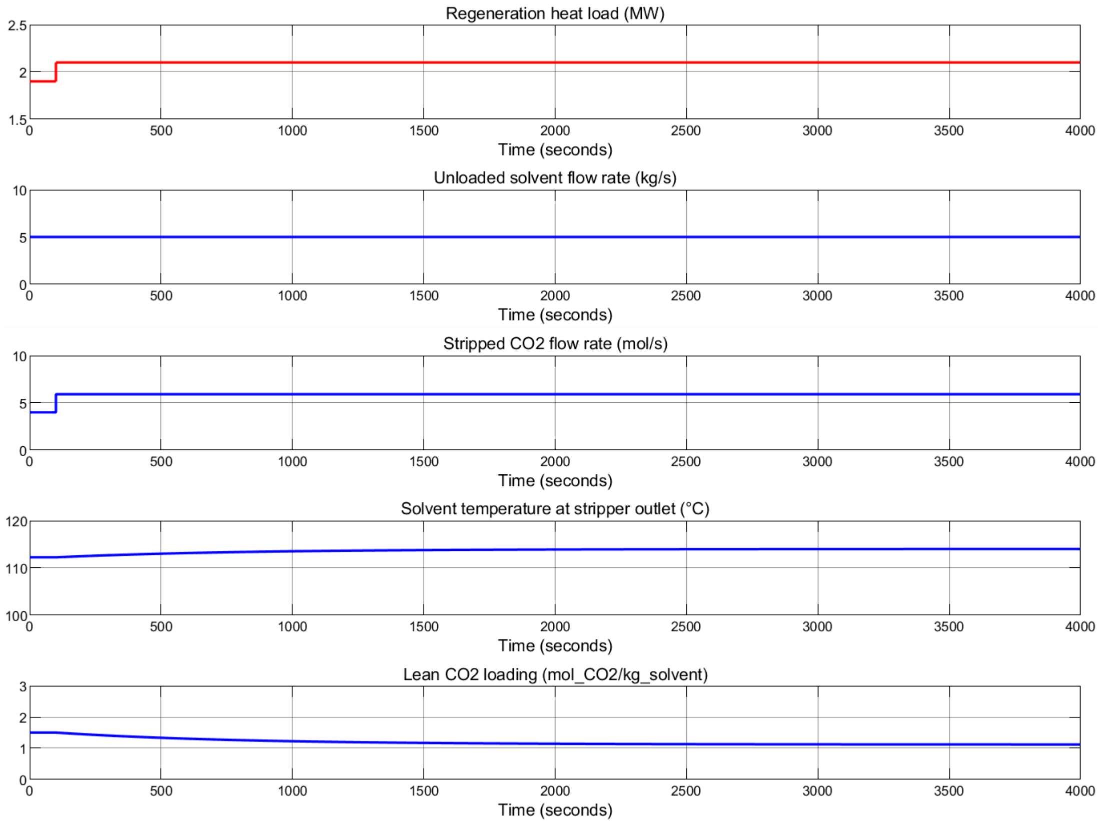

Figure 33. *CO_2 stripping process, regeneration heat load -step response simulation results.*

In the analyzed simulation run, the change in reboiler heat load instantaneously affects the flow rate of the stripped CO_2 gas, but because the solvent enters the liquid sump after the actual stripping has happened, the process' outlet conditions take some time to reach new steady state values. Estimating from Figure 33 it seems that these new steady state operation conditions were reached during the simulated timeframe, or the changes in solvent temperature and CO_2 loading at the stripper (reboiler) outlet at the end of the simulation must be too minor to be noticeable.

Next, the modelling results of a step change of the pump power setting are analyzed. In the test run, the power setting was decreased from 100 % to 80 % at t=100 s, while other stripping process input values were kept as their initial values. The tested input variable change and outputs of this simulation run are plotted below in Figure 34, as red and blue, respectively.

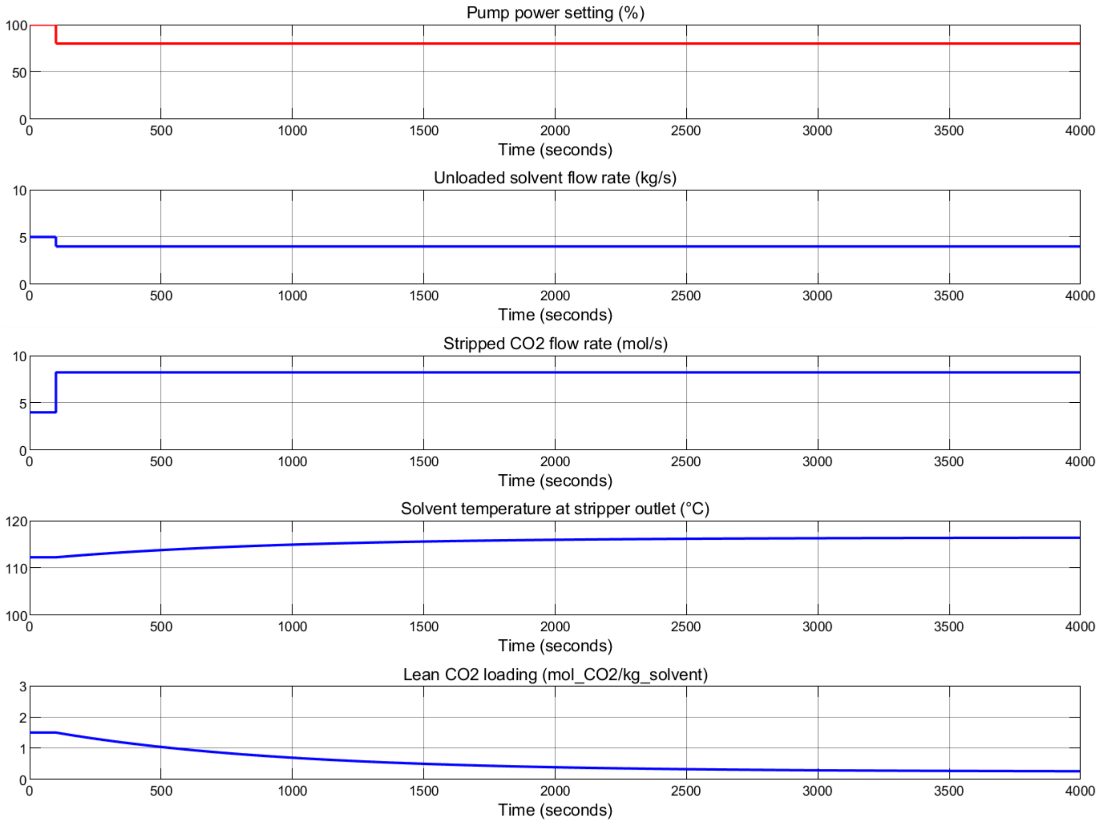

Figure 34. *CO_2 stripping process, pump power setting -step response simulation results.*

Other than obviously affecting the solvent flow rate through the system, these simulation results are similar to those of the previous reboiler heat load test. When the mass flow through the stripper decreases the heat load becomes able to heat the solvent to a higher temperature during the stripping, and because the CO_2 loading decreases more rapidly in higher temperatures, as seen earlier in Figure 16, the amount of stripped CO_2 is increased even though the amount of treated solvent has decreased. It also again seems that new steady state outlet conditions were reached during the simulated timeframe.

Step response tests were not carried out with the stripper's inlet condition changes, again to keep the work's length reasonable. But these test results should be obvious as a lower CO_2 loading at the stripper inlet would decrease the loaded solvent mass flow, and should therefore increase the reboiler operation temperature, and decrease the lean CO_2 loading at the outlet, similarly as happened in the analyzed pump power setting test, where the mass flow also decreased. However, unlike in the pump power setting test the amount of stripped CO_2 might decrease, because the lean CO_2 loading value change would need to be exactly equal to the change of the inlet CO_2 loading value, so that the capture rate would stay unaffected. If the stripper's inlet temperature would be changed, it should have similar results as in the earlier reboiler heat load test, where a lower solvent inlet temperature would worsen the stripping performance, and a higher inlet temperature would improve the stripping performance.

5.1.4 Liquid CO_2 Storage System

In this subchapter, the open loop behavior of the developed CO_2 storage system model is analyzed. The parameters used in the CO_2 storage system modelling can be found from Appendix F, and the initial input values of the analyzed simulation runs are presented below in Figure 35.

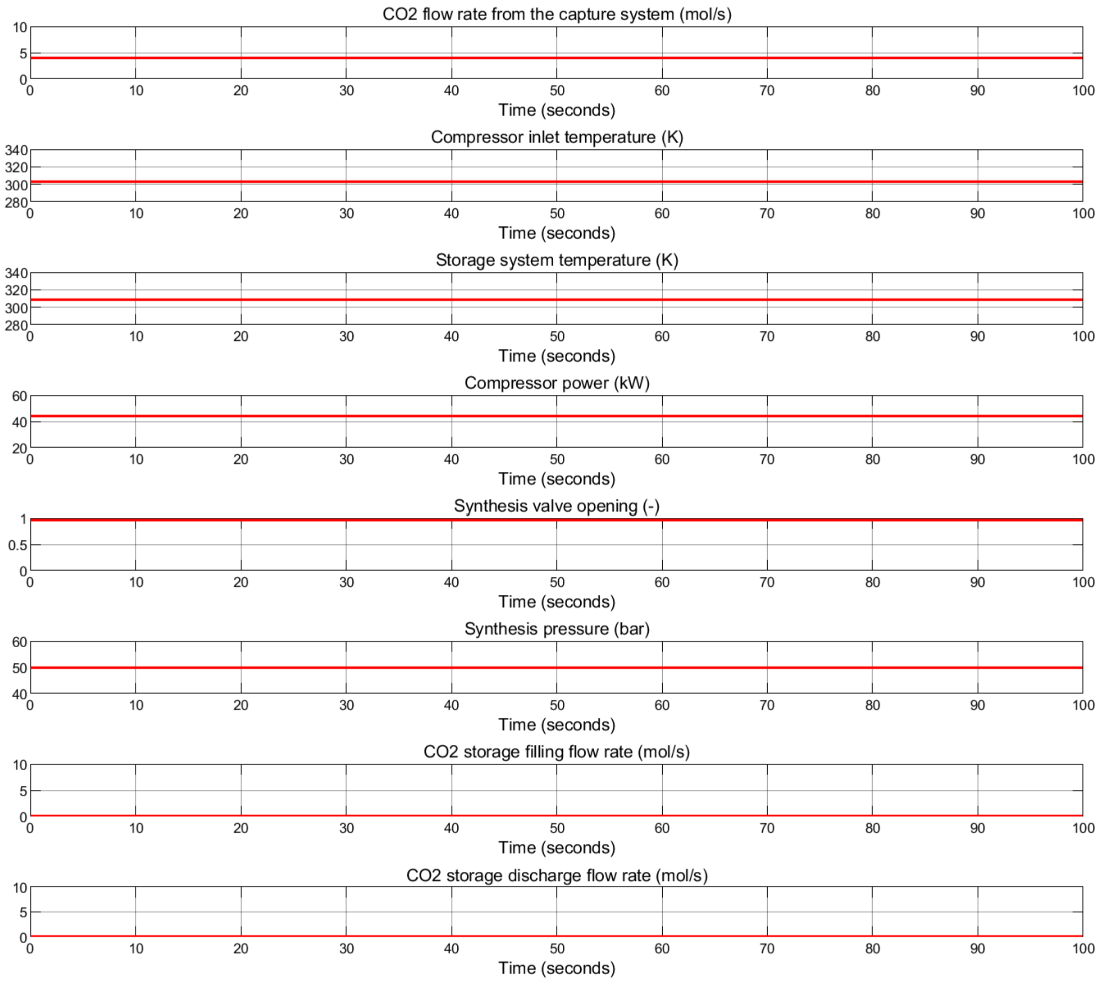

Figure 35. *Liquid CO_2 storage system modelling -initial input values.*

Next, the modelling results of a step change of the compressor power are analyzed. In the test run, the compressor power was decreased from 43.97 kW to 35 kW at t=100 s, and other input values were kept as their initial values. The tested input variable change and outputs of this simulation run are plotted below in Figure 36, as red and blue, respectively.

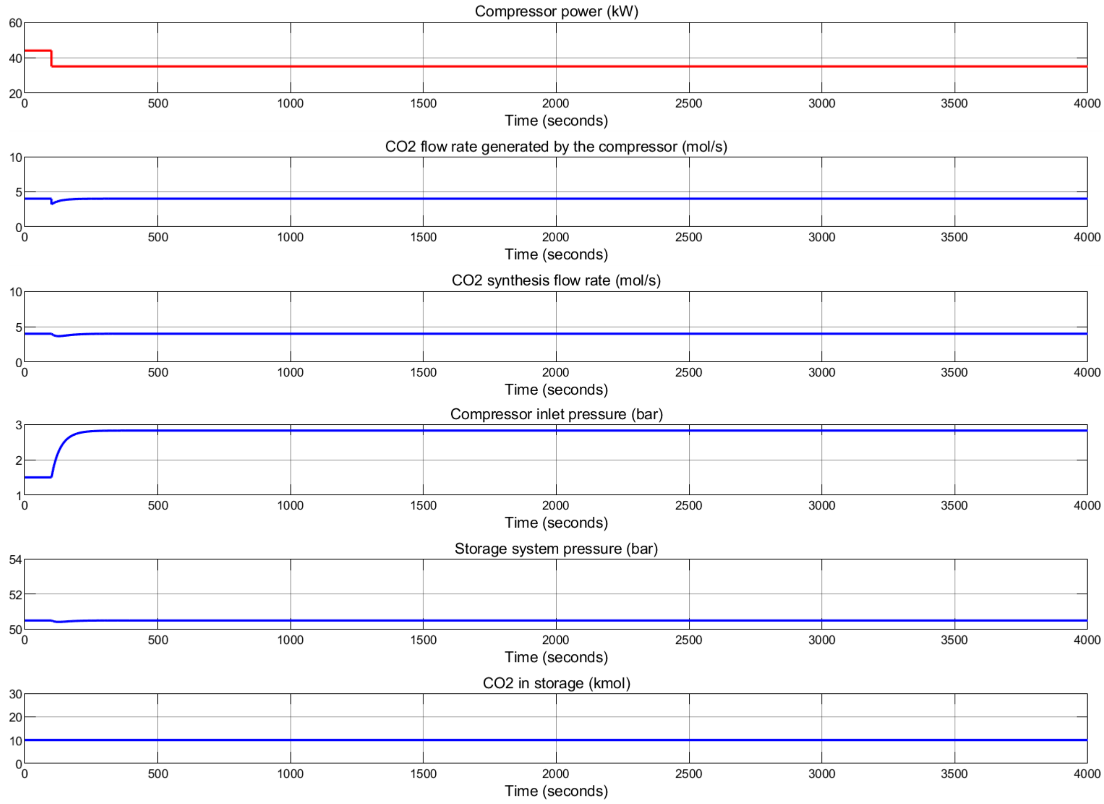

Figure 36. *Compressor power -step response simulation results.*

At t=100 s when the compressor power is dropped it instantly decreases the CO_2 flow rate generated by the compressor, and because of this CO_2 starts accumulating to the compressor feedline raising the compressor inlet pressure. At the same, time the lowered CO_2 flow rate into the storage system decreases the storage system pressure, and the synthesis flow rate out of the system because the storage system pressure is also the control valve's inlet pressure. Approximately a couple of minutes after the compressor power change the system has stabilized again because the amount of power needed by the compressor to achieve the system pressure decreases at the same time as the compressor inlet pressure rises, and a new steady state has at this point been found.

Next, the modelling results of a step change of the synthesis valve opening are analyzed. In the test run, the valve opening was reduced from 0.96 to 0.35 at t=100 s, and other input values were kept as their initial values. The tested input variable change and outputs of this simulation run are plotted below in Figure 37, as red and blue, respectively.

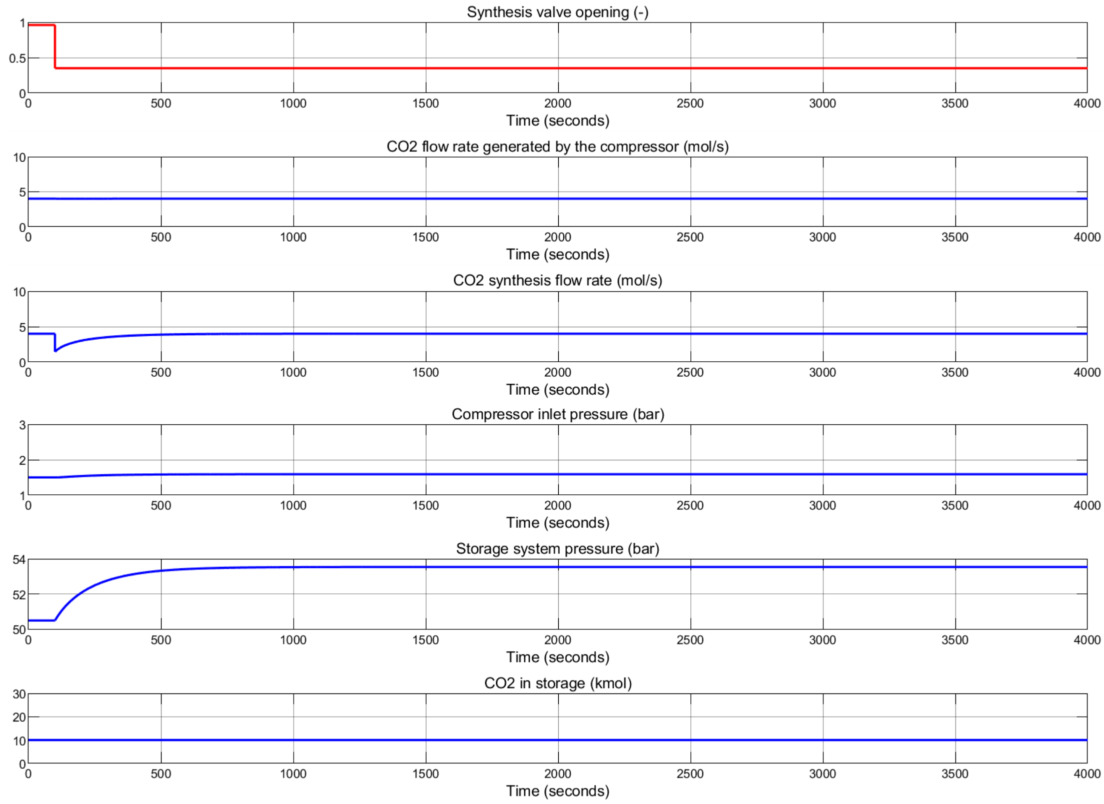

Figure 37. *Synthesis valve opening -step response simulation results.*

At t=100 s when the valve opening is reduced the synthesis flow rate decreases because of it, and gas starts to accumulate to the CO_2 storage system piping, which raises the storage system pressure. This raise in the compressor back pressure also starts decreasing the flow rate generated by the compressor, but in this simulation run, the change in the generated CO_2 molar flow is so small that it cannot really be noticed from the plotted scale. However, this effect can be seen from the small rise of the compressor inlet pressure value, which must happen because the compressor is for a little while unable to fully transfer the captured CO_2 flow to the storage system. At t=1000 s or so, the system has again stabilized to a new steady state, where the CO_2 flow rates generated by the compressor and allowed by the valve opening are equal to the flow rate of captured CO_2, which was given to the model as a constant input value.

Next, the modelling results of a step change of the storage discharge flow rate are analyzed. In the test run, the storage discharge flow was increased from 0 mol/s to 1 mol/s at t=100 s, and other input values were kept as their initial values. The tested input variable change and outputs of this simulation run are plotted below in Figure 38 as red and blue, respectively.

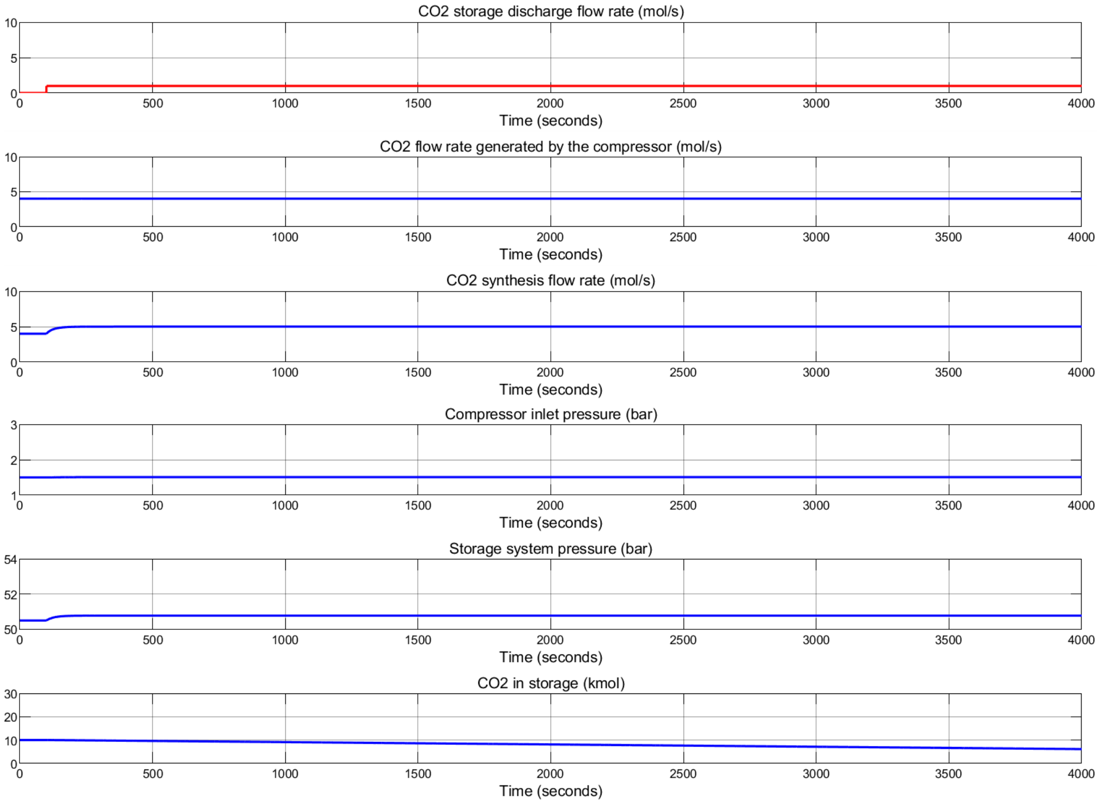

Figure 38. *CO_2 storage discharge flow rate -step response simulation results.*

At t=100 s the storage system pressure starts to rise because of the added storage discharge flow, as the current valve position does not allow it to go through it in addition to the initial synthesis flow rate. But approximately a minute after the change the system has stabilized to a new steady state, where the synthesis flow rate has increased from 4 mol/s to 5 mol/s because the now higher system pressure forces a higher flow rate through the synthesis valve. During the simulation run, the amount of CO_2 in the storage decreases consistently after t=100 s, when the storage discharge flow was changed from 0, as the new storage discharge flow value is given to the model as a constant input value after that.

The pressure change inside the storage system again also affects the compressor operation by decreasing its generated flow rate and increasing the compressor inlet pressure. But the changes of these values are so minimal before a new steady state is achieved, that they cannot be seen from the previously presented figure's scales. The changes of these values are presented separately for the previous test run in Figure 39 below, where the y-axis scales have been updated.

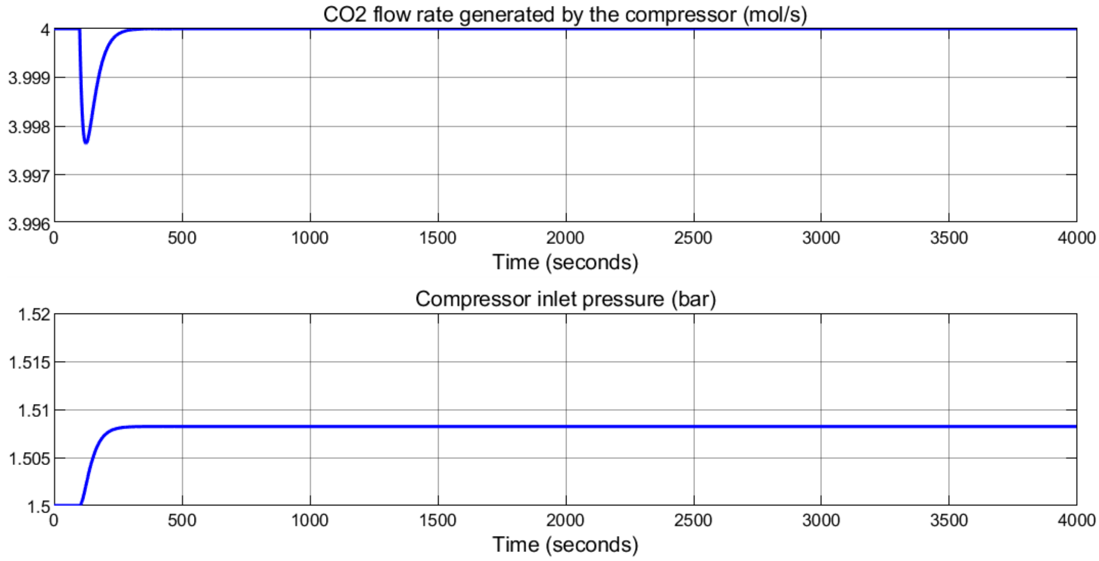

Figure 39. *CO_2 storage discharge flow rate -step response simulation results for compressor generated flow rate, and compressor inlet pressure.*

From the figure above, it can be observed that the compressor related values in the model do behave as expected, and that the resulting compressor inlet pressure change caused by the added storage discharge flow is indeed very minimal. Storage filling flow rate step response test was not considered necessary after this test, as its resulting changes to the modelled values are assumed to just happen in the opposite direction in comparison with the now analyzed results of the storage discharge flow rate test.

Changing the CO_2 flow rate from the capture system was not tested, because it was assumed that the previously analyzed tests had already comprehensively shown how the modelled pressures would behave when CO_2 gas amount would either increase or decrease at the compressor inlet or at the valve inlet. Step responses to the compressor inlet temperature and storage system temperature changes were also not tested, because these temperature values were modelled as input variables instead of just constants only so that they could be changed for the duration of a full simulation run if wanted. The synthesis was also assumed to happen in constant pressure so its pressure, which is also the valve's downstream pressure, was modelled as a constant.

5.1.5 Green Methanol Synthesis

In this subchapter, the open loop behavior of the developed methanol synthesis model is analyzed. The parameters used in the methanol synthesis process modelling can be found from Appendix G, and the initial input values of the analyzed simulations are presented below in Figure 40.

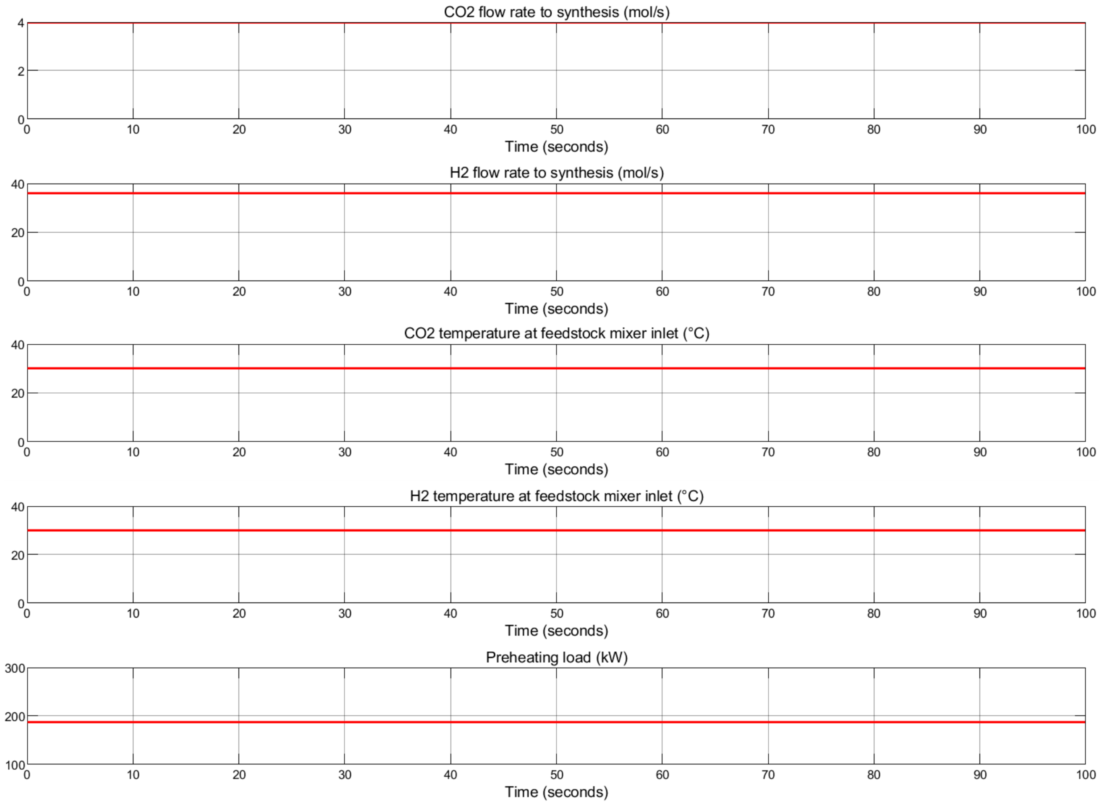

Figure 40. *Methanol synthesis modelling -initial input values.*

Next, the modelling results of a step change of the preheating load are analyzed. In the test run, the preheating load was increased from 187 kW to 240 kW at t=100 s, and other input values were kept as their initial values. The tested input variable change and outputs of this simulation run are plotted below in Figure 41, as red and blue, respectively.

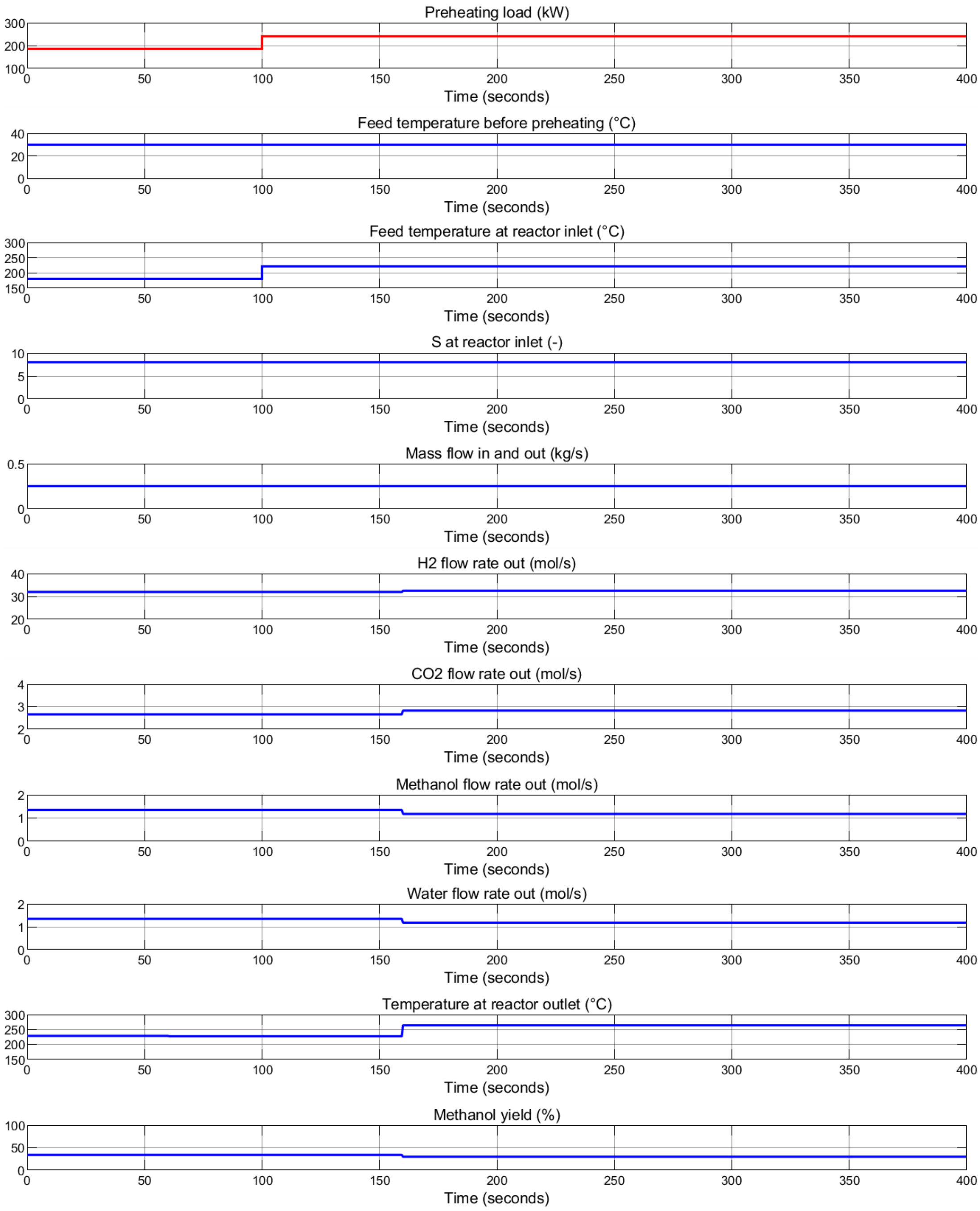

Figure 41. *Preheating load -step response simulation results.*

The preheating load change affects the temperature at the reactor inlet instantly, as any delay caused by actual heater dimensions was not modelled. The preheating change has no effect on the feed composition (S) or mass flow through the system, but because of the reactor inlet temperature change, it does affect the methanol yield. This change in the yield can be seen at the reactor outlet approximately 60 s after the reactor inlet temperature has changed, when all the outlet flow rates and the outlet temperature change.

This analyzed test is assumed to have similar results as tests, where either of the feedstock mixer inlet temperatures would be changed. The only difference between these results should be that a mixer inlet temperature change would also affect the temperature of the feed before preheating, unlike in the analyzed preheating load change test. Because of their assumed similarity, these tests were not analyzed separately.

Next, the modelling results of a step change of the hydrogen flow rate to synthesis are analyzed. In the test run, the hydrogen flow rate was decreased from 36 mol/s to 25 mol/s at t=100 s, and other input values were kept as their initial values. The tested input variable change and outputs of this simulation run are plotted below in Figure 42, as red and blue, respectively.

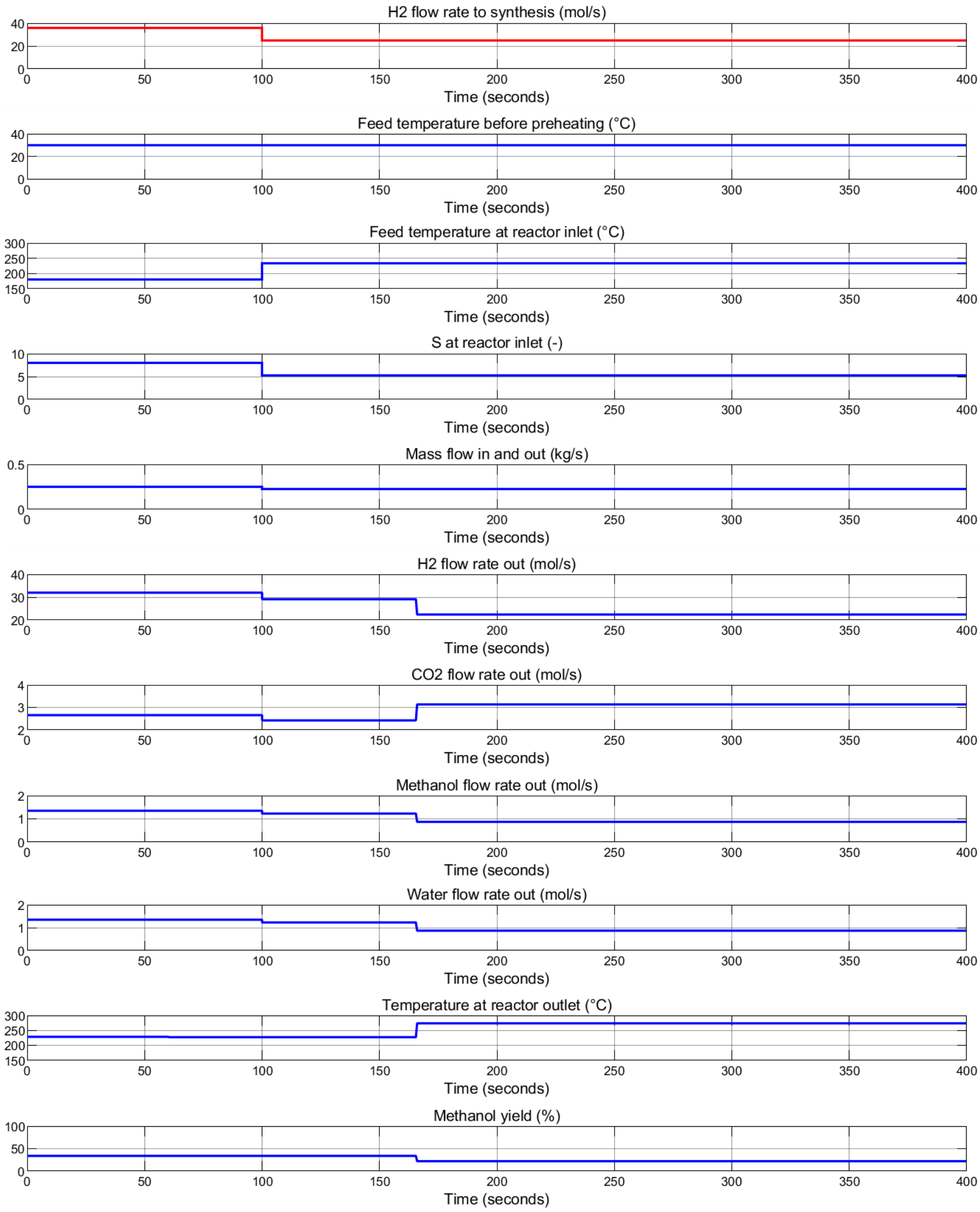

Figure 42. *Hydrogen flow rate to synthesis -step response simulation results.*

At t=100 s the hydrogen flow rate drop immediately affects the reactor inlet temperature, feed composition (S), mass flow through the system, and the molar flow rates of the product substances. The reactor inlet temperature increases because the preheating load stays unchanged while the mass flow through the preheater drops, and molar flow rates of the products also all drop because of the mass flow when they are not pushed through the reactor as quickly anymore. The effect that the feed composition and reactor inlet temperature changes have on the methanol yield can again be seen after a delay which depends on the reactor residence time. Because of the mass flow drop, in this test, the delay increases after t=100 s, and it takes approximately 65 s to see the composition change's effect on the product flow rates and on the reactor outlet temperature.

5.2 Proposed Control Solutions

Based on the simulation tests that were analyzed in the previous subchapters, control solutions could be proposed for each subprocess of the developed plant concept. The proposed control solutions are provided in the following subchapters as control diagrams, which are also discussed in the text. The aim of the following chapters is to answer what variables in the systems either need to or could be controlled, what variables could be manipulated to affect these chosen control variables, and what measurements could be utilized. Controls that would cover the considered plant concept fully however could not be proposed, because of the modelling simplifications and omissions that had to be done to keep the scope of the work reasonable.

To draw attention to the proposed solutions, controller and transmitter symbols were colored yellow in the presented control diagrams. All transmitter symbols were however not included in the diagrams to simplify them and to increase their readability. When they were deemed unnecessary to include and why is discussed in detail separately for each of the presented control diagrams.

5.2.1 Proton Exchange Membrane Electrolysis

Based on the analyzed simulation tests, the amount of produced hydrogen could be controlled by manipulating the operation current of the PEM electrolyzer and the operation temperature by manipulating the flow rate of water that is fed to the electrolyzer, if the water feed itself is assumed to be provided at a constant temperature.

A control diagram is presented below in Figure 43 for the proposed PEM electrolyzer controls. The control diagram is simplified by not including transmitter symbols in cases where the measured value is the same as the controlled variable, which in the case of the PEM electrolyzer concerns all the proposed controls. The operation temperature of the electrolyzer is assumed to be controlled by manipulating the speed of a frequency drive pump and the produced hydrogen flow rate by adjusting the operation current with power electronics. It is assumed in this work that the operation current of an electrolyzer could be manipulated as wanted, but how the power electronics themselves work was considered out of the scope of this study.

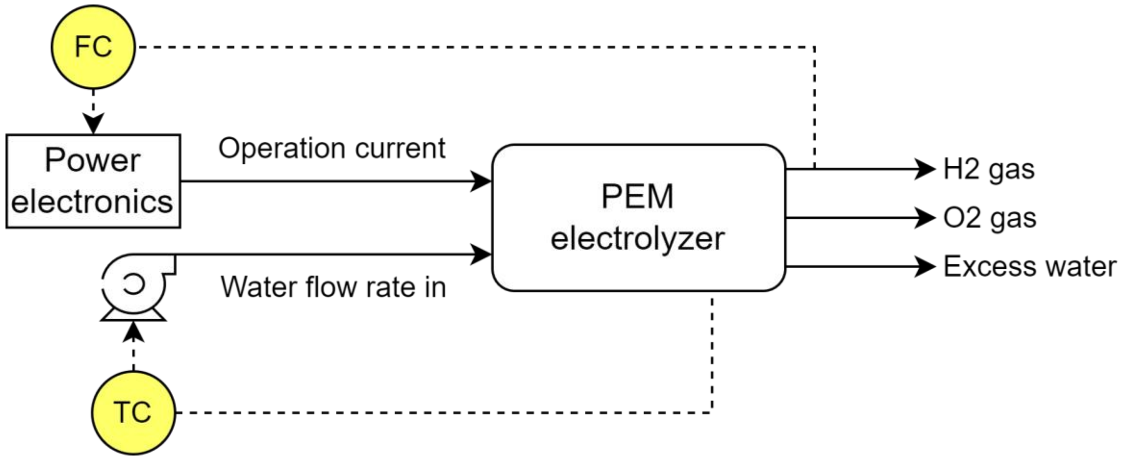

Figure 43. *Control diagram for the PEM electrolyzer.*

5.2.2 Compressed Hydrogen Storage System

Based on the analyzed simulation tests, the flows in and out of the hydrogen storage tank could be controlled by manipulating the compressor power and discharge valve opening as expected. These flows could be controlled to reach the wanted synthesis hydrogen flow rate setpoint in scenarios where the setpoint differs from the hydrogen flow rate coming from the PEM electrolyzer system.

Compressed hydrogen storage operation related heating and cooling phenomena were not modelled in this work to reduce the modelling scope, and therefore a control solution for the tank temperature could not be suggested either. However, in a real system, it would be important to take tank temperature limits into consideration to ensure safe operation. The standardized temperature range, which is allowed for compressed hydrogen storage systems used in vehicle applications, is currently specified to be -40 to 85 °C. (Maus, et al., 2008) This temperature range is given as a guiding example because operation temperature limits for storage vessel types more commonly used in stationary hydrogen gas applications could not be found.

A control diagram is presented below in Figure 44 for the hydrogen storage system controls that could be proposed, which only include a singular flow controller. This controller should be used to control both the storage compressor power and discharge valve opening. Controls were not suggested for the intercooling of the compressor train, which was modelled in the work with just one compression stage. The transmitter symbol was again omitted, as the measured value used by the controller would be the same as the controlled variable.

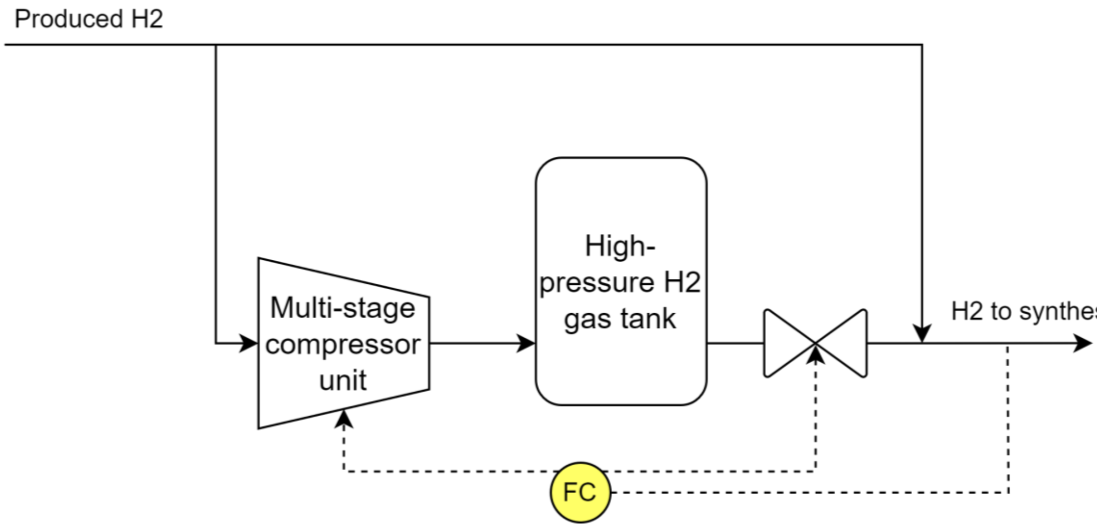

Figure 44. *Control diagram for the hydrogen storage system.*

5.2.3 Post-combustion Carbon Capture System

Based on the analyzed simulation tests, the amount of captured CO_2 could be controlled in the absorption process by varying the solvent flow rate by manipulating the power or speed setting of the solvent pump. However, a change in the solvent flow rate would also affect the temperature levels inside the system, which should therefore be controlled as well. In this work, the absorber outlet temperature is suggested to be the temperature value that should be controlled. It could be controlled by manipulating the precooling load of the precooler, which in the capture system is located before the absorber column. The outlet conditions of the stripping process could be controlled by manipulating the regeneration heat load. In the proposed plant concept, the recovery heat exchanger was left to be totally uncontrolled.

A control diagram is presented below in Figure 45 for the proposed carbon capture system controls. For the condenser, which was not modelled, no controls were suggested in this work. Level control is suggested for the rich solvent pump, even though it was not modelled, and the lean solvent pump is proposed to be the actuator used to control the CO_2 capture percentage. Transmitter symbols were again excluded from the diagram, when possible. However, flue gas composition and flow measurement transmitters had to be included in the diagram because the controlled variable (carbon capture percentage) whose control they would be utilized for, is neither of these measured values. The carbon capture percentage controller is marked in the diagram as QC, which stands for a quality controller, while composition transmitters are marked in the diagram as AT, and flow transmitters as FT. The stripping process on the other hand is proposed to be controlled based on the reboiler temperature, as this measurement should be easier to implement than a CO_2 loading measurement if one could even be possible.

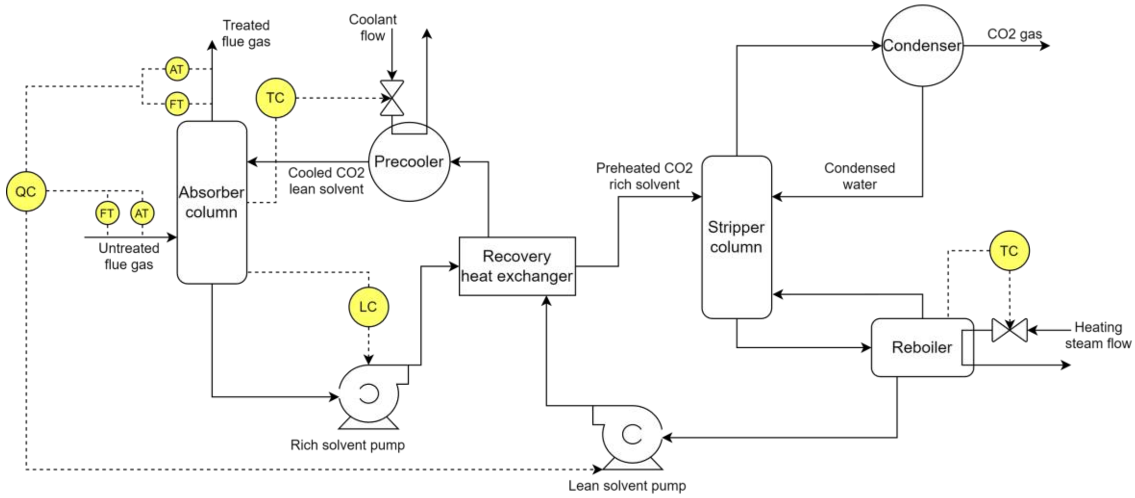

Figure 45. *Control diagram for the carbon capture system.*

The proposed control solution can be classified under the solvent flow control method, which was discussed in the literature review, as the CO_2 capture rate in the absorber is proposed to be controlled by adjusting the solvent flow rate. From the analyzed stripping process simulation results, it could be seen how slowly the stripper outlet conditions would change after the regeneration heat load of the stripping would have changed. This shows that the CO_2 loading control method, which was also discussed in the literature review, does indeed seem unsuitable for the process. It is still important to mention that in the modelled stripper column the solvent sump volume was set as unrealistically large in order to also estimate lag time that would be caused by the process components which were not modelled, like actual pipe lengths and possible solvent buffer tanks.

5.2.4 Liquid CO_2 Storage System

Based on the analyzed simulation tests, it can be assumed that the inlet pressure of the CO_2 compressor could be kept stable by manipulating the compressor power. The opening of the synthesis valve could be manipulated so that the wanted CO_2 flow rate would be provided for the methanol synthesis reactor, and the liquid storage could then be controlled so that the storage system pressure would not change. This would mean that in situations where the wanted CO_2 synthesis flow rate would be less than the flow rate generated by the compressor, CO_2 should be taken from the liquid storage by manipulating the evaporator heating load, or in the opposite case, CO_2 should be fed to the storage by increasing the cooling load of the CO_2 condenser.

A control diagram is presented below in Figure 46 for the proposed CO_2 storage system controls. Like somewhat implied earlier, controls are also proposed for the evaporator and condenser in the system, even though they were not modelled. Controls were again not suggested for the intercooling of the compressor train, which was modelled with just one compression stage, and the amount of compressor stages that would really be needed is unknown. Transmitter symbols were again omitted from the diagram when the measured values used by the controllers would be the same as the controlled variables.

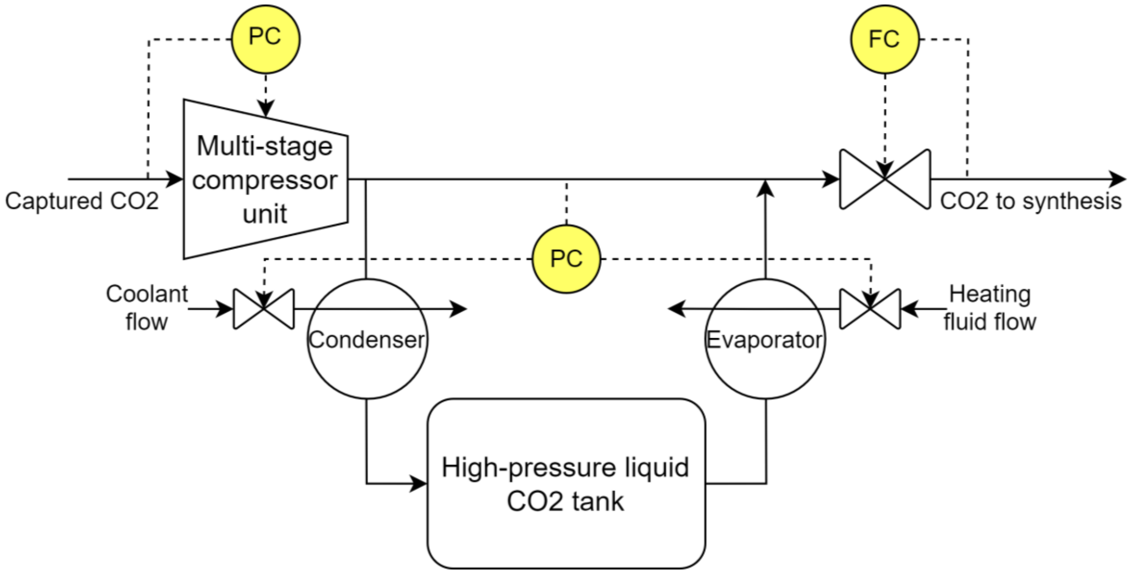

Figure 46. *Control diagram for the CO_2 storage system.*

5.2.5 Green Methanol Synthesis

Based on the analyzed simulation results, the temperature at the reactor inlet could be controlled by adjusting the preheating, so that the synthesis reactor would stay in the allowed operation temperature range. The flow rates of the feedstock substances should also be controlled to keep the feedstock composition sensible, but these feedstock flow controls are not actually a part of the methanol synthesis controls, and these synthesis flow controls have already been suggested for the storage systems of the plant concept.

A control diagram is presented below in Figure 47 for the proposed methanol synthesis system controls. The first preheating stage, which is done by recovering heat from the synthesis products stream, is proposed to be uncontrolled so that as much heat would be recovered as possible. The synthesis inlet temperature should therefore be controlled by manipulating the heating load of the second preheating stage instead. Because the product separation process was totally left out of this thesis' scope, no controls are suggested for it or the recycled feed substance flows. The transmitter symbol of the temperature transmitter was again omitted from the diagram because the controlled value of the only suggested control was also this same temperature.

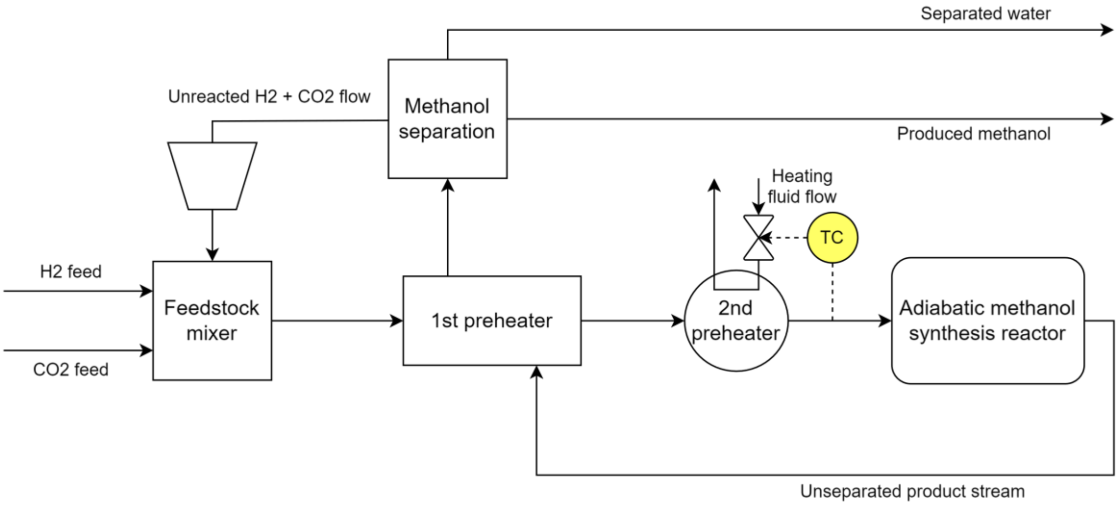

Figure 47. *Control diagram for the methanol synthesis.*

5.3 Future Continuation and Development

The next step after this work is to add the proposed control solutions into the developed simulation models to the extent that is possible, and to test these controls. All the proposed controls cannot yet be accurately implemented with the current model structures due to some of the omissions that were made when modelling the process. For example, with the current models heat exchanger controls would have to be tested by manipulating the heat loads directly, rather than manipulating valve positions on one fluid side of the exchangers, like in the proposed control diagrams. At this stage the used controller types should also be decided, and these controllers tuned.

The simulation models created in this work included many assumptions and simplifications that were discussed in the subchapters of Chapter 4, which made it possible to reach the extensive modelling scope, but which also decreased the accuracy of the models. One of the biggest problems faced in this work was the lack of available actual measurement data from similar processes. If there were available data, it could have been used both for steering the modelling task to include the most important behavioral traits of the processes, and to later validate simulation results of the models.

Because the simulation results of the developed models could not be validated against real measurement data, improvement suggestions to the current models cannot be given based on hard evidence and can only be suggested based on the author’s own understanding of the modelled process. In addition to improvement suggestions meant to increase the simulation accuracy of the models created in this work, suggestions about how the modelling scope could be expanded in the future can be given.

To improve the accuracy of the PEM electrolyzer modelling, it is suggested that the operation temperature's effect on its efficiency should be added to the current model. In practice, this means that the temperature relations of all the cell voltage modelling parameters ($r, j_0,\ j_L, \alpha$), which were fixed as constant in this work, should be researched, and added to the electrolyzer model. The hydrogen storage model's accuracy could be improved by also modelling the heating and cooling phenomena of the gas tank instead of modelling the tank at just constant temperature, like was done in this work. In general, almost all the developed models could also be improved by modelling the heat losses to the environment, and by including heat exchangers' dimensions in the models, unlike done previously, which meant that the modelled exchangers' performance always changed in an instant.

Among the previously omitted process parts, which were not modelled in this work, the methanol separation process and the recycle flows of the unreacted feedstock substances back to the synthesis process are seen by the author as the most important things that the modelling should be expanded to cover in the future. This is because the recycle flows of the synthesis raw materials would give an additional possibility to control the composition of the feedstock flow that is fed to the methanol reactor. Some smaller and easier additions that could be considered are for example adding condenser and evaporator models to the CO_2 storage system modelling.

6. CONCLUSIONS

The main objectives of this thesis were to assemble, design and model a Power-to-Methanol plant concept, and to develop control solutions for it. In a broader sense, the aim of the work was to gain knowledge of automation challenges and operational flexibility of Power-to-X technologies. Power-to-X term is used to refer to processes where renewable electricity is converted to different products, which are easier to store, and transport compared to electricity. Different Power-to-X concepts could accelerate the ongoing energy transition by providing grid balancing capability, energy storage solutions, alternative fuels to replace fossil fuels with, and use cases for CO_2. Preparing for this future scenario where Power-to-X processes would become more common is seen as the motivation for this study, where Power-to-Methanol was the chosen technology under focus.

As no available reference material was found detailing a plant concept that could have been modelled, the plant concept that was modelled in this work had to be designed by the author. This plant concept was built based on a review of scientific literature, where the suitability and technological maturity of known subprocess technologies were analyzed. The plant was modelled by creating separate simulation models for each of the chosen subprocess technologies. These models were tested by running step response tests with chosen input variables to identify possible control variables and to validate that the models behaved as expected and that the model implementation had been done successfully. Based on the analyzed simulation results, control solutions were proposed for the considered Power-to-Methanol plant concept.

A Power-to-Methanol process was considered in this work to be separable into five different subprocesses, which included water electrolysis, hydrogen storage system, carbon capture system, CO_2 storage system, and methanol synthesis. Based on the literature study, PEM was the best suited electrolyzer type for flexible operation and compressed hydrogen storage the best suited storage technology for stationary hydrogen applications, and they were therefore chosen for the developed plant concept. Because the CO_2 source was assumed to be flue gas, only post-combustion carbon capture was studied in detail in the literature review. For the developed plant concept, a simple carbon capture configuration with the most common monoethanolamine based solvent solution and a simple liquid CO_2 storage system were chosen. Finally, for the methanol synthesis a single-pass adiabatic fixed bed reactor was chosen because it was suggested in earlier studies that this simple reactor type could be used for CO_2 hydrogenation, which was the synthesis method studied in this work.

Accurately modelling the chosen technologies of these subprocesses was found out to be very time-consuming due to the large number of process components, chemical phenomena, and physical phenomena to be modelled. The complexity of the previously mentioned phenomena to be modelled also proved challenging in some cases. To reach the extensive modelling scope set in this work, various assumptions and simplifications had to be utilized when planning the simulation models. Additionally, not all model parameter values could be found from reference literature due to the work's scope, contrary to what was originally planned. Instead, some of the used parameter values were just chosen by the author.

The modelling task was approached by first developing and implementing individual subprocess models, while having an intention to later join these subprocess models together. However, during the duration of the work, it was realized how hard it would be to sensibly run and analyze simulation tests of the whole plant model, so results of the full plant simulation model were not analyzed in this work in the end. Instead, the dynamic behavior of the subprocesses was also analyzed individually, by running step response tests with chosen input variables of the developed subprocess simulation models. The model implementation and simulation in this thesis were done with MATLAB Simulink.

Based on the analyzed simulation results and the behavior observed in them, it was possible to propose some control solutions for the plant concept, which was developed in this work. These proposed control solutions are provided in the work as control diagrams for the individual subprocesses of the plant concept. These controls were not tested in this thesis work, and not all proposed controls could even be implemented yet with the current simulation models that were created. Adding the proposed controls into the developed simulation models to the extent that is possible and testing these controls is seen as the next step that should be taken to continue the work done in this thesis, along with generally improving the accuracy of the developed simulation models.

REFERENCES

Adnan, M. A. & Kibria, M. G., 2020. Comparative techno-economic and life-cycle assessment of power-to-methanol synthesis pathways. *Applied Energy,* Volume 278, p. 115614.

Ahn, H., Luberti, M., Liu, Z. & Brandani, S., 2013. Process configuration studies of the amine capture process for coal-fired power plants. *International Journal of Greenhouse Gas Control,* Volume 16, pp. 29-40.

Aliyon, K., Mehrpooya, M. & Hajinezhad, A., 2020. Comparison of different CO2 liquefaction processes and exergoeconomic evaluation of integrated CO2 liquefaction and absorption refrigeration system. *Energy Conversion and Management,* Volume 211, p. 112752.

Antoniou, A., Berastain, A., Hernandez, D. & Celis, C., 2022. Mathematical modelling of coupled and decoupled water electrolysis systems based on existing theoretical and experimental studies. *International Journal of Hydrogen Energy,* 47(40), pp. 17526-17543.

Barthelemy, H., Weber, M. & Barbier, F., 2017. Hydrogen storage: Recent improvements and industrial perspectives. *International Journal of Hydrogen Energy,* 42(11), pp. 7254-7262.

Basile, A. & Dalena, F., 2017. *Methanol: Science and Engineering.* 1st ed. Amsterdam, Netherlands: Elsevier.

Bi, L., Boulfrad, S. & Traversa, E., 2014. Steam electrolysis by solid oxide electrolysis cells (SOECs) with proton-conducting oxides. *Chemical Society Reviews,* 43(24), pp. 8255-8827.

Birta, L. G. & Arbez, G., 2007. *Modelling and Simulation: Exploring Dynamic System Behaviour.* 1st ed. London, UK: Springer London.

Bodner, M., Hofer, A. & Hacker, V., 2015. H2 generation from alkaline electrolyzer. *Wiley Interdisciplinary Reviews. Energy and Environment,* 4(4), pp. 365-381.

Bos, M. J., Kersten, S. R. A. & Brilman, D. W. F., 2020. Wind power to methanol: Renewable methanol production using electricity, electrolysis of water and CO2 air capture. *Applied Energy,* Volume 264, p. 114672.

Bowker, M., 2019. Methanol Synthesis from CO2 Hydrogenation. *ChemCatChem,* 11(17), pp. 4238-4246.

Bozzano, G. & Manenti, F., 2016. Efficient methanol synthesis: Perspectives, technologies and optimization strategies. *Progress in Energy and Combustion Science,* Volume 56, pp. 71-105.

Bui, M. et al., 2014. Dynamic modelling and optimisation of flexible operation in post-combustion CO2 capture plants – A review. *Computers & Chemical Engineering,* Volume 61, pp. 245-265.

Buttler, A. & Spliethoff, H., 2018. Current status of water electrolysis for energy storage, grid balancing and sector coupling via power-to-gas and power-to-liquids: A review. *Renewable & Sustainable Energy Reviews,* Volume 82, pp. 2440-2454.

Carbon Recycling International, n.d. *George Olah - Industrial Scale Renewable Methanol Plant.* [Online] Available at: https://www.carbonrecycling.is/project-goplant [Accessed 15 January 2024].

Carmo, M., Fritz, D. L., Mergel, J. & Stolten, D., 2013. A comprehensive review on PEM water electrolysis. *International Journal of Hydrogen Energy,* 38(12), pp. 4901-4934.

Carriveau, R. & Ting, D. S.-K., 2016. *Methane and Hydrogen for Energy Storage.* Stevenage, UK: The Institution of Engineering and Technology.

Çelebi, Y. & Aydın, H., 2019. An overview on the light alcohol fuels in diesel engines. *Fuel (Guildford),* Volume 236, pp. 890-911.

Cheméo, n.d. *Chemical Properties of Monoethanolamine.* [Online] Available at: https://www.chemeo.com/cid/20-170-0/Monoethanolamine [Accessed 14 May 2024].

Chen, C. & Yang, A., 2021. Power-to-methanol: The role of process flexibility in the integration of variable renewable energy into chemical production. *Energy Conversion and Management,* Volume 228, p. 113673.

Cui, X. & Kær, S., 2020. A comparative study on three reactor types for methanol synthesis from syngas and CO2. *Chemical Engineering Journal (Lausanne, Switzerland : 1996),* Volume 393, p. 124632.

Cui, X., Kær, S. K. & Nielsen, M. P., 2022. Energy analysis and surrogate modeling for the green methanol production under dynamic operating conditions. *Fuel (Guildford),* Volume 307, p. 121924.

de Vasconcelos, B. R. & Lavoie, J.-M., 2019. Recent advances in power-to-X technology for the production of fuels and chemicals. *Frontiers in Chemistry,* Volume 7, p. 392.

Dicken, C. J. B. & Mérida, W., 2007. Measured effects of filling time and initial mass on the temperature distribution within a hydrogen cylinder during refuelling. *Journal of Power Sources,* 165(1), pp. 324-336.

Dieterich, V. et al., 2020. Power-to-liquid via synthesis of methanol, DME or Fischer–Tropsch-fuels: A review. *Energy & Environmental Science,* 13(10), pp. 3207-3252.

Drewry, B. J. & Rochelle, G. T., 2024. Simple model for water wash performance in amine scrubbing for CO2 capture. *Carbon Capture Science & Technology,* Volume 11, p. 100186.

Galassi, M. C. et al., 2014. Assessment of CFD models for hydrogen fast filling simulations. *International Journal of Hydrogen Energy,* 39(11), pp. 6252-6260.

Gallucci, F., Paturzo, L. & Basile, A., 2004. An experimental study of CO2 hydrogenation into methanol involving a zeolite membrane reactor. *Chemical Engineering and Processing,* 43(8), pp. 1029-1036.

Gaspar, J., Jørgensen, J. B. & Fosbøl, P. L., 2015. Control of a post-combustion CO2 capture plant during process start-up and load variations. *IFAC-PapersOnLine,* 28(8), pp. 580-585.

Ghosh, S. & Seethamraju, S., 2021. Process Intensification with a Polar Solvent in Liquid Phase Methanol Synthesis. *Process Integration and Optimization for Sustainability,* 5(4), pp. 827-842.

Godula-Jopek, A., 2015. *Hydrogen Production: by Electrolysis.* 1st ed. Weinheim, Germany: Wiley-VCH.

Gray, M. A., 2010. *Introduction to the Simulation of Dynamics Using Simulink.* 1st ed. Boca Raton, USA: CRC Press LLC.

Gülen, J. & Hall, C., 2017. Optimizing post-combustion carbon capture. *Power engineering (Barrington, Ill.),* 121(6).

Hassan, I. A., Ramadan, H. S., Saleh, M. A. & Hissel, D., 2021. Hydrogen storage technologies for stationary and mobile applications: Review, analysis and perspectives. *Renewable & Sustainable Energy Reviews,* Volume 149, p. 111311.

Hauch, A., Ebbesen, S. D., Jensen, S. H. & Mogensen, M., 2008. Highly efficient high temperature electrolysis. *Journal of Materials Chemistry,* 18(20), pp. 2331-2340.

Hermesmann, M., Grübel, K., Scherotzki, L. & Müller, T. E., 2021. Promising pathways: The geographic and energetic potential of power-to-x technologies based on regeneratively obtained hydrogen. *Renewable & Sustainable Energy Reviews,* Volume 138, p. 110644.

Herrmann, F., Grünewald, M. & Riese, J., 2020. Flexibility of Power-to-Gas Plants: A Case Study. *Chemie Ingenieur Technik,* 92(12), pp. 1983-1991.

Hirscher, M., 2010. *Handbook of Hydrogen Storage: New Materials for Future Energy Storage.* 1st ed. Weinheim, Germany: Wiley-VCH.

International Energy Agency (IEA), 2018. *20 Renewable Energy Policy Recommendations.* [Online]
Available at: https://www.iea.org/reports/20-renewable-energy-policy-recommendations
[Accessed 12 January 2024].

International Energy Agency (IEA), 2023. *World Energy Outlook 2023.* [Online]
Available at: https://www.iea.org/reports/world-energy-outlook-2023
[Accessed 15 January 2024].

International Renewable Energy Agency (IRENA), 2020. *Green hydrogen cost reduction: Scaling up electrolysers to meet the 1.5°C climate goal.* [Online]
Available at: https://www.irena.org/publications/2020/Dec/Green-hydrogen-cost-reduction
[Accessed 22 January 2024].

International Renewable Energy Agency (IRENA), 2021. *Innovation outlook: Renewable methanol.* [Online]
Available at: https://www.irena.org/publications/2021/Jan/Innovation-Outlook-Renewable-Methanol
[Accessed 10 January 2024].

Jackson, S. & Brodal, E., 2018. A comparison of the energy consumption for CO2 compression process alternatives. *IOP Conference Series: Earth and Environmental Science,* 167(1).

Järvinen, L. et al., 2022. Automized parametrization of PEM and alkaline water electrolyzer polarisation curves. *International Journal of Hydrogen Energy,* 47(75), pp. 31985-32003.

Kim, I. & Svendsen, H. F., 2007. Heat of Absorption of Carbon Dioxide (CO2) in Monoethanolamine (MEA) and 2-(Aminoethyl)ethanolamine (AEEA) Solutions. *Industrial & Engineering Chemistry Research,* 46(17), pp. 5803-5809.

Kung, H. H., 1992. Deactivation of methanol synthesis catalysts – a review. *Catalysis Today,* 11(4), pp. 443-453.

Laguna-Bercero, M. A., 2012. Recent advances in high temperature electrolysis using solid oxide fuel cells: A review. *Journal of Power Sources,* Volume 203, pp. 4-16.

Lange, H., Klose, A., Lippmann, W. & Urbas, L., 2023. Technical evaluation of the flexibility of water electrolysis systems to increase energy flexibility: A review. *International Journal of Hydrogen Energy,* 48(42), pp. 15771-15788.

Li, D. et al., 2021. Durability of anion exchange membrane water electrolyzers. *Energy & Environmental Science,* 14(6), pp. 3393-3419.

Li, J. Q. et al., 2020. A study on the prediction of the temperature and mass of hydrogen gas inside a tank during fast filling process. *Energies (Basel),* 13(23), p. 6428.

Li, W. et al., 2022. Low-temperature water electrolysis: fundamentals, progress, and new strategies. *Materials Advances,* 3(14), pp. 5598-5644.

Lin, Y.-J., Chang, C.-C., Wong, D. S.-H. J. S.-S. & Ou, J.-J., 2012. Control strategies for flexible operation of power plant integrated with CO2 capture plant. *Computer Aided Chemical Engineering,* Volume 30, pp. 237-241.

Litster, S. & McLean, G., 2004. PEM fuel cell electrodes. *Journal of Power Sources,* 130(1), pp. 61-76.

Luyben, W. L., 2010. Design and Control of a Methanol Reactor/Column Process. *Industrial & Engineering Chemistry Research,* 49(13), pp. 6150-6163.

MAN Energy Solutions, 2023. *FlexMethanol.* [Online] Available at: https://www.man-es.com/energy-storage/solutions/power-to-x [Accessed 5 March 2024].

Marlin, D. S., Sarron, E. & Sigurbjörnsson, Ó., 2018. Process Advantages of Direct CO2 to Methanol Synthesis. *Frontiers in Chemistry,* Volume 6, p. 446.

Martinez-Moyano, I. J. & Richardson, G. P., 2013. Best practices in system dynamics modeling. *System Dynamics Review,* 29(2), pp. 102-103.

Maus, S. et al., 2008. Filling procedure for vehicles with compressed hydrogen tank. *International Journal of Hydrogen Energy,* 33(17), pp. 4612-4621.

Melideo, D. et al., 2017. CFD simulations of filling and emptying of hydrogen tanks. *International Journal of Hydrogen Energy,* 42(11), pp. 7304-7313.

Methanol Institute, 2023. *Supply/demand raw data.* [Online] Available at: https://www.methanol.org/methanol-price-supply-demand/ [Accessed 10 January 2024].

Mlilo, N., Brown, J. & Ahfock, T., 2021. Impact of intermittent renewable energy generation penetration on the power system networks – A review. *Technology and Economics of Smart Grids and Sustainable Energy,* 6(1), p. 25.

Moradi, R. & Groth, K. M., 2019. Hydrogen storage and delivery: Review of the state of the art technologies and risk and reliability analysis. *International Journal of Hydrogen,* 44(23), pp. 12254-12269.

Mucci, S., Mitsos, A. & Bongartz, D., 2023. Cost-optimal Power-to-Methanol: Flexible operation or intermediate storage?. *Journal of Energy Storage,* Volume 72, p. 108614.

Muhammad, H. A. et al., 2019. Design and optimization of CO2 pressurization system integrated with a supercritical CO2 power cycle for the CO2 capture and storage system. *Energy Conversion and Management,* Volume 195, pp. 609-619.

Mumford, K. A., Wu, Y., Smith, K. H. & Stevens, G. W., 2015. Review of solvent based carbon-dioxide capture technologies. *Frontiers of Chemical Science and Engineering,* 9(2), pp. 125-141.

NIST Chemistry WebBook, 2023. *NIST Standard Reference Database Number 69.* [Online] Available at: https://doi.org/10.18434/T4D303 [Accessed 14 May 2024].

NIST Physical Measurement Laboratory, 2024. *Values of Fundamental Physical Constants.* [Online] Available at: https://www.nist.gov/pml/fundamental-physical-constants [Accessed 14 May 2024].

Nittaya, T., Douglas, P. L., Croiset, E. & Ricardez-Sandoval, L. A., 2014. Dynamic modelling and control of MEA absorption processes for CO2 capture from power plants. *Fuel (Guildford),* Volume 116, pp. 672-691.

Notz, R., Mangalapally, H. P. & Hasse, H., 2012. Post combustion CO2 capture by reactive absorption: Pilot plant description and results of systematic studies with MEA. *International Journal of Greenhouse Gas Control,* Volume 6, pp. 84-112.

Oexmann, J., Kather, A., Linnenberg, S. & Liebenthal, U., 2012. Post-combustion CO2 capture: chemical absorption processes in coal-fired steam power plants. *Greenhouse Gases: Science and Technology,* 2(2), pp. 80-98.

Oko, E., Wang, M. & Joel, A. S., 2017. Current status and future development of solvent-based carbon capture. *International Journal of Coal Science & Technology,* 4(1), pp. 5-14.

Olah, G. A., Goeppert, A. & Prakash, G. K. S., 2018. *Beyond Oil and Gas: The Methanol Economy.* 3rd ed. Weinheim, Germany: Wiley-VCH.

Olumayegun, O. & Wang, M., 2019. Dynamic modelling and control of supercritical CO2 power cycle using waste heat from industrial processes. *Fuel (Guildford),* Volume 249, pp. 89-102.

Ott, J. et al., 2012. Methanol. In: *Ullmann's Encyclopedia of Industrial Chemistry.* Weinheim, Germany: Wiley-VCH.

Pérez-Fortes, M., Schöneberger, J. C., Boulamanti, A. & Tzimas, E., 2016. Methanol synthesis using captured CO2 as raw material: Techno-economic and environmental assessment. *Applied Energy,* Volume 161, pp. 718-732.

Pontzen, F. et al., 2011. CO2-based methanol and DME - Efficient technologies for industrial scale production. *Catalysis Today,* 171(1), pp. 242-250.

Rajeshwar, K., Licht, S. & McConnell, R., 2008. *Solar Hydrogen Generation: Toward a Renewable Energy Future.* 1 ed. New York, USA: Springer.

Sollai, S. et al., 2023. Renewable methanol production from green hydrogen and captured CO2: A techno-economic assessment. *Journal of CO2 Utilization,* Volume 68, p. 102345.

Sood, S. et al., 2020. Generic dynamical model of PEM electrolyser under intermittent sources. *Energies (Basel),* 13(24), p. 6556.

Spong, M. W., 2023. *Introduction to Modeling and Simulation: A Systems Approach.* New Jersey, USA: Wiley.

Striednig, M., Brandstätter, S., Sartory, M. & Klell, M., 2014. Thermodynamic real gas analysis of a tank filling process. *International Journal of Hydrogen Energy,* 39(16), pp. 8495-8509.

Tahan, M.-R., 2022. Recent advances in hydrogen compressors for use in large-scale renewable energy integration. *International Journal of Hydrogen Energy,* 47(83), pp. 35275-35292.

Tait, P. et al., 2016. A pilot-scale study of dynamic response scenarios for the flexible operation of post-combustion CO2 capture. *International Journal of Greenhouse Gas Control,* Volume 48, pp. 216-233.

Ulleberg, Ø., 2003. Modeling of advanced alkaline electrolyzers: A system simulation approach. *International Journal of Hydrogen Energy,* 28(1), pp. 21-33.

Ursua, A., Gandia, L. M. & Sanchis, P., 2012. Hydrogen Production From Water Electrolysis: Current Status and Future Trends. *Proceedings of the IEEE,* 100(2), pp. 410-426.

Vaz, S., Rodrigues de Souza, A. P. & Lobo Baeta, B. E., 2022. Technologies for carbon dioxide capture: A review applied to energy sectors. *Cleaner Engineering and Technology,* Volume 8, p. 100456.

Verhelst, S., Turner, J. W., Sileghem, L. & Vancoillie, J., 2019. Methanol as a fuel for internal combustion engines. *Progress in Energy and Combustion Science,* Volume 70, pp. 43-88.

Wang, M., Wang, Z., Gong, X. & Guo, Z., 2014. The intensification technologies to water electrolysis for hydrogen production – A review. *Renewable & Sustainable Energy Reviews,* Volume 29, pp. 573-588.

Wang, Y., Zhao, L., Otto, A. R. M. & Stolten, D., 2017. A Review of Post-combustion CO2 Capture Technologies from Coal-fired Power Plants. *Energy Procedia,* Volume 114, pp. 650-665.

Wilberforce, T. et al., 2021. Progress in carbon capture technologies. *The Science of the Total Environment,* Volume 761, p. 143203.

Yang, B. & Abramova, I., 2022. *Dynamic Systems: Modeling, Simulation, and Analysis.* Cambridge, UK: Cambridge University Press.

Yodwong, B. et al., 2020. Faraday's efficiency modeling of a proton exchange membrane electrolyzer based on experimental data. *Energies (Basel),* 13(18), p. 4792.

Yu, C. H., Huang, C. H. & Tan, C. S., 2012. A Review of CO2 Capture by Absorption and Adsorption.. *Aerosol and Air Quality Research,* 12(5), pp. 745-769.

Zhen, X. & Wang, Y., 2015. An overview of methanol as an internal combustion engine fuel. *Renewable & Sustainable Energy Reviews,* Volume 52, pp. 477-493.

Zheng, J. et al., 2012. Development of high pressure gaseous hydrogen storage technologies. *International Journal of Hydrogen Energy,* 37(1), pp. 1048-1057.

Øi, L. E. et al., 2016. Simulation and Cost Comparison of CO2 Liquefaction. *Energy Procedia,* Volume 86, pp. 500-510.

APPENDIX A: PEM ELECTROLYSIS MODELLING PARAMETERS

Parameter	Value	Unit	Source	Reference condition
N	700	-		
A_{cell}	0.3	m^2		
m_{PEM}	1 000	kg		
c_{PEM}	1 000	J/kgK		
p_{cell}	50	bar		
T_{cell}	30	°C		
p_{ref}	1	bar	(Järvinen, et al., 2022)	-
r	0.2	Ωcm^2		
α	0.6	-		
j_0	$3*10^{-7}$	A/cm^2		
j_L	3.5	A/cm^2		
b_1	0.1	-	(Antoniou, et al., 2022)	-
b_2	-0.3	-	(Antoniou, et al., 2022) Fixed from a value of 0.3 used in the source	-
R	8.314463	J/molK	(NIST Physical Measurement Laboratory, 2024)	-
F	96 485.33	C/mol	(NIST Physical Measurement Laboratory, 2024)	-
z	2	-	(Buttler & Spliethoff, 2018)	-
U_{tn}	1.482	V	(Ulleberg, 2003)	(20 °C, 1 atm)
c_{H_2O}	4 169	J/kgK	(NIST Chemistry WebBook, 2023)	(20 °C, 50 bar)
M_{H_2O}	18.0153	g/mol	(NIST Chemistry WebBook, 2023)	-

APPENDIX B: COMPRESSED HYDROGEN STORAGE SYSTEM MODELLING PARAMETERS

Parameter	Value	Unit	Source	Reference condition
R	8.314463	J/molK	(NIST Physical Measurement Laboratory, 2024)	-
M_{H_2}	2.01588	g/mol	(NIST Chemistry WebBook, 2023)	-
n	1.1	-		
η_{comp}	0.95	-		
V_{sto}	26	m^3		
C_v	0.03	m^2mol/kg		

APPENDIX C: HYDROGEN COMPRESSIBILITY FACTOR COEFFICIENT DEFINITIONS

Term definition	Value	Unit	Source
R	8.314463	J/molK	(NIST Physical Measurement Laboratory, 2024)
M_{H_2}	2.01588	g/mol	(NIST Chemistry WebBook, 2023)
R_{H_2}	$\frac{R}{M_{H_2}}$	J/kgK	(Striednig, et al., 2014)
a_1	-3.694172494172333e-08	m^3/kgK^2	(Striednig, et al., 2014)
a_2	-3.506993006991895e-11	$(m^3/kgK)^2$	(Striednig, et al., 2014)
b_1	3.189634592074488e-05	m^3/kgK	(Striednig, et al., 2014)
b_2	-1.696430419581131e-08	$(m^3/kg)^2/K$	(Striednig, et al., 2014)
c_1	9.834748827973704e-04	m^3/kg	(Striednig, et al., 2014)
c_2	7.6696112812326303e-05	$(m^3/kg)^2$	(Striednig, et al., 2014)
K_1	$\frac{a_1}{R_{H_2}}$	1/PaK	(Striednig, et al., 2014)
K_2	$\frac{b_1}{R_{H_2}}$	1/Pa	(Striednig, et al., 2014)
K_3	$\frac{c_1}{R_{H_2}}$	K/Pa	(Striednig, et al., 2014)
K_4	$\frac{{a_1}^2}{{R_{H_2}}^2}$	$1/Pa^2K^2$	(Striednig, et al., 2014)
K_5	$\frac{2a_1b_1}{{R_{H_2}}^2}$	$1/Pa^2K$	(Striednig, et al., 2014)
K_6	$\frac{2a_1c_1 + {b_1}^2 - a_2}{{R_{H_2}}^2}$	$1/Pa^2$	(Striednig, et al., 2014)
K_7	$\frac{b_2 - 2b_1c_1}{{R_{H_2}}^2}$	K/Pa^2	(Striednig, et al., 2014)
K_8	$\frac{c_2 - {c_1}^2}{{R_{H_2}}^2}$	K^2/Pa^2	(Striednig, et al., 2014)

APPENDIX D: CO_2 ABSORPTION PROCESS MODELLING PARAMETERS

Parameter	Value	Unit	Source	Reference condition
$\dot{m}_{unloaded_{max}}$	5	kg/s		
$wt-\%_{MEA}$	30	%		
M_{CO_2}	44.0095	g/mol	(NIST Chemistry WebBook, 2023)	-
M_{MEA}	61.0831	g/mol	(NIST Chemistry WebBook, 2023)	-
$c_{m_{MEA}}$	182	J/molK	(Cheméo, n.d.)	(80 °C)
c_{CO_2}	903.76	J/kgK	(NIST Chemistry WebBook, 2023)	(80 °C, 1.5 bar)
c_{H_2O}	4 196.6	J/kgK	(NIST Chemistry WebBook, 2023)	(80 °C, 1.5 bar)
c_{N_2}	1 042.9	J/kgK	(NIST Chemistry WebBook, 2023)	(80 °C, 1.5 bar)
c_{O_2}	930.28	J/kgK	(NIST Chemistry WebBook, 2023)	(80 °C, 1.5 bar)
w_{CO_2}	0.165	kg/kg_{fg}	(Notz, et al., 2012)	-
w_{H_2O}	0.069	kg/kg_{fg}	(Notz, et al., 2012)	-
w_{N_2}	0.672	kg/kg_{fg}	(Notz, et al., 2012)	-
w_{O_2}	0.094	kg/kg_{fg}	(Notz, et al., 2012)	-
X_{max}	2.3	$mol_{CO2}/kg_{solvent}$		
$m_{unloaded_{sump}}$	3 500	kg		
$\Delta H_{absorption}$	85 000	J/mol_{CO2}	(Kim & Svendsen, 2007)	(40 °C)

APPENDIX E: CO_2 STRIPPING PROCESS MODELLING PARAMETERS

Parameter	Value	Unit	Source	Reference condition
$\dot{m}_{unloaded_{max}}$	5	kg/s		
$wt-\%_{MEA}$	30	%		
M_{CO_2}	44.0095	g/mol	(NIST Chemistry WebBook, 2023)	-
M_{MEA}	61.0831	g/mol	(NIST Chemistry WebBook, 2023)	-
$c_{m_{MEA}}$	182	J/molK	(Cheméo, n.d.)	(80 °C)
c_{CO_2}	903.76	J/kgK	(NIST Chemistry WebBook, 2023)	(80 °C, 1.5 bar)
c_{H_2O}	4 196.6	J/kgK	(NIST Chemistry WebBook, 2023)	(80 °C, 1.5 bar)
$m_{unloaded_{sump}}$	3 500	kg		

APPENDIX F: LIQUID CO_2 STORAGE SYSTEM MODELLING PARAMETERS

Parameter	Value	Unit	Source	Reference condition
R	8.314463	J/molK	(NIST Physical Measurement Laboratory, 2024)	-
M_{CO_2}	44.0095	g/mol	(NIST Chemistry WebBook, 2023)	-
n	1.1	-		
η_{comp}	0.95	-		
$V_{feedline_{comp}}$	0.5	m^3		
$V_{feedline_{valve}}$	2.5	m^3		
C_v	0.002	m^2mol/kg		

APPENDIX G: GREEN METHANOL SYNTHESIS MODELLING PARAMETERS

Parameter	Value	Unit	Source	Reference condition
m_{gas}	14.9	kg		
M_{CO_2}	44.0095	g/mol	(NIST Chemistry WebBook, 2023)	-
M_{H_2}	2.01588	g/mol	(NIST Chemistry WebBook, 2023)	-
$c_{m_{CO_2}}$	47.737	J/molK	(NIST Chemistry WebBook, 2023)	(230 °C, 50 bar)
$c_{m_{H_2}}$	29.332	J/molK	(NIST Chemistry WebBook, 2023)	(230 °C, 50 bar)
$c_{m_{H_2O}}$	84.082	J/molK	(NIST Chemistry WebBook, 2023)	(230 °C, 50 bar)
$c_{m_{MeOH}}$	161.78	J/molK	(NIST Chemistry WebBook, 2023)	(230 °C, 50 bar)
$\Delta H_{hydrogenation}$	49 160	J/mol_{MeOH}	(Ott, et al., 2012)	(300 K)